ALBERT-LUDWIGS-
UNIVERSITÄT FREIBURG
Fakultät für Mathematik und Physik

Heating of the Corona in a 3D MHD Forward Model Approach

Dissertation zur Erlangung des Doktorgrades der
Fakultät für Mathematik und Physik der
Albert-Ludwigs-Universität
Freiburg im Breisgau

eingereicht von

Sven Bingert

aus Kusel

August 18, 2009

Betreuer

PD Dr. Hardi Peter

Dekan:	Prof. Dr. Kay Königsmann
Referent:	Dr. Hardi Peter
Koreferent:	Prof. Dr. Frank Stienkemeier
Datum der mündlichen Prüfung:	29. September 2009

Contents

Zusammenfassung

Beobachtungen der solaren Korona zeigen ein Plasma bei Temperaturen von mehreren Millionen Grad, angeordnet in bogenartigen Strukturen. Aktuelle Forschungsergebnisse weisen darauf hin, dass diese hohen Temperaturen, die weit über der Oberflächentemperatur der Sonne liegen, durch die Dissipation von Magnetfeldern erreicht werden. Der Prozess der Umwandlung von magnetischer zu thermischer Energie ist jedoch noch nicht im Detail verstanden. Dazu untersuchen wir in einem dreidimensionalen magneto-hydrodynamischen Modell den Prozess der koronalen Heizung. Dieses numerische Modell ist zeitabhängig und beschreibt die Entwicklung von Magnetfeldern über einer Aktiven Region. Es umfasst die Atmosphäre der Sonne von der Photosphäre bis zur Korona. Die Magnetfelder in der Korona werden an ihren Fußpunkten in der Photosphäre verdrillt. Dadurch entstehen Ströme, die anschließend dissipiert werden und damit die Korona aufheizen. Dies entspricht dem sogenannten DC-Prozess (Direct Current), wie er 1972 von Parker vorgeschlagen wurde. Das Modell ist in einem quasi-stationären Gleichgewicht, in dem die zugeführte Energie aus den Bewegungen in der Photosphäre durch die Strahlungsverluste in der optisch dünnen Korona kompensiert wird.

Das Modell zeigt, dass der Heizungsprozess durch die Dissipation von Strömen eine Möglichkeit ist, um eine Korona mit einer Temperatur von mehreren Millionen Grad zu erzeugen. Untersuchungen der Heizraten in unserem Modell zeigen weitere interessante Details. Die Heizung findet auf kleinen Skalen mit zeitlich zufällig verteilten Ereignissen statt. Diese Ereignisse entsprechen Nanoflares auf der Sonne. Eine Betrachtung der Größenverteilung dieser Nanoflares zeigt, dass deren Verteilung mit Beobachtungen und Theorie vereinbar ist. Unser Modell erzeugte damit erstmals selbstkonsistent eine solche Nanoflare-Verteilung.

Bei der Untersuchung der Plasmaeigenschaften entlang von Magnetfeldbögen zeigten sich Ähnlichkeiten zu bereits bekannten Skalengesetzen. Dabei ist jedoch eine große Streuung zu erkennen, was die Anwendbarkeit der Skalengesetze für beliebige Magnetfeldkonfigurationen in Frage stellt. Insbesondere bei der Anwendung auf stellare Koronen sollte eine veränderte magnetische Aktivität berücksichtigt werden.

Die synthetisierten Emissionslinien unserer Modellkorona zeigen eine gute Übereinstimmung mit Beobachtungen. Eine Analyse des Differentiellen Emissionsmaßes ergab eine Temperaturabhängigkeit, wie sie auch aus Beobachtungen abgeleitet wurde.

Daher kann davon ausgegangen werden, dass die physikalischen Parameter der Modellkorona, wie z.B. Temperatur und Dichte, die Werte der realen solaren Korona realistisch abbilden.

Bogenartige Strukturen, die bei der Betrachtung des Modells in der Emissionslinie Ne VIII zu sehen sind, scheinen nicht mit den Magnetfeldlinien zu korrelieren. Diese sogenannten iLoops (intensity Loops) weisen darauf hin, dass die Korona nicht nur aus Strukturen entlang von Magnetfeldern aufgebaut ist und damit das Konzept der Skalengesetze nur bedingt anwendbar ist.

Die vorgelegte Arbeit zeigt die Stärke der dreidimensionalen nummerischen Modelle, die Ergebnisse liefern welche direkt mit Beobachtungen verglichen werden können (Forward model approach). Durch die Verwendung verschiedener photosphärischer Randbedingungen können unterschiedliche Phänomene der solaren Korona untersucht werden. Unser Modell beschreibt Ergebnisse aus Beobachtungen ohne Annahmen zu machen die auf Beobachtungen basieren. Resultate des Modells beruhen nicht auf den Anfangsbedingung sondern ergeben sich aus den Grundannahmen der MHD und den physikalischen Randbedingungen.

Abstract

Observations of the solar corona show loop-like structures formed by plasma at temperatures of one million degrees and higher. Since the solar surface is much cooler than the corona, a heating mechanism must be responsible for the high temperatures. The dissipation of magnetic fields in the corona could provide such a heating mechanism. However, the process of transforming magnetic energy into thermal energy is still not yet understood in detail. To investigate this process and its impact on the heating of the corona, we employ a three-dimensional magneto-hydrodynamical model. This numerical model synthesizes the temporal evolution of the magnetic field above an Active Region. It includes the solar atmosphere from the photosphere up to the corona. The magnetic field in the corona is braided by foot point motions in the photosphere. This is done similarly to the braiding through granulation in reality. The stressed magnetic field induces currents which are then dissipated in the corona. This idea is known as the *DC model* (direct current) and was proposed by Parker in 1972. The model reaches a quasi-stationary state, i.e. the energy input by photospheric motions is counterbalanced by radiative losses in the optically thin corona. As a result, the described heating process creates and sustains a hot corona with a temperature of one million degrees and higher.

Persistent heating is created by single heating events randomly distributed in time - comparable to Nanoflares observed on the Sun. A statistical analysis of the heating events in our model results in a Nanoflare distribution as claimed by theory and observations. The is the first time that a complex numerical model self-consistently produces a Nanoflare distribution strong enough to maintain the high coronal temperatures.

We also investigated plasma properties along magnetic field lines. The results are comparable to known scaling laws, but they show a large spread. This is an indication that the scaling laws are sensitive to the magnetic field configuration at the solar surface. This means that in order to explain a corona or atmospheres above active stars, the scaling laws have to be treated with care.

We pursue the forward model approach and synthesize line emissions at different wavelengths. The differential emission measure can be used as a tool to compare our model with observations. An analysis shows that the temperature dependency of the differential emission measure in the model fits well to the values obtained by

the interpretation of observational data. Therefore, one can justifiably assume that the average plasma properties in our model corona, such as temperature and density, are comparable to the plasma properties on the Sun.

When we look at the loop-like structures in the emission line of Ne VIII in our model, they are seemingly not correlated with magnetic field lines. These iLoops (intensity Loops) reveal that the corona is not entirely built of structures following magnetic field lines. Thus it might be possible that the emission from more active coronae is not mainly produced by loops following magnetic fieldlines.

The model presented in this thesis shows a great advantage of the forward model approach using complex three-dimensional numerical models: The results are directly comparable to observable quantities. The model corona in this 'ab initio' approach depends only on the MHD assumptions and the physical boundary conditions but not on the initial condition. The application of different boundary conditions allows us to investigate various phenomena in the solar corona. Hence, the model provides a crucial tool to critically evaluate the interpretation of observational data.

1 Introduction

Already thousands of years ago, people were amazed by the shiny phenomenon around the Sun during a solar eclipse. This faint object was called corona, which is Latin for 'crown'. It puzzled the people and is up to the present day an interesting field of research. Figure 1.1 illustrates an impressive image of the solar corona. Since the corona was only seen during solar eclipses it was assumed to belong to the moon. Either it was the moon's atmosphere, light scattering on the moon's surface or solar light refracted in the moon's atmosphere. The first proof, that the corona is part of the solar atmosphere was obtained by two independent observations. During the eclipse on 18th July 1860, A. Secchi and W. De La Rue made photographs, 500 km apart, that did not show any parallax of the prominences seen in the pictures. This would have been the case for features on the nearby moon.

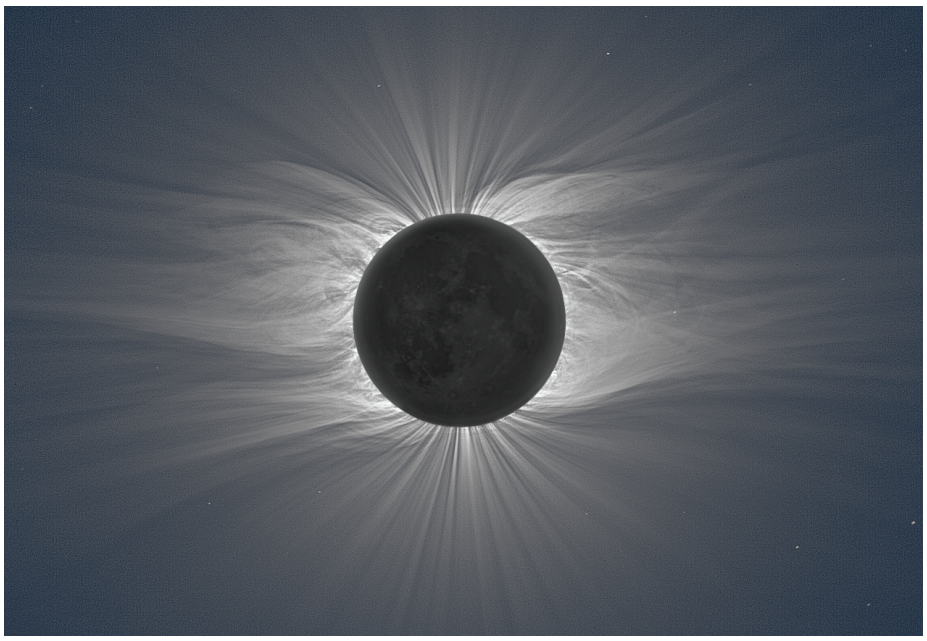

Figure 1.1: Solar eclipse 2009 observed at Enewetak Atoll, Marshal Islands. Composition of 38 eclipse images. Image processing by Miloslav Druckmüller. Courtesy: Miloslav Druckmüller, Peter Aniol, Vojtech Rusin, Lubomir Klocok, Karel Martisek, Martin Dietzel. *www.zam.fme.vutbr.cz/∼druck/Eclipse/index.htm*

With the invention of the coronograph by B. Lyot (1930), it was possible to observe the corona not only during eclipses. The coronograph is a pinhole camera behind an occulting disk rejecting direct solar light. Employing such instruments, the corona, with a brightness less than a million of the brightness of the Sun, becomes observable.

The spectrum of the Sun is in first order a Planck spectrum of a black body with six thousand Kelvin. The intensity coming from the solar disc decreases rapidly towards the high energy range in the extreme ultraviolet (EUV). In this wavelength range the emission of the corona is therefore brighter than light coming from solar surface. Since the earth's atmosphere is opaque in this wavelength range high energy observations of the corona in the EUV are only possible in space. Nowadays an armada of ground based telescopes as well as space missions observe the Sun and its atmosphere in different wavelengths and with various methods, like imaging or spectroscopic measurements.

In the last decades many discoveries were made and problems solved. For instance, the element coronium was postulated to explain the green emission line which later was identified as the emission of highly ionized iron. But one of the major riddles in solar physics withstands to be solved up to the present day: The temperature of the corona exceeds the temperature of the solar surface by a factor of 200 and above. This is known since almost eighty years now and the mechanism to heat the corona is still not understood in detail. Actually, Grotrian (1931) did not mention the high temperature, but he was the first one who derived the electron velocity in the corona based on the Doppler broadening of a certain line. Using measurements from the solar eclipse on May 9th 1929, the resulting electron velocity is ten times higher than the thermal speed at temperatures found on the solar surface. Since the surface temperature was the highest conceivable temperature at that time, he argued that other scenarios or phenomena have to be utilized to explain the high velocity. Later, Edlén (1943) identified coronal emission lines as transitions of highly ionized atoms. Since then it was clear that the solar corona has to be hotter than a million degrees.

1.1 The Sun

Even though the heating mechanism is not yet understood completely, it seems natural that the energy for the heating process originates from the solar interior. The Sun generates energy in the core by fusion of hydrogen into helium at around 15 billion Kelvin. The energy is then transported outwards by radiation in the inner two thirds of the solar radius and by convection in the outer layer. The convection zone is superadiabatic and therefore forms an unstable layer. The temperature drops from one million degrees at the bottom of the convection zone to roughly 6000 Kelvin in the photosphere, the layer above the convection zone. A schematic view of the solar interior is illustrated in figure 1.2. The photosphere is defined as the layer when

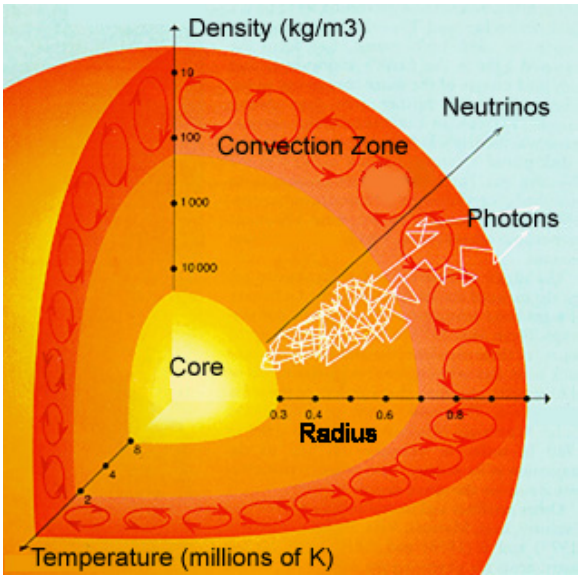

Figure 1.2: A cut-away schematic of the Sun from the Center for Science Education of the Berkeley University of California.

the surface becomes transparent to the radiation from below. It is visible as yellow disk from the earth, where almost all radiation originates from. A closer look reveals a regular pattern for the convection, the so-called granules. Over a small fraction of the Sun the granulation is replaced by dark structures. These structures, for example Sun spots or Active Regions, are visible manifestations of magnetic fields. Figure 1.3 illustrates an Active Region surrounded by granulation. It is believed that the solar dynamo process generates magnetic fields at the bottom of the convection zone. Sun spots are therefore perpendicular cuts through magnetic flux tubes which are based deep in the convection zone and extend high into the solar atmosphere.

In the photosphere the plasma becomes optically thin. Whereas information from the solar interior can only be obtained from helioseismology, the atmosphere above can be observed directly. The solar atmosphere is divided into three layers. The chromosphere above the photosphere is a relatively cool layer, well observed but not yet totally understood. The plasma is not fully ionized and mostly not in local thermal equilibrium. As well as the corona the chromosphere are cooled by radiative losses. The Heating mechanism proposed are magnetic by nature or dissipation of acoustic shock waves. The interface between the cool and dense chromosphere to the hot corona is called transition region. In this relatively thin layer - less than 1% of the solar radius - the temperature rises up to one million degrees. From the transition region the corona reaches up to three solar radii into the space.

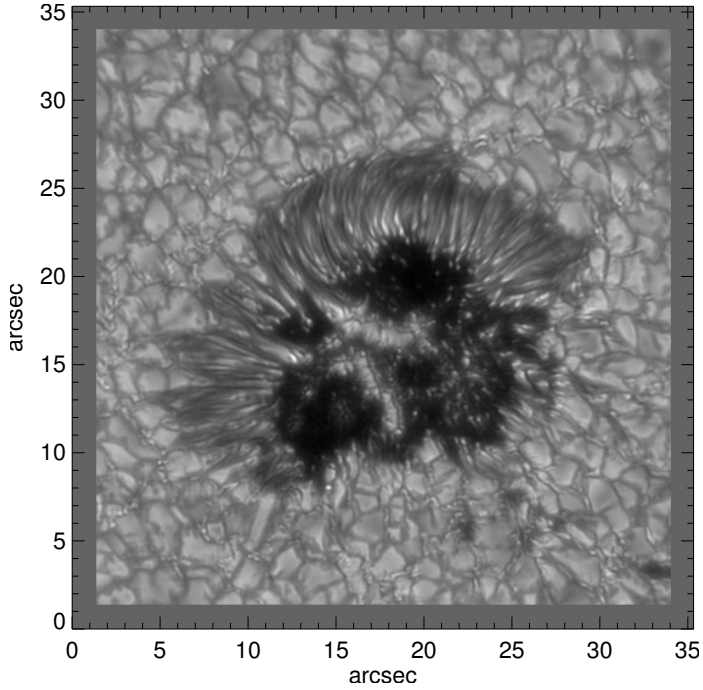

Figure 1.3: Active Region AR11024 and granulation. Recorded on July 4th 2009 in the G band at 403 nm (Vakuum Turm Teleskop (VTT), Kiepenheuer-Institut für Sonnenphysik).

1.2 Solar Corona

The corona is mostly observed with space missions in the extreme ultraviolet wavelength range. Successful missions, such as the Solar & Heliospheric Observatory (SOHO, Domingo et al. (1995)) and the Transition Region And Coronal Explorer (TRACE, Handy et al. (1999)), provide data over long time periods. Observations reveal that the structure of the corona strongly depends on the solar cycle of 22 years. During that time, the polarity of the magnetic field in the east-west oriented Active Regions changes twice (Hale's polarity law). Therefore, the Sun has an activity cycle of 11 years. During the solar maximum the corona is highly structured and visible almost all over the entire Sun. During solar minimum, the corona appears only above the solar equator and looks more diffuse. Hence, this gives a first indication, that coronal structures and the coronal heating mechanism are related to the magnetic fields.

1.2.1 Coronal magnetic fields

The solar magnetic field determines the dynamics and topology of the corona. Hot plasma with a high degree of ionization can only flow along magnetic fieldlines. There-

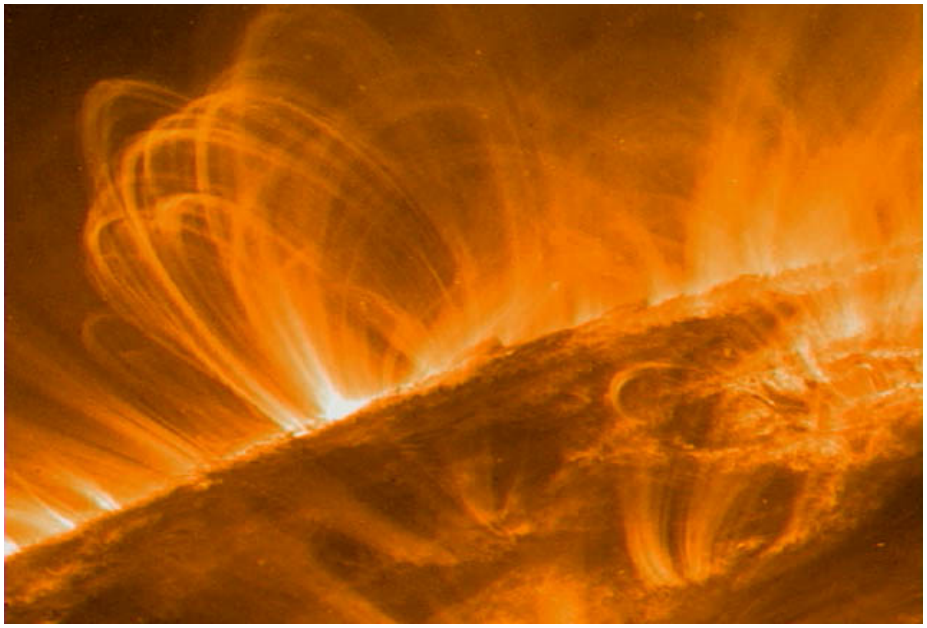

Figure 1.4: TRACE image of coronal loops, taken in the 17.1 nm passband. This is characteristic for plasma at one million degrees Kelvin.

fore, the heat conduction is efficient along the fieldlines and strongly suppressed perpendicular to the loop. Thus, coronal loops outline magnetic flux tubes as illustrated in figure 1.4. The knowledge of magnetic fields in the solar corona is mostly based on extrapolations of measurements on the solar surface. In order to obtain this, the Zeemann splitting of spectral lines is used to derive the magnetic field configuration in the photosphere. However, extrapolations into the corona are uncertain due to unknown currents and non-potential field conditions. The fact that coronal loops expand less with height as extrapolated magnetic fields emphasizes the inadequacy of such models. Direct magnetic field measurements in the corona would be adjuvent but are only available in low temporal and spatial resolution. These measurements employ effects of Faraday rotation, the polarization of free-free emission, Hanle effect in Lyman-α, or Stokes polarimetry in infrared lines. But only integrated magnetic field properties along the line of sight of the optically thin corona can be derived. When looking at the disk center, information over a wide range in height is mixed up. Therefore, one has to measure above the limb at least over a period of half a solar rotation to use the so called tomographic reconstruction method.

1.2.2 Coronal heating

The second law of thermodynamics tells us that the temperature should drop when we go from the photosphere towards the outer layers of the solar atmosphere. But the temperature increases, which calls for a heating mechanism to resolve this con-

tradiction. This heating mechanism must be able to produce and maintain the high temperatures from the outer chromosphere up to the corona. Different models were proposed in the last decades, and some have already been disproved. One model is the purely hydrodynamical model in which upward traveling waves turn into shocks and dissipate their energy. This scenario cannot provide the required amount energy to heat the corona. The acoustic waves do not reach the upper atmosphere but are mostly dissipated in the chromosphere and contribute to the heating of the latter. Another model is based upon the energy transport by the electromagnetic field. This scenario is classified into DC models (Direct Current) and AC models (Alternating Current). These two types differ in the relation between the timescale of the mechanical driver in the photosphere and the Alfvén transit time along a loop. A magnetic disturbance propagates with the Alfvén speed v_A along a magnetic fieldline. For DC models the mechanical driving is slow and the loop behaves quasi-static. When the photospheric driver changes faster than the Alfvén transit time, the loop 'sees' an alternating current (AC model).

AC models

In AC models the energy of waves traveling along a loop is dissipated within a short distance in the corona. Typically, there are three different types of waves: the purely magnetic and the fast and slow magneto-acoustic waves. The magnetic waves (Alfvén waves) travel along the field whereas the magneto-acoustic modes propagate transverse. The magnetic-acoustic waves are mostly reflected due to the strong gradients in density and pressure and thus do not reach the corona. Therefore only the Alfvén waves can significantly contribute to the coronal heating. These waves can travel unimpeded into the corona. In order to utilize these waves for the heating mechanism, an enhanced dissipation of these waves has to take place in the corona. There are two types of AC heating: the phase mixing and the resonant absorption. Phase mixing occurs when the Alfvén speeds of two nearby fieldlines differ so that the waves are out of phase in the corona. As a consequence gradients in the gas speed increase, leading to instabilities and the dissipation of the wave. Resonant absorption happens when the driver frequency is equal to the eigen-frequency of the loops. Again, large gradients in the plasma speed cause absorption of the waves and viscous dissipation of the energy.

DC models

Here we distinguish between stress-induced reconnection, currents and turbulence. In the reconnection model flux tubes are braided and non-potential energy is stored up to a certain threshold. The energy is then released by sporadic dissipation events, the so called Nanoflares. The other scenario suggests that foot point motions in the photosphere stir up a potential to a non-potential coronal magnetic field. Thus,

currents occur in the non-potential field which can than be dissipated and heat the corona. This process is called Ohmic dissipation or Joule heating. The stress-induced turbulence model describes a cascade of energy towards smaller length scales where the dissipation process is more efficient. The dissipation itself is again Ohmic.

1.3 Forward model approach

Forward modeling builds the connection between theory and observations. Starting from a physical model it allows to examine observable consequences. Input parameters can be adjusted to reproduce observations. Hence theoretical models can be tested or even eliminated. Its predictive character, by telling what may be observable, helps to design future experiments and instrumental designs.

Yet, the forward model approach is used by several authors for testing different models of Nanoflare heating in the solar corona. A review about the forward model approach and its application is given in de Moortel et al. (2008). Results of theses models could already reproduce parts of observations. Most of the models do not self-consistently compute the heating mechanism but make for example assumptions about the background plasma. However, most of these models were restricted to 0D or 1D hydrodynamics of coronal loops. A step further are the large scale 3D magneto-hydrodynamic simulations such as those by Gudiksen and Nordlund (2005). They simulated a model of the solar corona *ab initio*. The basic idea was that braiding of magnetic fieldlines by photospheric motions could heat the corona. Using these results, Peter et al. (2004, 2006) calculated both line intensities and Doppler shifts and found a remarkable accordance to observed emission measures and Doppler shifts. Nevertheless, it was not possible to conduct parameter studies or to simulate different solar phenomena. The high demands on computing resources for these 3D MHD models is still an ongoing issue.

1.4 Motivation and scope of this work

We want to investigate the importance of Ohmic heating as a heating mechanism for the solar corona. Therefore, we conduct a three dimensional magneto-hydrodynamic numerical model. Thereby we emphasize the details in the energy balance equation. In this dynamic model the foot points of magnetic fieldlines are shuffled around by the almost random motions in the photosphere. Thereby the fieldlines are braided in the atmosphere. This conforms to the heating process suggest by Parker (1972). His illustration of the fieldline braiding is shown in figure 1.5. The resulting complex pattern of the magnetic field induces currents that dissipate as Joule heating. It took thirty years before this process could be investigated in three dimensional numerical models with complex magnetic configurations.

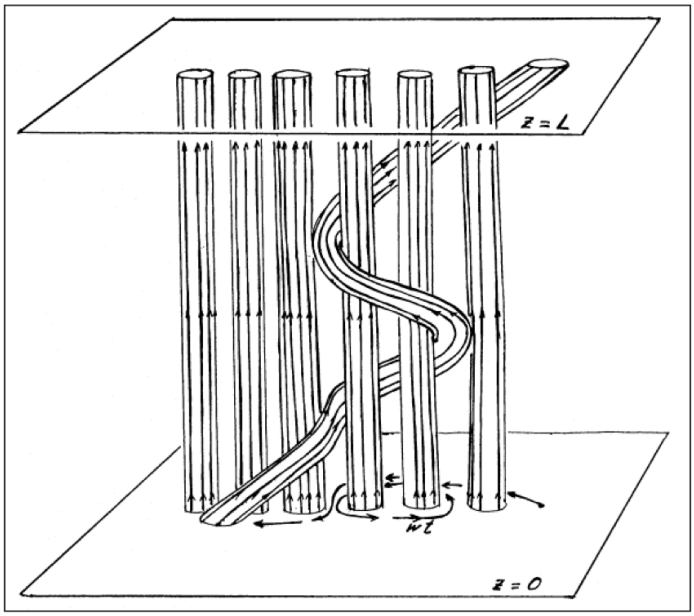

Figure 1.5: Schematic drawing of the topology of magnetic flux tubes of force following a displacement of the ends of the tubes (Parker, 1983).

We carry on the idea of the ab initio coronal model by Gudiksen and Nordlund (2005). They used a reduced Spitzer heat conduction to increase the time step. They argue that it is sufficient as long as the Spitzer heat conduction is the fastest process in the simulation. We use the Spitzer heat conduction term as derived by Spitzer and Härm (1953) and obtain smaller time steps. Therefore, structures in the temperature distribution should be better resolved. Another limitation of the model (Gudiksen and Nordlund, 2005) is the short time period of solar data. We want to produce longer time series to be able to investigate statistical properties of the solar corona. The data obtained from the model is used after an initial phase which is more than twice as long as the initial phase in Gudiksen and Nordlund (2005). This improves the assumption that the initial condition is forgotten and the model only depends on the boundary conditions.

We use different magnetic boundary conditions to work out the dependency of the observable coronal structures on the underlying magnetic activity. How do line emissions in different wavelength change when the underlying magnetic field increases in complexity.

2 Basic equations of MHD

Even tough there are several good textbooks around, in which one can find the basic equations of magneto-hydrodynamics, we would like to summarize the important equations used in this thesis. Thus, this chapter can be used as formulary since the notations are the same throughout the entire work. A summary of the equations used in the way they are implemented in the numerical code can be found in chapter 4.2.

2.1 Maxwell's equations

We start with Maxwell's equations (Maxwell, 1865) in differential form:

$$\nabla \cdot \mathbf{E} = \frac{\rho^*}{\epsilon} \tag{2.1}$$

$$\nabla \cdot \mathbf{B} = 0 \tag{2.2}$$

$$\nabla \times \mathbf{E} = -\frac{\partial \mathbf{B}}{\partial t} \tag{2.3}$$

$$\nabla \times \mathbf{B} = \mu\, \mathbf{j} + \epsilon\mu \frac{\partial \mathbf{E}}{\partial t} \tag{2.4}$$

where ρ^* is the charge density. The permittivity ϵ and the magnetic permeability μ may be replaced with their respective vacuum values in the solar atmosphere. They are related to the speed of light c_0 by

$$\epsilon_0 \mu_0 c_0^2 = 1$$

Introducing a typical length scale L and a typical time scale T for the plasma motions, resulting in a typical velocity of $V = L/T$, one can approximate Maxwell equations. Replacing $\nabla \times \mathbf{E}$ with $\frac{E}{L}$ and approximating $\frac{\partial \mathbf{B}}{\partial t} \approx \frac{B}{T}$ in equation 2.3 leads to

$$\frac{E}{L} \approx \frac{B}{T} \tag{2.5}$$

Now we can express the displacement current on the right hand side of equation 2.4 ($\frac{\partial \mathbf{E}}{\partial t} \approx \frac{E}{T}$) as

$$\epsilon_0 \mu_0 \frac{E}{T} = \frac{V^2}{c^2} \frac{B}{L}$$

by using the typical scales and equation 2.5. Since the characteristic plasma velocities are much smaller than the speed of light, $V \ll c$, the displacement current can be neglected when compared to the left hand side of equation 2.4:

$$\frac{B}{L} \gg \frac{V^2}{c^2}\frac{B}{L} \tag{2.6}$$

Furthermore, we arrogate charge neutrality, that is $n_e - n_i \ll n$, with n_e and n_i being the number densities for electrons and ions respectively, while n represents the total number density. The charge imbalance is given by equation 2.1 and can be expressed as

$$(n_+ - n_-)\, e = \rho^* \approx \epsilon\frac{E}{L} = \epsilon\frac{VB}{L},$$

where we used again equation 2.5.
In chapter 3.4 we will show that the resulting assumption

$$\frac{\epsilon}{e}\frac{VB}{L} \ll n \tag{2.7}$$

is meaningful.

Including all assumptions Maxwell's equations reduce to:

$$\nabla \cdot \mathbf{B} = 0 \tag{2.8}$$

$$\nabla \times \mathbf{E} = -\frac{\partial \mathbf{B}}{\partial t} \tag{2.9}$$

$$\nabla \times \mathbf{B} = \mu_0\, \mathbf{j} \tag{2.10}$$

Equation 2.10 is also known as Ampère's law.

2.2 Ohm's law

Ohm's law states that the current $\mathbf{j}$ is proportional to the voltage. In other words, the current density is proportional to the total electric field. Deviations from this law are well known and desired for example in semiconductors. To derive Ohm's law properly we may start with Boltzmann's equation for each particle species. The difference of the first moments of these equations would lead us to a generalized Ohm's law. But in this work we are not accounting for the micro physical processes thus we use the simplified form

$$\mathbf{j} = \sigma\,(\mathbf{E} + \mathbf{u} \times \mathbf{B}) \tag{2.11}$$

It describes the proportionality for a frame of reference moving with the plasma at a velocity $\mathbf{u}$. Additionally, the electric conductivity σ is proportional to the electron number density and the collision times between the particle species.

2.3 Induction equation

It is common to combine the simplified Maxwell's equations 2.9 and 2.10 as well as Ohm's law to replace the electric field. This leads us to the induction equation. First we take the curl of Ohm's law and replace the electric field using the third Maxwell equation. Then we replace the current using Ampere's law.

$$\begin{aligned}
\nabla \times \frac{1}{\sigma}\mathbf{j} &= \nabla \times \mathbf{E} + \nabla \times (\mathbf{u} \times \mathbf{B}) \\
&= -\frac{\partial \mathbf{B}}{\partial t} + \nabla \times (\mathbf{u} \times \mathbf{B}) \\
\nabla \times \eta (\nabla \times \mathbf{B}) &= -\frac{\partial \mathbf{B}}{\partial t} + \nabla \times (\mathbf{u} \times \mathbf{B}) \\
\frac{\partial \mathbf{B}}{\partial t} &= \nabla \times (\mathbf{u} \times \mathbf{B}) - \nabla \times \eta (\nabla \times \mathbf{B}) \qquad (2.12)
\end{aligned}$$

The factor $\eta = 1/\sigma\mu$, as well as σ, is not spatially constant on micro physical scales. We will discuss the resistivity η in more detail in chapter 6.

The induction equation describes the temporal and spatial evolution of the magnetic field including the dissipation of magnetic energy. Is $\eta = 0$, meaning the plasma is a perfect conductor, the magnetic fieldlines are forced to move alongside with the plasma. The condition is known as the "frozen in" theorem by H. Alfvén.

2.3.1 Vector potential

Since we are interested in the temporal and spatial evolution of the magnetic field, we have to solve the induction equation (cf. equation 2.12). The main goal for a non conservative code, as used in this thesis, is to assure that the divergence of the magnetic field is always zero as stated by the second Maxwell equation 2.2. Therefore we use a vector potential $\mathbf{A}$ that obeys

$$\mathbf{B} = \nabla \times \mathbf{A}$$

resulting in a divergence of $\mathbf{B}$ like

$$\nabla \cdot \mathbf{B} = \nabla \cdot (\nabla \times \mathbf{A}) = 0$$

for all times. Now the induction equation can be written as

$$\frac{\partial \mathbf{A}}{\partial t} = \mathbf{u} \times (\nabla \times \mathbf{A}) - \eta \nabla \times \nabla \times \mathbf{A}\,.$$

Because of gauge invariance, we can add the gradient of an arbitrary scalar field ϕ to the induction equation without changing the magnetic field. We choose $\phi = \eta \nabla \cdot A$. In case of constant η it simplifies to

$$\frac{\partial \mathbf{A}}{\partial t} = \mathbf{u} \times (\nabla \times \mathbf{A}) + \eta \nabla^2 \mathbf{A} \qquad (2.13)$$

2.3.2 Magnetic energy balance

As the heating in our model is assumed to be magnetic, we have to examine how the energy is transported into the corona. The energy flux in the electro-magnetic field is given by the Poynting vector. The internal energy originating from the magnetic field is given by the Ohmic heating term (cf. equation 2.37). The correlation between the two processes and the rate of change of the electro-magnetic energy is derived here.

Poynting flux

The Poynting vector describes the energy flux through a unit area per unit time and is defined as

$$\mathbf{S} = \frac{1}{\mu_0}\mathbf{E} \times \mathbf{B} \tag{2.14}$$

where $[S] = \frac{W}{m^2}$. Using Ohm's law

$$\mathbf{j} = \sigma(\mathbf{E} + \mathbf{u} \times \mathbf{B})$$

the Poynting vector can be written as

$$\begin{aligned} \mathbf{S} &= \frac{1}{\sigma\mu_0}(\mathbf{j} \times \mathbf{B}) - \frac{1}{\mu_0}(\mathbf{u} \times \mathbf{B}) \times \mathbf{B} \\ &= \frac{1}{\mu_0}\left(\eta\mu_0\mathbf{j} - \mathbf{u} \times \mathbf{B}\right) \times \mathbf{B} \end{aligned} \tag{2.15}$$

where the electric field is eliminated from the Poynting flux definition. Another way to express the Poynting flux is

$$\mathbf{S} = \frac{1}{\sigma\mu_0}(\mathbf{j} \times \mathbf{B}) + \mathbf{u}\,(\mathbf{B} \cdot \mathbf{B}) - \mathbf{B}\,(\mathbf{u} \cdot \mathbf{B}) \tag{2.16}$$

Therefore, the energy flows either perpendicular to the plane stretched by $\mathbf{j}$ and $\mathbf{B}$ or along the rectangular component of $\mathbf{u}$ to $\mathbf{B}$.

Ohmic heating and work done by the Lorentz force

In this section the change in magnetic energy due to plasma motions and dissipation are described. The magnetic energy density is given by

$$e_{\mathrm{mag}} = \frac{\mathbf{B}^2}{2\mu_0} \tag{2.17}$$

where e has a unit of $\mathrm{J/m^3}$. In order to find the rate of change we use the time derivative

$$\frac{\partial e_{\mathrm{mag}}}{\partial t} = \frac{1}{\mu_0}\mathbf{B} \cdot \frac{\partial \mathbf{B}}{\partial t}$$

Furthermore, we can use the induction equation 2.12 to replace $\frac{\partial \mathbf{B}}{\partial t}$

$$\frac{\partial e_{\mathrm{mag}}}{\partial t} = \frac{1}{\mu_0}\mathbf{B} \cdot [\nabla \times (\mathbf{u} \times \mathbf{B}) - \nabla \times \eta (\nabla \times \mathbf{B})] \tag{2.18}$$

At this point we have to exploit some vector identities and Ampere's law to reform the right hand side. The result is

$$\begin{aligned} \frac{\partial e_{\mathrm{mag}}}{\partial t} = & + \frac{1}{\mu_0}\nabla \cdot ((\mathbf{u} \times \mathbf{B}) \times \mathbf{B}) - \mathbf{u} \cdot (\mathbf{j} \times \mathbf{B}) \\ & - \nabla \cdot (\eta \mathbf{j} \times \mathbf{B}) - \eta \mu_0 \mathbf{j}^2 \end{aligned} \tag{2.19}$$

Together with the definition of the Poynting flux (cf. equation 2.15) the equation transforms to

$$\frac{\partial e_{\mathrm{mag}}}{\partial t} + \nabla \cdot \mathbf{S} = -\eta \mu_0 \mathbf{j}^2 - \mathbf{u} \cdot (\mathbf{j} \times \mathbf{B}) \tag{2.20}$$

with $\mathbf{S}$ being the Poynting vector. On the left hand side we see the conservation law of energy with the energy flux $\mathbf{S}$ and on the right hand side we have the work done by the Lorentz force and the sink of energy due to Ohmic dissipation. The latter one appears in the energy equation 2.33 in the form of Ohmic heating.

The energy loss by Lorentz force can be found if one transforms the momentum balance equation 2.27 into an energy equation by multiplying from the left with the plasma velocity $\mathbf{u}$.

2.4 Equation of continuity

The general equation of continuity has the form

$$\frac{\partial \phi}{\partial t} + \nabla \cdot \mathbf{f}_\phi = 0 \tag{2.21}$$

where $\mathbf{f}$ is the flux of the quantity ϕ. If one is interested in regions where nuclear fusion does not take place and the plasma is considered as a single fluid, mass conservation applies. Otherwise, one has to solve Boltzmann's equations to account for the particle species and their ionization state. The equation of mass conservation can be written as

$$\frac{\partial \rho}{\partial t} + \nabla \cdot (\rho \mathbf{u}) = 0 \tag{2.22}$$

or

$$\frac{D\rho}{Dt} + \rho \nabla \cdot \mathbf{u} = 0\,. \tag{2.23}$$

We introduced the material derivative following the motion also known as convective time derivative

$$\frac{D}{Dt} = \frac{\partial}{\partial t} + \mathbf{u} \cdot \nabla\,. \tag{2.24}$$

It expresses the Eulerian time derivative (written $\partial/\partial t$) in Lagrangian coordinates.

Equation 2.23 describes a compressible fluid whereas incompressible fluids would have $\nabla \cdot \mathbf{u} = 0$ and therefore $\frac{D\rho}{Dt} = 0$.

In our numerical scheme (chapter 4) the continuity equation 2.23 is written in terms of $\ln \rho$,

$$\frac{\partial \ln \rho}{\partial t} + (\mathbf{u} \cdot \nabla) \ln \rho + \nabla \cdot \mathbf{u} = 0 \; . \tag{2.25}$$

Using a logarithmic density, rather than density itself, ensures purely positive densities. Additionally, the numerical solution will be more stable when density values vary over several orders of magnitude.

2.5 Equation of motion

The conservation of momentum $\rho\mathbf{u}$ may be written as

$$\frac{\partial \rho \mathbf{u}}{\partial t} + \nabla \cdot ((\rho \mathbf{u}) \circ \mathbf{u}) = 0 \tag{2.26}$$

Expanding leads to

$$\rho \frac{\partial \mathbf{u}}{\partial t} + \mathbf{u} \frac{\partial \rho}{\partial t} + \rho \, (\mathbf{u} \cdot \nabla) \, \mathbf{u} + \rho \mathbf{u} \, (\nabla \cdot \mathbf{u}) + \mathbf{u} \, (\mathbf{u} \nabla \rho) = 0$$

This equation can be simplified using the conservation of mass and replacing the time derivative of the density with equation 2.23. This leads to

$$\rho \frac{\partial \mathbf{u}}{\partial t} + \rho \, (\mathbf{u} \cdot \nabla) \, \mathbf{u} = 0$$

the well known Navier-Stokes equation. The momentum of a fluid is changed when different forces act upon it. If the forces are of external nature the momentum conservation equation becomes a balance equation. We add the corresponding terms on the right hand side of equation 2.26

$$\rho \frac{\partial \mathbf{u}}{\partial t} + \rho (\mathbf{u} \cdot \nabla) \mathbf{u} = \sum_i \mathbf{f}_i \tag{2.27}$$

The forces $\mathbf{f}_i$, or more precisely the forces per unit volume, that act on the plasma are:

Gas pressure gradient:	$-\nabla p$
Lorentz force:	$\mathbf{j} \times \mathbf{B}$
Gravitational force:	$-\rho \nabla \Phi$
Coriolis force:	$-2\rho \, (\Omega \times \mathbf{u})$
Centrifugal force:	$-\rho \Omega \times (\Omega \times \mathbf{r})$
Viscous force:	$2\nu \nabla \circ (\rho \underline{S})$
Inertial force:	$-\rho \, (\mathbf{u} \cdot \nabla) \, \mathbf{u}$

The centrifugal and Coriolis forces are just simple examples for a frame of reference that is rotating with Ω in respect to a reference frame at rest. Other scenarios will lead to more complex coordinate transformations. The viscous force is given by the divergence of the stress tensor, which is defined as:

$$\tau_{ij} = 2\nu\rho\underline{S} \tag{2.28}$$

where $\underline{S}$ is the rate-of-strain tensor

$$\underline{S} = \frac{1}{2}\left(\frac{\partial u_i}{\partial x_j} + \frac{\partial u_j}{\partial x_i} - \frac{2}{3}\delta_{ij}\nabla\cdot\mathbf{u}\right) \tag{2.29}$$

and ν is the kinematic viscosity. The latter correlates to the dynamic viscosity μ by $\mu = \rho\nu$.

If we add diffusion in equation 2.23, another term appears. Meaning, if we smear mass, the momentum has to change to. Subsequently the conservation of momentum reads as

$$\rho\frac{\partial\mathbf{u}}{\partial t} + \rho\left(\mathbf{u}\cdot\nabla\right)\mathbf{u} + \mathbf{u}c_\rho\nabla^2\rho = \sum_i \mathbf{f}_i \tag{2.30}$$

in which c_ρ represents a positive and constant mass diffusion coefficient.

2.6 Equation of state

The equation of state for an ideal polytropic gas is given by

$$p = \left(c_p - c_V\right)\rho T \tag{2.31}$$

where c_p and c_V are the specific heat capacities at constant pressure and constant volume respectively. They are correlated to the universal gas constant R and the mean atomic weight $\tilde{\mu}$ or the Boltzmann constant by

$$\left(c_p - c_V\right) = \frac{\mathrm{R}}{\tilde{\mu}} = \frac{k_B}{\tilde{\mu}\, m_p}$$

We can use the adiabatic index $\gamma = \frac{c_p}{c_V}$ to write

$$c_V = \frac{\mathrm{R}}{\left(\gamma - 1\right)\tilde{\mu}}\,.$$

2.7 Energy equation

The last equation of interest is the energy or heat equation. This equation can be written in different forms. The energy equation is first written in terms of entropy

and then transformed into a temperature equation. Entropy S, in a closed system, is a conserved quantity, thus can neither in- nor decrease, so that

$$\frac{\partial S}{\partial t} + \nabla \cdot (S\mathbf{u}) = 0$$

where S is the entropy per unit volume. We can use $S = s\rho$, with s being the entropy per unit mass, and obtain

$$\begin{aligned} \frac{\partial \rho s}{\partial t} + \nabla \cdot (\rho s \mathbf{u}) &= s\frac{\partial \rho}{\partial t} + \rho\frac{\partial s}{\partial t} + s\nabla \cdot (\rho\mathbf{u}) + \rho\left(\mathbf{u} \cdot \nabla\right) s \\ &= s\left(\frac{\partial \rho}{\partial t} + \nabla \cdot (\rho\mathbf{u})\right) + \rho\frac{\partial s}{\partial t} + \rho\left(\mathbf{u} \cdot \nabla\right) s \\ &= \rho\frac{\partial s}{\partial t} + \rho\left(\mathbf{u} \cdot \nabla\right) s \\ &= \rho\frac{Ds}{Dt} \stackrel{!}{=} 0 \end{aligned} \tag{2.32}$$

We can multiply equation 2.32 with the temperature and obtain the conservation of energy

$$\rho T\frac{Ds}{Dt} = -L\ . \tag{2.33}$$

We added on the right hand side the energy loss function L in units of $[\frac{W}{m^3}]$, which describes all sinks and sources of energy.
One can use the thermodynamic potential $\mathrm{d}e = T\mathrm{d}s - \frac{p}{\rho^2}\mathrm{d}\rho$ for the internal energy to express equation 2.33 in the following form

$$\rho\left(\frac{De}{Dt} - \frac{p}{\rho^2}\frac{D\rho}{Dt}\right) = -L \tag{2.34}$$

For an ideal polytropic gas the internal energy e is given by

$$e = c_V T. \tag{2.35}$$

Together with the equation of state (2.31) and mass conservation (2.23) we can rewrite equation (2.34) to

$$c_V \rho T\frac{D\ln T}{Dt} + p\nabla \cdot \mathbf{u} = -L \tag{2.36}$$

Heat sources and sinks used are discussed in the following sections.

2.7.1 Ohmic heating

Because of the sign of the energy loss function the Ohmic heating is

$$L = -\eta\mu_0\mathbf{j}^2\ . \tag{2.37}$$

It is derived in equation (2.19) and plays a major role in the model presented in this work. Ohmic heating, or sometimes called Joule dissipation, is discussed in chapter 6. There the resistivity, or sometimes called magnetic diffusivity, η will also be discussed.

2.7.2 Viscous heating

The loss of kinetic energy by friction and the resulting heating of the plasma is given by the viscous term

$$L = -2\rho\nu\mathbf{S^2} \tag{2.38}$$

The kinematic viscosity ν is assumed to be constant.

2.7.3 Radiative loss

For the optically thin part of the atmosphere the radiative loss is no longer coupled to the radiation field by the radiation transfer equations. The loss can be described as

$$L_r = n_e n_H Q\left(T\right) \tag{2.39}$$

in which $Q(T)$ describes the radiative loss function, n_e and n_H the electron and hydrogen particle densities. In order to calculate the correct shape of that function one needs to know the abundances as a function of geometrical height in the atmosphere. Observations result in estimations, whereas in situ measurements count particles but only in a very small volume and at large distances from the Sun. In our model we use for $Q(T)$ the results from Cook et al. (1989), who rely, among others, on the abundances reported in (Meyer, 1985).

The function $Q(T)$ is shown in figure 2.1 and may be fitted using a piecewise constant slope of the form of

$$Q(T) = \chi T^{\alpha}\ [W\,m^3] \tag{2.40}$$

The first peak is the contribution of hydrogen (Lyman-α), followed by the peaks of carbon, oxygen and iron. The increase of the radiative loss above $\log T/[\mathrm{K}] = 6.5$ is due to Bremsstrahlung. This result emphasizes the importance of the correct abundances used in the calculation because the trace gases have a major contribution.

The right hand side of figure 2.1 indicates the time scale for the radiative loss as a function of height. There are two ways to determine the time scale, first by evaluating the energy loss in a given time interval, or second, by integrating the radiative loss function. The latter is the simplified energy equation:

$$\rho c_V \frac{\mathbf{d}T}{\mathbf{d}t} = -n_e n_i Q(T)$$

We rewrite the equation by using the equation of state (cf. equation 2.31) and substitute the particle densities $n_{e,i}$ (cf. A.4).

$$\frac{\mathbf{d}T}{\mathbf{d}t} = -0.65\frac{\tilde{\mu}(\gamma-1)}{k_B m_p}\rho\, Q(T)$$

where k_B is the Boltzmann constant, $\tilde{\mu} \approx 0.6$ the mean atomic weight and m_p the proton mass. If we now assume that the mass is independent of time and temperature, it is possible to separate the variables

$$-1.54\frac{k_B m_p}{\tilde{\mu}(\gamma-1)}\frac{1}{\rho\, Q(T)}\mathbf{d}T = \mathbf{d}t$$

Therewith, the time it takes until the temperature drops by a factor of $\frac{1}{e}$ can be computed by integration:

$$\tau_{cool}(T_0) = -1.54\frac{k_B m_p}{\tilde{\mu}(\gamma-1)}\frac{1}{\rho}\int_{T_0}^{T_1}\frac{1}{Q(T)}\mathbf{d}T \tag{2.41}$$

where $T_1 = T_0/e$. As indicated, the cooling time depends on the initial temperature. The fact that the density will change when the temperature decreases is neglected, as it can only be accounted for, when doing a full time depending simulation of a solar atmosphere, where the heating is switched off suddenly. In our model we integrate equation 2.41 numerically. The resulting cooling times are shown on the right hand side of figure 2.1 (solid line). Also shown is the cooling time, under the assumption that the energy loss rate for a single time step does not depend on time, meaning that a small change in temperature does not influence the energy loss.

The cooling time in the upper corona is of the order of 2 to 10 hours and decreases towards the transition region due to increasing density. At $z \approx 6\,\mathrm{Mm}$ the temperature is still so high, that the radiative loss function is not to reliable. Below this altitude the temperatures are smaller than $\log T/[\,\mathrm{K}] = 4.5$ and the radiative loss becomes inefficient. Below a temperature of $\log T/[\,\mathrm{K}] = 4.0$ it takes almost infinite time to cool the plasma by radiation only.

Since the cooling time is directly proportional to the density, which varies by two orders of magnitude in the corona, the time scale cover a vast range. This process is slow compared to heat conduction in the corona. Therefore, radiative loss can not cause thermal instabilities mentioned by Parker few decades before.

2.7.4 Heat conduction

Above the photosphere the heat transport by radiative transfer plays a minor role. The Heat flux vector, according to Fourier's law, is

$$\mathbf{q} = -K\nabla T \tag{2.42}$$

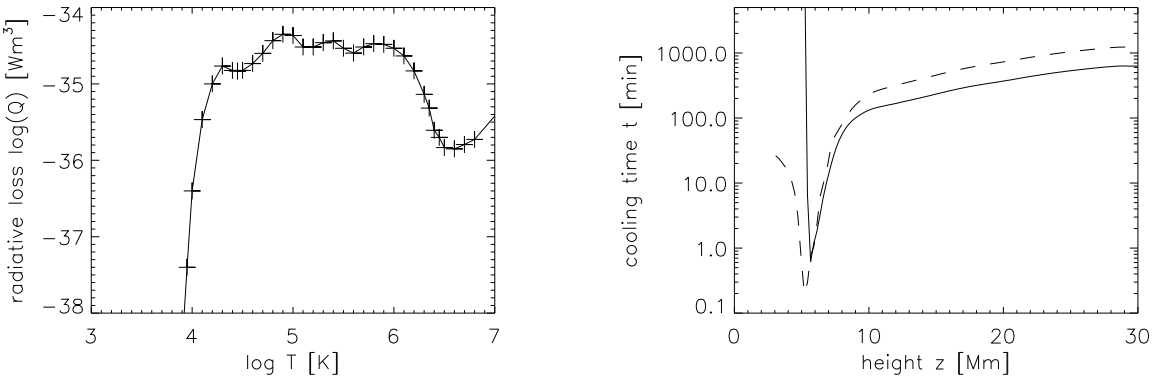

Figure 2.1: *Left*: Piecewise constant slope approximation for radiative loss in the optical thin corona. The intervals are marked by the crosses. *Right*: Radiative cooling time for different heights in the atmosphere based on the temperatures and densities of the model described in this work. Integration of the loss function (solid line) and extrapolation from the loss per time step (dashed line).

in the chromosphere, while it is given by particle conduction in the atmospheric layers above. In an ionized plasma with magnetic fields the thermal conduction tensor K is not diagonal. Thus the heat flux vector can be written as

$$\mathbf{q} = \left(K_\perp \delta_{ij} + \left(K_\parallel - K_\perp\right) b_i b_j\right) \nabla T \tag{2.43}$$

Spitzer and Härm (1953) already conducted numerical models to find a description of $K_\parallel$ and $K_\perp$ depending on Temperature. In their analysis they used a fully ionized hydrogen plasma and Spitzer (1962) gives

$$K_\parallel \approx 2 \cdot 10^{-11} \left(\frac{T}{[\,\mathrm{K}]}\right)^{\frac{5}{2}} \frac{\mathrm{W}}{\mathrm{m\,K}} \tag{2.44}$$

The strong temperature dependency is a result of the large mean free path and the small collision frequency for the almost free traveling electrons.

The perpendicular coefficient is neglected for simplicity. It is smaller by several orders of magnitude in comparison to the parallel coefficient and smaller then the additional isotropic heat conduction described below.

2.7.5 Isotropic heat conduction

In order to stabilize the code we use a isotropic heat conduction of the form

$$q = -\rho |\nabla T| \nabla T \tag{2.45}$$

$$= -T^2 \rho |\nabla \ln T| \nabla \ln T \tag{2.46}$$

The divergence of the heat flux vector is then

$$L = \nabla \cdot \left(T^2 \rho |\nabla \ln T| \nabla \ln T\right) \tag{2.47}$$

2.7.6 Newton cooling

Since we cannot account for a proper energy transport from the photosphere to the upper chromosphere we need to keep the temperature at a constant level. We use Newton's cooling law to obtain a standard temperature profile $T_0(z)$

$$\frac{\mathrm{d}T}{\mathrm{d}t} = -\frac{1}{\tau}\left(T - T_0\right) \tag{2.48}$$

Since we use a logarithmic temperature in the energy equation we write

$$\frac{\mathrm{d}\ln T}{\mathrm{d}t} = \frac{1}{\tau}\left(\frac{T_0}{T} - 1\right) \tag{2.49}$$

where $\tau = \tau\left(z\right)$ and increases with geometrical height. Thus only the lower part of the chromosphere is influenced by Newton cooling. Since earlier works, like Spiegel 1957, have shown that fluctuations in the temperature field will be smoothed by radiation, the time evolution of temperature perturbations can be described as:

$$\frac{\partial T_1}{\partial t} - (\gamma - 1)\frac{T_0}{\rho_0}\frac{\partial \rho_1}{\partial t} \approx -\frac{T_1}{\tau} \tag{2.50}$$

At constant pressure equation 2.50 simplifies to the Newton's Law of Cooling.

3 The model

Our aim is to understand the dynamic processes in the upper atmosphere due to Ohmic heating caused by braiding of magnetic fieldlines. Therefore our model needs to include the solar atmosphere all the way from the photosphere ($z = 0$) to the corona ($z = 30\,\mathrm{Mm}$). The size of the box in comparison to the Sun is shown in figure 3.1. At the bottom of the domain an observed magnetogram is used in the beginning which will evolve with time due to the photospheric motions. The velocity distribution is similar to the granular pattern of the Sun. These motions shuffle around the foot points of the magnetic fieldlines which will result in a non-potential field in the upper atmosphere. This non-potential field induces currents, that are dissipated in the corona and that heat the latter. The sketch in figure 3.2 illustrates the energy flow through the box. We inject energy by photospheric motions, magnetic fields interact with the plasma and radiative loss removes energy from the system. When the losses balance the energy input, or vice versa, the model is in a quasi-stationary state. Meaning energy can still be recycled and redistributed by convection and advection in a highly dynamic atmosphere. The goal is to reach that state to show that the

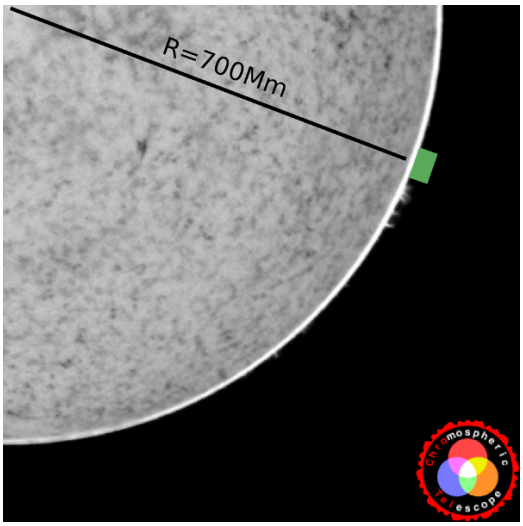

Figure 3.1: Size comparison between the Sun ($R \approx 700\,\mathrm{Mm}$) and the simulated domain $50 \times 50 \times 30\,\mathrm{Mm}^3$ as seen at the solar limb (green square). In this picture, the Sun is observed with ChroTel (Kentischer et al., 2008) in the He 1083 nm emission line (Bethge C., talk at DPG spring meeting, Regensburg 2007).

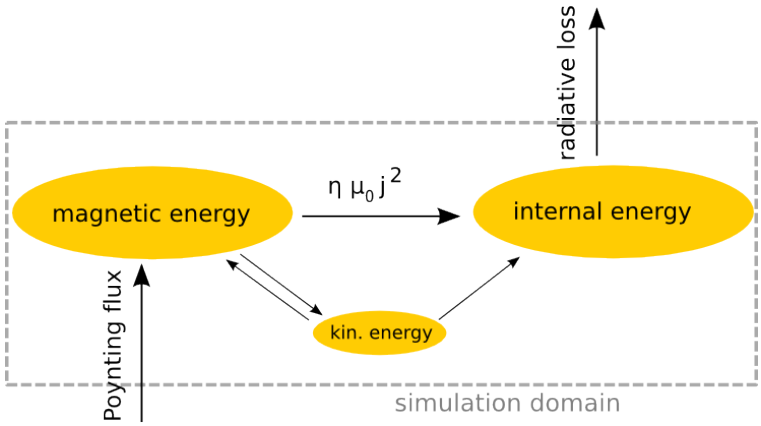

Figure 3.2: Sketch of the energy flow in the domain. The energy input is due to photospheric motions and is balanced by radiative loss in a quasi-stationary state. The complex processes of e.g. heat conduction or advection, are not mentioned, as they simply result in a spatial redistribution of energy.

heating mechanism is able to sustain a corona with a temperature of a million degrees Kelvin.

Since computing power is limited, we have to find a proper setup. Extensive tests have shown that domain sizes of 128^3 grid points can be realized using the computer cluster at the Kiepenheuer Institute. Short time series of domains with a size of 256^3 grid points are also possible. Since the simulation should have a resolution better than the one achieved by observations, and since the resolution should be high enough to resolve the very thin transition region, a box of the size of $50 \times 50 \times 30\,\mathrm{Mm}^3$ was chosen. This gives us a spatial resolution of $\mathrm{d}x \approx 390\,\mathrm{km}$ in the horizontal direction and $\mathrm{d}z \approx 230\,\mathrm{km}$ in the vertical respectively.

This setup is therefore similar to the initial condition used by Gudiksen and Nordlund (2002). A comparison to their results can then be used as a test for our code. Our first simulations based on the same initial condition, but different numerical schemes, showed a good agreement. The Active Region used at the bottom layer in the model of Gudiksen and Nordlund (2005) did not include chromospheric network flux. This is a result of the scaling which leads to a loss of small structures. Observations however show a variety of connections between Active Regions and network flux. Therefore, we added a quiet Sun magnetogram to the initial condition. No spatial scaling is applied but the magnetic field strength is enhanced by factor of two, in order to fit into the scaled Active Region. This gives the expectation of a more complex atmosphere. The left hand side of figure 3.3 shows the compounded image.

We tested the model with several different setups, varying resolution, resistivity η and other physical parameters. In addition, simplified models which do not invoke the energy equation are computed by J. Warnecke (Diploma thesis). These models

help to understand the heating process of the corona and save computation time by using the evolved magnetic field as initial condition in more complex simulations. A detailed description of parameters used for the models is given in the appendix.

In order to compare our results to observations, the simulation has to include as much physics as possible. Therefore, we solve the equation of mass and momentum conservation, as well as the energy equation and the induction equation as mentioned in chapter 2. The most important physics is included in the energy equation, in which we account for the optical thin corona and introduce radiative loss. Furthermore, heat conduction is dominated by the Spitzer heat conduction in both, simulation and on the Sun. The strength of this kind of heat conduction defines the height of the transition region. Heat, carried by fast electrons, flows down to the photosphere where it is radiated away in dense regions. An increase in heat flux results in higher densities in the region where the equilibrium between radiation and heating is achieved. The transition region, where the temperature is around $\log T/[\,\mathrm{K}] = 5.0$ is displaced to lower heights and the chromosphere becomes thinner. Hence, the heat conduction determines the density and pressure in the transition region and corona. In order to compare the results with observations and to reproduce the real atmospheric stratification it is crucial to implement the Spitzer heat conduction properly.

We include four different layer in our box. The lower most layer is the photosphere, above it, followed by the chromosphere, is found the transition region and the corona on top of it. Even though we are only interested in the heating mechanism in the solar corona each layer plays an important role in this process. The photosphere is the place where the foot points of the magnetic fieldlines are shuffled around. Without these motions no braiding of magnetic fieldlines and thus no heating would occur. In the chromosphere the physics is to complex to be treated properly in the MHD assumption. In order to keep things simple, we treat this layer only as a heat and momentum reservoir and exclude it in the spectral analysis. The height of the third layer, the transition region, determines the pressure and density in the corona. Even though this is a very thin layer, it is crucial, not only physically, but also numerically as the gradient in temperature is very high and needs to be resolved in the simulation to avoid numerical instabilities. The corona, which extends over more than three quarters of the model domain, is the layer where the analysis should be comparable to observations. The discussion in this work mainly reflects results concerning the transition region and the corona.

3.1 Initial conditions

To save computational time we start with an existing temperature and density stratification. It was taken from previous simulations (Gudiksen and Nordlund, 2005) and is shown on the right hand side of figure 3.3. The chosen temperature profile

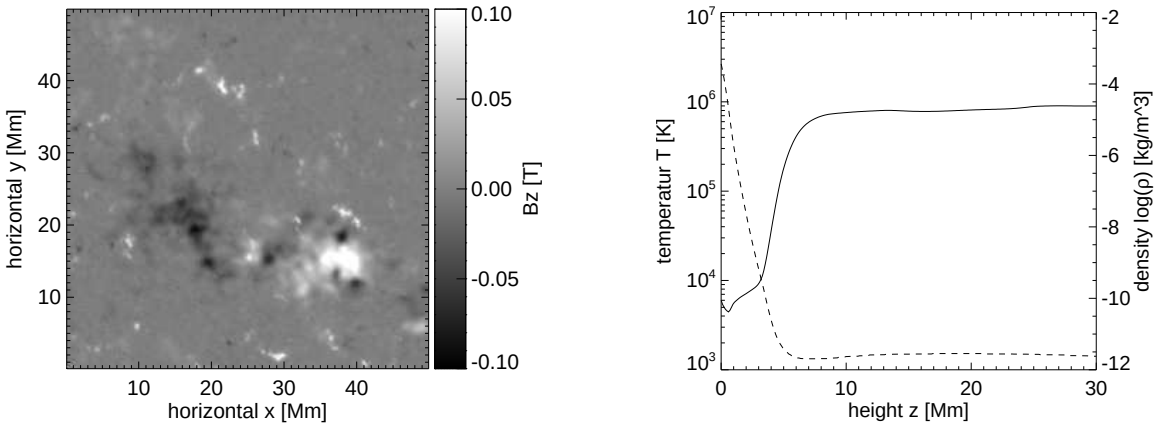

Figure 3.3: *Left*: Initial magnetogram. Spatially scaled down Active Region with additional network flux. *Right*: Initial temperature (solid line) and density stratification (dashed line).

starts at the photosphere with $T \approx 6000\,\mathrm{K}$, includes the chromospheric minimum, the transition region and reaches temperatures of $T \approx 10^6\,\mathrm{K}$ in the corona. The density drops from $\rho_0 = 3 \cdot 10^{-4}\,\frac{kg}{m^3}$, (cf. Stix (1989)), to $\approx 10^{-12}\,\frac{kg}{m^3}$ in the corona. This initial atmosphere is like the real corona not in hydrostatic equilibrium. In the beginning of the simulation we provide a MDI-image (Michelson Doppler Imager (Schou et al., 1994)) which will be used to create a potential field extrapolation to fill the box with magnetic flux. The MDI image corresponds to the line of sight component of the magnetic field vector $B_z(x, y, z = 0)$. Thus, the extrapolation returns the full vector, of the vector potential, at each grid point in the domain. A short derivation of the potential field extrapolation can be found in appendix A.5 and a more detailed description of the concept in Bracewell (1965). There is no need to use more sophisticated extrapolations, e.g. a force free constant α field, since the evolution of the model results in a non force free field anyway.

For our purposes we chose a scaled down Active Region (left-hand side of 3.3) constructed from a MDI image of quiet Sun. It comes from the model by Gudiksen and Nordlund (2002), after their initial start-up phase. Their initial condition is a scaled down Active Region from August 2002 and had a original size of $225 \times 225\,\mathrm{Mm}^2$.

First we reproduced their results using the same initial conditions but with different numerical code. Then due to lack of small scale features in the magnetogram we added chromospheric network flux from a second set of MDI observations.

3.2 Boundary conditions

One of the most important, and widely discussed aspects of numerical astrophysics are the boundary conditions. Therefore, we describe all the boundary conditions used

in great detail below. If we assume a periodic magnetogram at the lower boundary, we can use periodic boundary conditions for all other physical values in the horizontal direction. In the vertical direction we have to analyze which boundary condition satisfies the real physical requirements. Hence, at first, we describe the physics and then check how variables of the code depend on it. The numerical boundary conditions are discussed in the appendix A.1.2.

3.2.1 Photospheric boundary layer

We place the photosphere at the lower boundary of our simulation domain. An obvious property of the photosphere is the motion of the convection, visible as granules. Since we do not include this convection itself in our simulation we have to provide a velocity field matching the observations.

Photospheric driver

We use an application provided by Gudiksen and Nordlund (2005) to calculate photospheric horizontal velocities with a power spectrum similar to observed velocity spectra, cf. figure 3.4. Velocity maps deduced from observations are restricted in resolution. Not only the observing technique but also the data analyze (local correlation tracking) limit the spatial scale to a few thousand kilometers. On the other hand, numerical simulations of the solar convection reach much higher resolution. Thus for scales below $\approx 5\,\mathrm{Mm}$ the power spectrum matches simulations by Stein and Nordlund (1998). The deviation from the $\mathbf{k} \sim \mathbf{l}$ law implies less energy at small scales. A three dimensional Fourier analysis $(x - y - t)$ produces a so called $\mathbf{k}$-ω-diagram. The procedure is explained in A.2 and should not be mistaken with the $\mathbf{k}$-ω-diagram used in helioseismology.

On the left hand side of figure 3.5 the power distribution in the spatial and temporal frequency domain is depicted. At small spatial frequencies two distinguished temporal frequencies are visible. A cut along one spatial frequency, cf. right hand side of figure 3.5, reveals a third temporal frequency. These can be assigned to the three layers of granulation with lifetimes between 5 min and 70 min as described in detail in Gudiksen and Nordlund (2005).

Additionally, the motion of the foot points are damped anti proportional to the magnetic field strength. Since it is observed (Berger et al., 1998) that velocities are smaller in places of strong magnetic fields, we use a damping factor

$$q = \frac{1 + \frac{1}{\beta^2}}{1 + 3\frac{1}{\beta^2}} = \frac{\beta^2 + 1}{\beta^2 + 3} \tag{3.1}$$

in which β, known as plasma beta, is defined as

$$\beta = \frac{p}{B^2 \,/\, 2\mu_0} \tag{3.2}$$

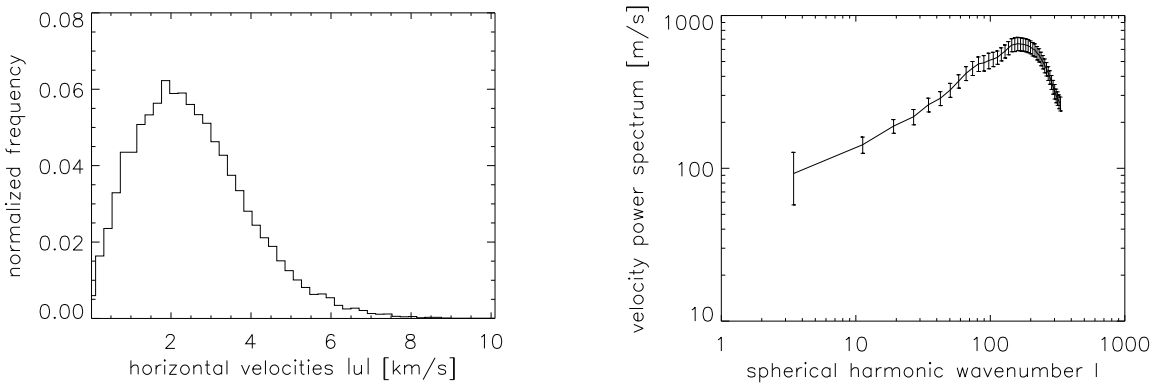

Figure 3.4: *Left*: Histogram of absolute horizontal velocities with $u_{rms} \approx 3\frac{km}{s}$ and $u_{mean} \approx 2.6\frac{km}{s}$ for given time. *Right*: Averaged power spectrum for the absolute horizontal velocities over the spherical harmonic wave number l ($l(l+1) = k^2R_0^2$, $R_0 \approx 700\,\mathrm{Mm}$). To create this plot, we used 120 snapshots with time difference of 30 s. The maximum is located at $l \approx 152$, which corresponds to a spatial scale of $\approx 4.58\,\mathrm{Mm}$.

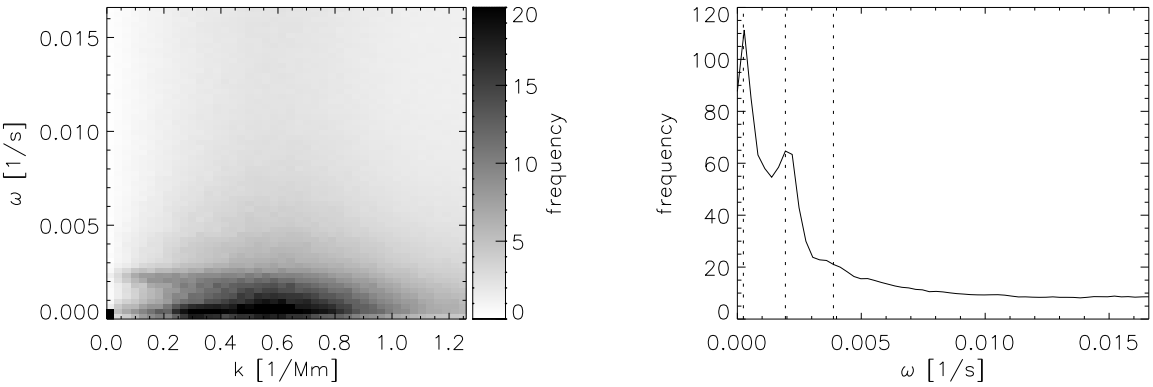

Figure 3.5: *Left*: k-ω-diagram of the absolute horizontal velocity for a time period of $1\,h$ with a cadence of 30 s. *Right*: Cut through the k-ω-diagram at k= $0.2\frac{1}{\mathrm{Mm}}$. Vertical lines (dotted lines) indicate the three different lifetimes of granules. The periods are $T_1 \sim 5\,\mathrm{min}$, $T_2 \sim 8.3\,\mathrm{min}$ and $T_3 \sim 70\,\mathrm{min}$.

This reduces the velocities by one third for strong magnetic fields. On the left hand side of figure 3.4 the velocity distribution for a given point in time is illustrated. The distribution has its maximum at approximately 2 km/s and gives a mean value of 2.6 km/s.

The vertical component of the velocity in the photosphere is zero, thus there is no mass flux into the box. Any flux into the domain would require an assumption about the mass and internal energy of the incoming plasma. The mass fraction needed to feed the solar wind is negligible in comparison to the mass density at photospheric level.

Magnetic field

Since we use a potential field extrapolation at the beginning, the time evolution is given by the induction equation 2.12. The velocities in equation 2.12 are derived from the velocity field described above. Since the resistivity used in the domain would reduce the total magnetic flux through the bottom layer, η is set to zero at the bottom layer and the induction equation becomes

$$\frac{\partial \mathbf{B}}{\partial t} = \nabla \times (\mathbf{u} \times \mathbf{B}) \tag{3.3}$$

For that equation the frozen-flux theorem of Alfvén (1943) applies:

> *In a perfectly conducting fluid ($Rm \gg \infty, \eta = 0$), magnetic fieldlines move with the fluid: the fieldlines are ' frozen' into the plasma.*

This theorem states that plasma motions along the fieldlines do not change the field, while motions transverse to the field carry the field with them. Alfvén showed in his work that for the given assumption, the magnetic flux does not change in time respecting any closed contour moving with the plasma.

Since the solar magnetic flux is based deep in the convection zone, which is not included in our model, the almost random plasma velocities in the photosphere would corrode the Active Region and spread the magnetic flux all over the photosphere. The lifetime of the Active Region would be much shorter (less than an hour) than the typical lifetimes on the Sun (up to several days). Therefore we need to stabilize the Active Region, which is done by updating the vertical magnetic field by a fraction of the original one. Thus the deviation from the initial magnetogram can be controlled in a way that the simulated evolution looks like an observed evolution of a small Active Region on the Sun. The Active region would look like the initial magnetogram after a certain time when the convective motions stop.

3.2.2 Top layer

A mass flow through the top layer of the simulation domain is prohibited. As mentioned before this prevents wrong assumption on the incoming plasma. In order to suppress a net mass flux in the horizontal direction and a global shear of the magnetic field, the horizontal motions in the top layer are forced to be zero. Density and temperature may change at the top layer, but will be forced to have no gradient at the boundary. Since the heat flux depends on the temperature gradient there is no heat flux into the domain or out of the domain.

The magnetic field configuration at the top boundary is a major task which is not entirely solved yet. Not only the numerical code used in this work struggles with it, but also most of other codes encounter problems. In our code we have to extend the field into three outer layers (grid points). Short below the top layer the magnetic

field is in a non force free, dynamic and highly structured state. The extension on top should fit not only the curvature of the magnetic field or the magnetic energy density but also the current vector and its density. Since there is no solution yet, a potential field extrapolation is used. This induces additional currents, which are neglected during simulation, but as a result, the magnetic fieldlines may move freely at the upper boundary.

3.3 Initial phase

Since we start with a plane parallel atmosphere it is necessary to go through a start-up phase before analyzing the data. Starting with the initial and boundary conditions as described above, the system evolves self-consistently for one hour solar time. Only the boundary conditions influence the model during that time. After this phase, assuming the initial condition has been forgotten, data is collected for another time period of one hour. The length of the start-up phase is determined by different deliberations. Obvious criteria are the net mass flux and the heating rate in the domain. Both are illustrated in figure 3.6. It takes at least 30 minutes before the mean heating rate, which is directly proportional to j^2, reaches a value that is not lowered during the rest of the simulation. It still alternates, as a result of the dynamics in our model. Due to the initial stratification and the lag of heating during the initial phase, the corona is unstable in the beginning. After about 40 minutes the corona stops to sink down and during the rest of the time there is no mass loss of the corona. Starting our analysis one hour after the initial condition allows the system to find a quasi-stationary state, where dynamic processes are still observable. Not all quantities, e.g. the root mean square value of the velocity, show this temporal behavior. If not explicitly mentioned we refer to the begin of the second phase when we speak about time zero.

3.4 Plasma parameters

In our numerical model we use the equations resulting from the magneto-hydrodynamic approximations. We investigate in this section the assumption in detail. The discussed parameters are also auxiliary in the next chapters.

A plasma is mostly defined by three parameters. The Debye length λ_D describes the distance over which significant charge separation can occur, the plasma frequency ω_e occurs when quasi-neutrality is disturbed and the mean free path λ is the medium length of a path covered by a particle between subsequent impacts.

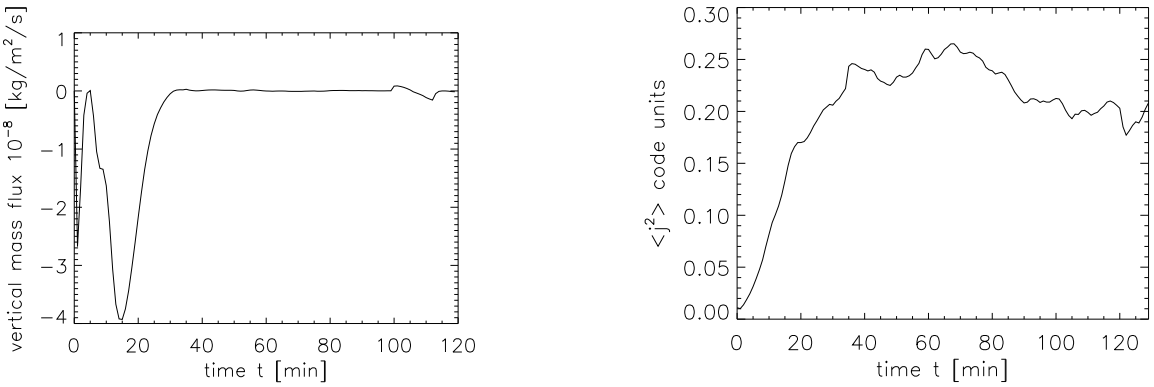

Figure 3.6: *Left*: Mean vertical mass flux in the corona versus time. The first hour reflects the initial start up phase, the second hour is used for data production. *Right*: Average j^2 value of the domain depending on time. Numbers are given in internal units of the code.

Debye length

For an ideal plasma the number of particles in a sphere with radius λ_D has to be large. In a such a Debye sphere the number is given by

$$N_D = n\left(\frac{4}{3}\pi\lambda_D^3\right) = \left(\frac{\epsilon_0}{e^2}\right)^{3/2}\frac{(k_B T_e)^{3/2}}{n^{1/2}}\,,$$

where T_e is the electron temperature which can be approximated by the plasma temperature. In our simulations we find values from $\log N_D = 4$ to $\log N_D = 8$ with a mean value of $\log \bar{N_D} = 7.8$ for the corona. This fulfills the criteria of large particle numbers in a Debye sphere.

Plasma frequency

The plasma frequency has to be smaller than all other time scales of interest:

$$\omega_e = \sqrt{\frac{e^2 n_e}{m_e \epsilon_0}}$$

It is proportional to the square root of the electron number density and is in the order of $\omega_e = 10^9\,\mathrm{Hz}$ in the corona and increases downwards to a maximum value of $\omega_e = 10^{13}\mathrm{Hz}$ at the photosphere. In comparison to the time step of $\mathrm{d}t \approx 10^{-5}\,\mathrm{s}$ to $10^{-3}\,\mathrm{s}$, which is the smallest timescale of the simulation by definition, the plasma frequency is even faster by several orders of magnitude.

Mean free path

The mean free path for an electron is defined as

$$\lambda_e = u_e \tau_{ei} \,, \tag{3.4}$$

where u_e is the electron velocity and τ_{ei} the electron-ion collision time. Following Boyd and Sanderson (2003), the effective range of the electric fields increase to the Debye length and therefore the electrons undergo more interactions. Thus the collision frequency is increased. For a electron with thermal speed Boyd and Sanderson (2003) gives as result:

$$\begin{aligned} \lambda_e &= 1.44 \cdot 10^{17} \frac{(T/[\mathrm{eV}])^2}{\ln\Lambda \; n/[\frac{1}{\mathrm{m}^3}]} \,\mathrm{m} \\ \lambda_e &\approx 1 \cdot 10^{8} \frac{(T/[\,\mathrm{K}])^2}{n/[\frac{1}{\mathrm{m}^3}]} \,\mathrm{m} \end{aligned}$$

The Coulomb logarithm $\ln\Lambda$ is in the order of 10 and the density and the temperature can directly be used from our data. Thus for our simulation the mean free path reaches values up to 6 Mm, cf. figure 3.7. The numbers given are only for electrons traveling along magnetic fieldlines. Motions perpendicular are forced into gyrations around the fieldlines. The mean free path is then given by the Larmor radius which is in the order of centimeters in the corona and decreases rapidly towards the photosphere (cf. right panel of figure 3.7).

The motions parallel to the magnetic fieldlines are resolved since the time step scales mostly with the heat conduction term. Meaning the inverse time step is proportional to the temperature to the power of $\frac{5}{2}$. In this dependency the thermal velocity ($\sim \sqrt{T}$) and the collision frequency ($\sim T^2$) are combined. Considering a thermal electron with a speed of $8000\,\frac{\mathrm{km}}{\mathrm{s}}$ and a time step of 1 ms. The electron travels a distance of 8 km which is well below the spatial resolution of the simulation. The grid spacing of our model is in the order of hundreds of kilometers. We conclude that the large mean free path along magnetic fieldlines is considered by the small time step given by the Spitzer heat conduction. It is therefor crucial to implement and use the proper description of the heat flux as given in Spitzer (1962). In section 6.3 we discuss the influence of non thermal electrons on the results of our numerical experiment. Further discussion about the heat transport and the heating mechanism are found in chapter 6.

Charge neutrality

We have to proof that charge neutrality is valid in our simulation domain. Therefore we evaluate equation 2.7 using the density and plasma velocities at each grid point. The smallest dimension we resolve is the grid spacing $\mathrm{d}x$, so we use this as typical

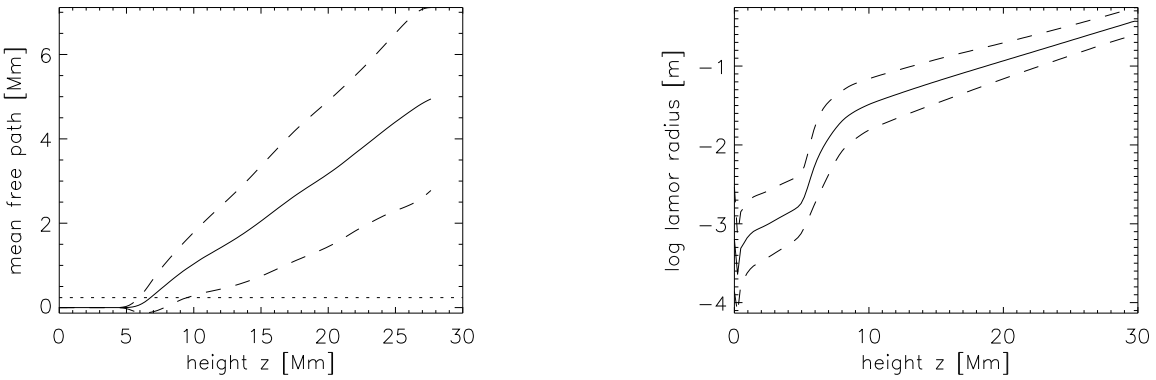

Figure 3.7: *Left*: Electron mean free path, horizontal mean (solid line), one sigma deviation (dashed lines) and the minimum grid spacing (dotted line). *Right*: Horizontally averaged electron Larmor radius (solid line) and one sigma deviation (dashed lines).

length scale. Altogether we find that the fraction of right hand side to left hand side of equation 2.7 is everywhere smaller than 10^{-10}. This satisfies the assumption of charge neutrality.

4 Numerical algorithm

To conduct our model we use the Pencil Code (Brandenburg and Dobler, 2002) as numerical algorithm. It was started at the Turbulence Summer School of the Helmholtz Institute in Potsdam (2001). Primarily developed by Axel Brandenburg and Wolfgang Dobler the group of people improving the code is still growing. Even if there are plenty of 3D-MHD codes with different purposes available we choose the Pencil Code because of several good reasons.

The most important is, that the code is build for massively parallel computing on simple Linux cluster which could be build of common desktop computers. Therefore, an affordable computer cluster could be realized at the Kiepenheuer Institute. For the parallelization by decomposing the domains, MPI (Message Passing Interface) is used. Several free implementations for MPI are available today.

The code solves the partial differential equations for a resistive and compressible plasma, e.g. induction equation and momentum equation, on a equidistant or non-equidistant grid. The physics is distributed in different modules, so that applications are manifold. The code was tested with up to 8000 CPU on bigger computer clusters and shows a good scaling.

A more detailed description of the numerical method can be found either in the manual of the code or in Brandenburg (2003). The most important numerical methods are discussed briefly in this chapter.

4.1 Spatial and temporal derivatives

To solve the partial differential equations (4.3) the spatial derivatives on the right hand side are calculated using a 6th order scheme and a Runge-Kutta third order scheme describes the time evolution.

Spatial derivatives

The first and the second spatial derivatives can be expressed as

$$y_0^{(1)} = \Sigma_{p=-n/2}^{n/2} w_p y_p \ ,$$
$$y_0^{(2)} = \Sigma_{p=-n/2}^{n/2} \hat{w_p} y_p \ ,$$

where $n = 2, 4, 6, ...$ is the order and p the position in respect to the point of interest. The coefficients w_p and $\hat{w_p}$ can be calculated from the requirement of an exact

solution for the monomials $y = 1$, $y = x$,..., $y = x^n$ at the position x_0. For this computation, equidistant grid points are required. In order to resolve the steep temperature gradient in the transition region, we need a high spatial resolution. Not to increase the number of grid points to much we added a non-equidistant grid description into the code. The grid z is therefore a function of space itself $z = z(\zeta)$, where ζ are equidistant grid points. The first and second derivatives can then be calculated by

$$\frac{df}{dz} = \frac{df}{d\zeta}\frac{d\zeta}{dz} = \frac{1}{z'}f'(\zeta) \ , \qquad \frac{d^2f}{dz^2} = \frac{1}{z'^2}f''(\zeta) - \frac{z''}{z'^3}f'(\zeta) \ . \tag{4.1}$$

The first and second derivatives of z are known and the rest can be computed using the standard scheme for the spatial derivatives. For $z = \zeta$ the grid is not changed and stays equidistant. Typically, we use $z \sim \sinh(\zeta)$, where the reflection point of the hyperbolic sine function is set to the point where the highest resolution is needed.

Using a 6th order scheme is a compromise between accuracy and run time as well as memory usage. Higher order schemes would increase the accuracy slightly, but the computation time would increase quiet fast. Calculations concerning this problem can be found in Brandenburg (2003).

Time evolution

The partial time derivative describes the evolution of the system. Unlike the spatial scheme it has to be asymmetric. There is no information about the past. So, a step in time is divided into sub steps. Here we use a third order scheme meaning three sub steps yield one time step. The scheme is written as a 2N scheme in which only 2 copies of all variables have to be kept in memory. This makes the code very cache efficient.

The length of a time step is defined by the Courant criterion.

$$\delta t = min\left(c_{\delta t}\frac{\delta x_{\min}}{U_{\max}}, c_{\delta t,v}\frac{\delta x_{\min}^2}{D_{\max}}, c_{\delta t,s}\frac{1}{H_{\max}}\right) \tag{4.2}$$

where $\delta x_{\min}$ is the minimum grid spacing, $U_{\max}$ the maximum velocity, $D_{\max}$ the maximum diffusivity and H represents the total right hand side of a partial differential equation. The coefficients c are in the order of unity but have an upper limit so that the scheme is stable. It goes back to Courant et al. (1928), who find a condition (CFL condition) for convergence while solving partial differential equations numerically. E.g. $c_{\delta t,v} = 0.4$ in the 6th order in space and 3rd order in time scheme used in this work. The maximum velocity can either be the plasma velocity, the sound speed or the Alfvén velocity. Also, the maximum diffusivity is either determined by the magnetic or thermal diffusivity.

4.2 The equations

This is a summery of the equations as they are used in the code. The detailed description how they are derived can be found in chapter 2. On the right hand side are all spatial derivatives whereas the time derivatives, which are evolved by the Runge-Kutta time stepping, are on the left hand side. In total it is a set of eight equations, the momentum, mass and energy balance as well as the induction equation.

$$
\begin{aligned}
\frac{\partial \mathbf{u}}{\partial t} =& -(\mathbf{u}\cdot\nabla)\mathbf{u} + \frac{1}{\rho}\left[-\nabla p + \mathbf{j}\times\mathbf{b} - \rho\nabla\Phi + 2\nu\nabla\circ(\rho\underline{S})\right] \\
\frac{\partial \ln\rho}{\partial t} =& -\nabla\cdot\mathbf{u} - (\mathbf{u}\cdot\nabla)\ln\rho + c_\rho\left((\nabla\ln\rho)^2 + \nabla^2\ln\rho\right) \\
\frac{\partial \ln T}{\partial t} =& -(\mathbf{u}\cdot\nabla)\ln T - (\gamma-1)\nabla\cdot\mathbf{u} + \frac{1}{\tau}\left(\frac{T_0}{T} - 1\right) \\
&+ \eta\mu_0\mathbf{j}^2 + 2\rho\nu\mathbf{S}^2 \\
&+ \frac{\gamma}{c_p\rho T}\left[-\left(\frac{0.8\rho}{m_p}\right)^2 Q(T) + \nabla\cdot\left(K_0 T^{\frac{5}{2}}\mathbf{b}(\mathbf{b}\cdot\nabla T)\right)\right. \\
&\left.+\nabla\cdot(c_p\chi\rho\nabla T) + \nabla\cdot(c|\nabla T|\nabla T)\right] \\
\frac{\partial \mathbf{A}}{\partial t} =& \mathbf{u}\times(\nabla\times\mathbf{A}) + \eta\nabla^2\mathbf{A}
\end{aligned}
\tag{4.3}
$$

The parameters used in the equations above are:

γ	$= \frac{5}{3}$	adiabatic coefficient for ideal gas
m_p	$= 1.67\cdot10^{-27}\,\mathrm{kg}$	proton mass
c_p	$= \frac{\gamma}{\gamma-1}\frac{\mathrm{R}}{0.595\,m_p}$	heat capacity at constant pressure
ν	$= 2\cdot10^{10}\,\frac{\mathrm{m}^2}{\mathrm{s}}$	kinematic viscosity
η	$= 10^{10}\,\frac{\mathrm{m}^2}{\mathrm{s}}$	magnetic diffusivity
c_ρ	$= 10^{8}\,\frac{\mathrm{m}^2}{\mathrm{s}}$	mass diffusion
χ	$= 2.5\cdot10^{8}\,\frac{\mathrm{m}^2}{\mathrm{s}}$	heat diffusion
K_0	$= 2\cdot10^{-11}\,\frac{\mathrm{J}}{\mathrm{K\,s\,m}}$	Spitzer heat conduction coefficient
c	$= 10^{-5}\,\frac{\mathrm{J}}{\mathrm{K}^2\,\mathrm{s\,m}}$	isotropic heat conduction coefficient

All values and parameters are unified in the code using conversion factors which are based on three fundamental units and the assumption that $c_p = 1, \gamma = \frac{5}{3}$ and $\mu_0 = 1$ in the code.

4.3 Dimensionless parameters

Dimensionless parameters are useful to describe the proportionality in time or space of different physical processes. But they are useful as well as criteria in numerical simulations. If the parameter R compares two time scales, then the restriction given by the number of grid points n_x is

$$\frac{1}{\mathrm{n}_x} < \mathrm{R} < \mathrm{n}_x \ ,$$

If the parameter R does not satisfy this equation one process is much less important and thus can be neglected. The number R is not only a tool to analyze the data but also helps to find the right parameters, for example the viscosity, for the simulation.

Reynolds number

The Reynolds number is defined as ratio of the inertial to the viscous force. Or it can be interpreted as the comparison of the advective to the viscous time scale

$$\mathrm{Re} = \frac{u\, l}{\nu}, \tag{4.4}$$

where l is a typical length scale, u a typical velocity and ν the kinematic viscosity. If the value exceeds a problem depending value Re_{crit} the flow changes from a laminar to a turbulent state. The Reynolds number can also be understood as the fraction of momentum convection to momentum diffusion. For a stable simulation the numerical Reynolds number should be in the order of unity and the typical length scale corresponds to the grid spacing and the typical velocity is replaced by $\mathbf{u}_{\max}$.

Since we start with zero velocity we have to assume the evolution of the numerical Reynolds number. Therefore we estimate a typical velocity during the simulation. The coronal velocities can reach values up to 150 km/s. So the viscosity can be calculated trough

$$\begin{aligned} \mathrm{Re} &= \frac{\mathbf{u}_{\max}\delta x}{\nu} \approx 1 \\ \nu &= \mathbf{u}_{\max}\mathrm{L}_x\frac{1}{\mathrm{n}_x} \\ &= 7.5 \cdot 10^{12}\frac{m^2}{s}\frac{1}{\mathrm{n}_x} \\ &= 5.86 \cdot 10^{10}\frac{m^2}{s} \end{aligned}$$

where we used $\mathrm{L}_x = \mathrm{n}_x \delta x$ and $\mathrm{n}_x = 128$ This first guess can be adjusted to increase or decrease the resolution of plasma flows keeping in mind numerical stability. The kinematic viscosity used in the code is comparable to values in the solar corona.

Magnetic Reynolds number

The magnetic Reynolds number is defined as the fraction of advection to diffusion of magnetic fields

$$\mathrm{Rm} = \frac{ul}{\eta} \tag{4.5}$$

where η is the magnetic diffusivity. As described above we can make a first guess using the definition of the magnetic Reynolds number. The result is larger by several orders of magnitude in comparison to solar values.

Mach number

The Mach number is defined as the fraction of the plasma velocity to the sound speed.

$$\mathrm{Ma} = \frac{u}{c_s} \tag{4.6}$$

For Mach numbers greater than 0.3 one has to account for compressible effects of the fluid. We find Mach numbers between 0.01 and 1 in our numerical model. Thus we cannot assume $\nabla \cdot u = 0$ what describes an incompressible fluid.

Lundquist number

The Lundquist number is defined as

$$\mathrm{Lu} = \frac{v_\mathrm{A} l}{\eta} = \frac{v_\mathrm{A}/l}{\eta/l^2} = \frac{t_{diff}}{t_{adv}} \tag{4.7}$$

where $v_\mathrm{A} = \frac{B}{\sqrt{\mu_0 \rho}}$ is the Alfvén speed. Although this dimensionless constant has the appearance of a Reynolds number, either hydrodynamic or hydro magnetic, it is neither. Physically, the Lundquist number is a measure of the effective Lorentz force relative to the resistive force due to magnetic diffusion. When magnetic fields dominate; i.e. the magnetic energy has been inserted over a distance L that is much smaller than the natural distance for the system, then the Lundquist number will be large. As the magnetic field eventually diffuses over a much larger distance scale, the Lundquist number will become very small and a conventional hydrodynamic shock may emerge. The Lundquist number in the model corona is in the order of 10^3. Below the transition region it decreases rapidly below unity. The Lundquist numbers found on the Sun are larger by several orders of magnitude. It demonstrates the fact that the magnetic field dominates the dynamics and the structures of the corona in our model and on the Sun.

5 The solar atmosphere in our model

In this chapter we present global and general results of our numerical simulations. We have the complete set of physical parameters that describe a hydrodynamic fluid with a magnetic field. There are therefore many possible investigations. We focus on the temperature and density stratification and discus the physics appearing in the partial differential equations. Additionally, we continue in the forward model approach and present results of the line emission synthesis. The heating mechanism and the influence of the magnetic field will be discussed in detail in chapter 6 and chapter 7.

In order to reach a quasi-stationary state we let the model relax for one solar hour after initialization (cf. section 3.3). For a subsequent analysis we let the system evolve for another solar hour and then take snapshots of all physical parameters with a cadence of 30 seconds. This way we obtained 120 snapshots which are used to derive the results presented in this thesis.

Since the Active Region at the lower boundary of the simulation domain has an infinite lifetime, the model is able to reach a quasi-stationary state. The total energy, the sum of kinetic, thermal and electromagnetic energy, is constant on average inside the box. The energy is injected by photospheric motions and will be extracted by radiative losses. Even though an averaged coronal parameter varies slightly with time, the corona is highly dynamic on small scales. Thus averaged quantities, for example temperatures and densities, show only a small dependence on time, cf. figure 5.1.

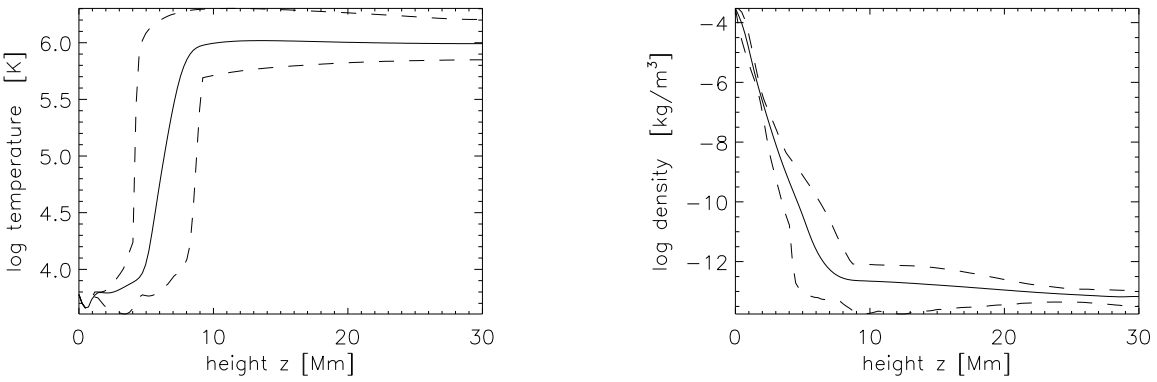

Figure 5.1: *Left*: Horizontally averaged temperature profile (solid line) and minimum and maximum values (dashed lines) at each height. *Right*: Horizontally averaged density profile (solid line) and minimum and maximum values (dashed lines) at each height.

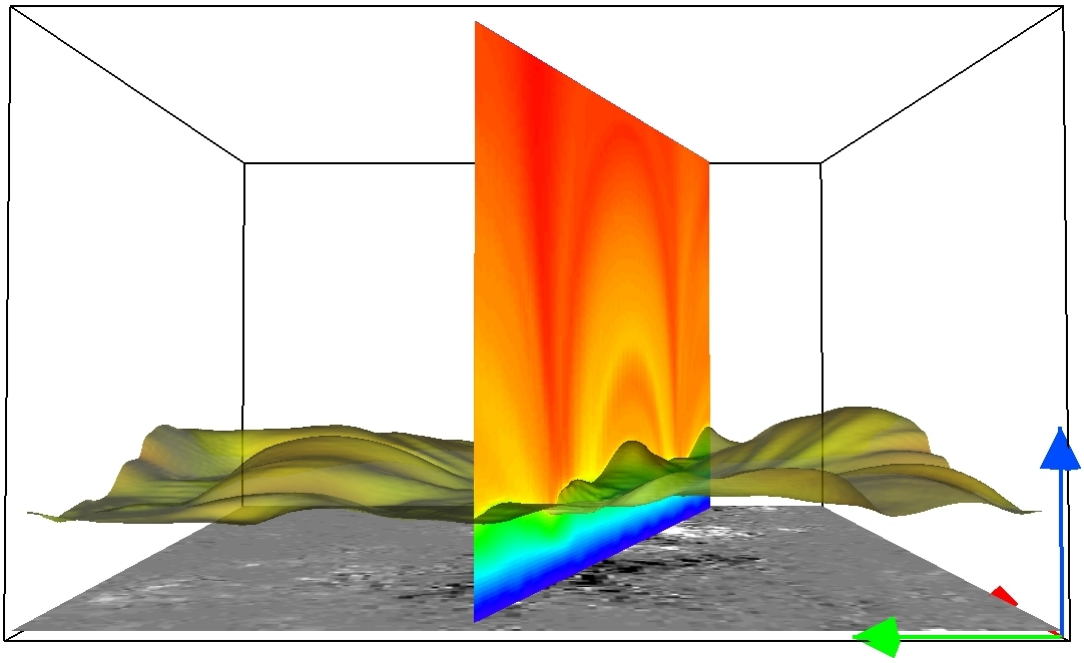

Figure 5.2: Visible impression of the transition region height (using the tool VAPOR (Clyne and Rast, 2005)). Isosurface of temperature at $\log T/[\mathrm{K}] = 5.0$ and a cut trough the box showing the density above the main magnetic polarities (greyscale bottom picture). Color code of the isosurface and the plane indicates logarithmic densities. The box size is $50 \times 50 \times 30\,\mathrm{Mm}^3$.

Our model corona has a typical temperature of one million Kelvin and an average density of $10^{-13}\,\mathrm{kg/\,m^3}$. This density is found at the lower end of the corona above an Active Region or at the higher end of the corona above the quiet Sun. Since the underlying magnetogram is scaled down, and thus represents a magnetic field with less influence on the corona, its density is smaller than inferred from observational results. The base of our corona and the height of the strong corrugated transition region is located at $z_0 \approx 16\,\mathrm{Mm}$ above the photosphere. Figure 5.2 illustrates an isosurface at $\log T/[\mathrm{K}] = 5.0$ together with the underlying magnetogram and a cut through the box. The color code shows the density variation. In the vertical cut one can see dense loops connecting the main polarities and small fluctuations of density along the temperature isosurface. The temperature profile, in the left panel of figure 5.1, also demonstrates the temperature minimum ($z = 0.5\,\mathrm{Mm}$), and the chromosphere. As a result of the Newton cooling term, no deviation from the mean temperature exists at the lower boundary. This extra term in the energy equations adjust the temperature to a given atmospheric model, resulting in a chromosphere, that works as a heat and momentum reservoir, matching solar observations.

The velocities in the corona reach values up to $100\,\mathrm{km/\,s}$. These are mean values, representing a volume of $\mathrm{d}x \times \mathrm{d}y \times \mathrm{d}z = 400 \times 400 \times 240\,\mathrm{km}^3$. Therefore, very high

velocities, which are observed on the Sun, are not resolved in our model. The average absolute velocity is in the order of 10 km/s at all heights.

In order to demonstrate the plasma flow, test particles were traced for a period of one solar hour. Initially, 64^3 particles were distributed uniformly among the grid points at the time t=0s. The positions at the next time step were computed using the plasma velocities. Thereby we assumed that the flow is steady in between the snapshots and we neglected viscous effects. This procedure is repeated for the 120 time steps. After one solar hour the test particles are clustered in loops or in a granulation pattern, as shown in figure 5.3. Each dot represents a test particle, while the color represents its actual vertical velocity. Red dots move downwards and blue dots upwards. Above 5 Mm coronal loops are visible. Below that height convection circulates the plasma. The convection is a result of the small heat conduction coefficient. The focus of this work was to investigate the coronal heating mechanism, for what reason a proper description of coronal physics is necessary. Therefore, we use the Spitzer heat conduction. Due its strong temperature dependency ($T^{5/2}$) it has no effect to chromospheric temperatures. It is not only smaller by factor 100 as in the corona but also anisotropic. The additional isotropic heat conduction, used to stabilize the code, is also to small. Fluctuations in the heat distribution can therefore only be convected away. The dominant red color in the chromosphere indicates a strong down flow of matter. This can also be seen when looking at the net mass flux. The model chromosphere works as a mass reservoir and is therefore not included in the line emission synthesis. The granular pattern in the lower chromosphere is therefore a superposition of the convective motion and a down flow along magnetic fieldlines.

In the top left panel of figure 5.3 the main polarities of the magnetogram (cf. figure 3.3) are visible. Also loops with foot points at the main polarities are outlined. Around the position $x = 40\,\mathrm{Mm}$ and $y = 10\,\mathrm{Mm}$, next to the positive polarity, particles seem to cluster at the outer shell of a flux tube. The two panels in the bottom row of figure 5.3 depict large loops structures. Loop halves seem to contain either down or up flow, but none of them dominates in the coronal part. This result of the quasi-stationary state, in which the corona has no net mass flux in the vertical direction. However, for a detailed and quantitative analysis one needs to synthesize line emissions and Doppler shifts. This will be discussed later in this chapter.

5.1 Momentum balance

The change of the plasma momentum is described by the forces per unit volume on the right hand side of:

$$\rho \frac{D\mathbf{u}}{Dt} = -\nabla p + \mathbf{j} \times \mathbf{b} - \rho \nabla \Phi + 2\nu \nabla \circ (\rho \underline{S})$$

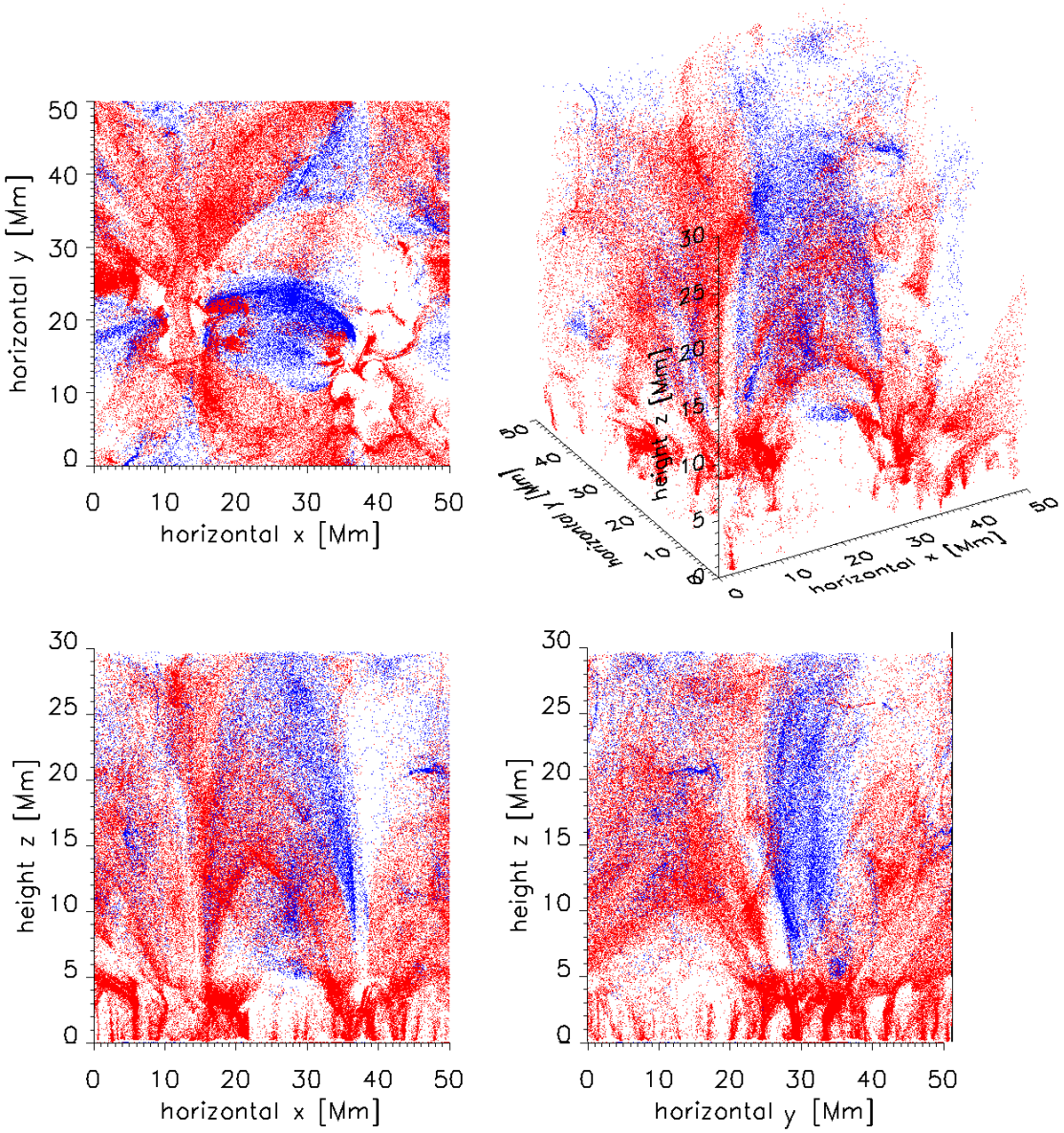

Figure 5.3: Tracer particle positions (dots) after one solar hour. Initially, particles where distributed homogeneously among the grid points and then traced using the plasma velocity. Each panel shows a "line of sight integration". That is, all particles are projected to the image plane. No viscous effects were considered in the tracing routine. From top left to bottom right: Views along the z-direction, a tilted cube, y-direction, x-direction. Blue color indicates particles with upwards velocity and red color those with downward velocities.

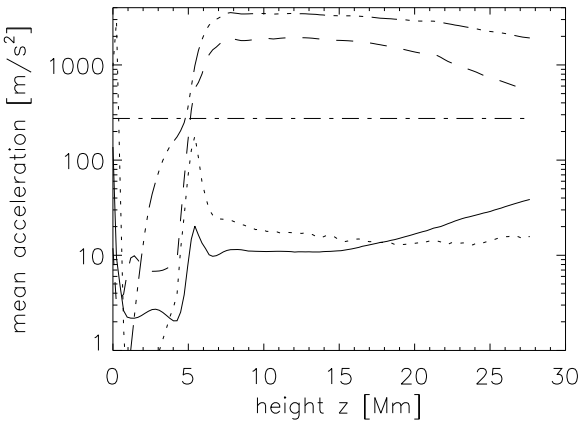

Figure 5.4: Horizontal average of the net acceleration: Lorentz force (triple dotted line), viscous force (dotted line), gravity (dash-dotted line), pressure (dashed line) and advection term (solid line), cf. equation 2.27.

The strength of the forces and therefore their importance for the coronal dynamics is illustrated in figure 5.4. The forces are first divided by the density and then averaged horizontally. Thus, shown are the forces per unit mass or simply the acceleration.

The Coriolis force and the centrifugal force are neglected in our model. We can estimate the order of the centrifugal force using the rotation period of the Sun of approximately 25 days and the solar radius $R = 700\,\mathrm{Mm}$. Our numerical box is located at the disk center. Therefore the centrifugal force reads:

$$f \approx \rho \frac{4\pi^2}{T^2} R = \rho\, 5.9 \cdot 10^{-3} \frac{m}{s^2} \tag{5.1}$$

Thus, in comparison to the net accelerations in figure 5.4 the centrifugal force is neglectable. We can make the same estimations for the Coriolis force and use a typical velocity of $100\,\mathrm{km/\,s}$:

$$f \approx \rho \frac{4\pi}{T} u = \rho\, 0.87 \frac{m}{s^2} \tag{5.2}$$

As well as the centrifugal force the Coriolis force is smaller than the forces in figure 5.4 by several orders of magnitude.

In our model gravity is constant with height. This assumption is reasonable, since the height of the simulation domain is small when compared to the solar radius. The dominating forces in the corona are the Lorentz force and the pressure gradient. The average Lorentz force is dominant except in the photosphere and the lower chromosphere. In the transition region, high velocities are present. Thus, in this regime, the viscous force and the advection increases to a tenth of the Lorentz force but are much smaller elsewhere. This is illustrated in figure 5.5 which shows that the plasma is dominated by the magnetic field and the gas pressure. Plasma beta

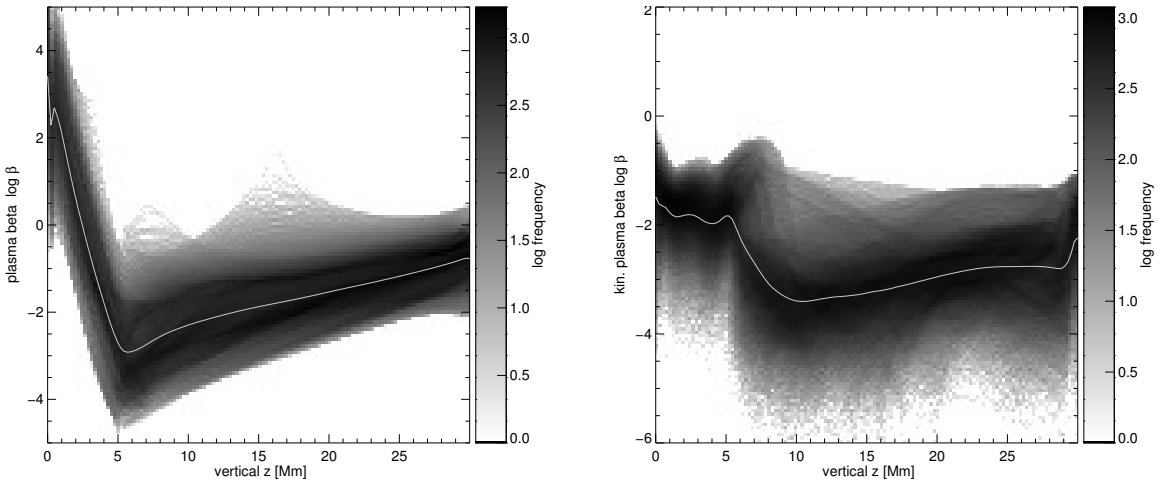

Figure 5.5: *Left*: Plasma beta represents the ratio of gas pressure to magnetic pressure. *Right*: Kinetic plasma beta, which is a measure of the fraction of kinetic energy to magnetic energy. Both panels show a two dimensional histogram in greyscale. Over plotted by the mean value of kinetic plasma beta and plasma beta (solid line).

(left panel) shows a behavior comparable to observations (cf. Gary (2001)). In the photosphere the plasma density is high and therefore the gas pressure is dominant. With height the density drops by several orders of magnitude, and thus decreases faster than the magnetic energy density. Therefore, the plasma beta is small in the transition region and lower corona. Higher up in the corona, the density stays almost constant and the magnetic energy density decreases further. As a result plasma beta increases again. Gary (2001) reports a plasma beta equal to unity at a height of $\approx 100\,\mathrm{Mm}$. This is far outside of our domain but simple linear extrapolation would lead to a height of $\approx 40\,\mathrm{Mm}$ in our model. This may be an artifact of the upper boundary condition and needs to be investigated in future simulations.

The kinetic plasma beta is the ratio of kinetic energy to magnetic energy and is illustrated in the right panel of figure 5.5. It is smaller than the plasma beta when comparing the horizontally averaged values (solid line). Due to the large variation of both quantities, an overlap exists, and therefore the kinetic plasma beta may be bigger than plasma beta at a minority of grid points.

5.2 Energy balance

To understand the reason for the coronal temperature we investigate the term on the right hand side of the energy equation:

$$\begin{aligned} c_V \rho T \frac{D \ln T}{Dt} = & - c_V \rho T (\gamma - 1) \nabla \cdot \mathbf{u} - \left(\frac{0.8\rho}{m_p}\right)^2 Q(T) + \frac{1}{\tau}(T_0 - T) \\ & + \nabla \cdot \left(K_0 T^{\frac{5}{2}} \mathbf{b}(\mathbf{b} \cdot \nabla T) \right) + \nabla \cdot (c_p \chi \rho \nabla T) + \nabla \cdot (c |\nabla T| \nabla T) \\ & + \eta \mu_0 \mathbf{j}^2 + 2\rho\nu \mathbf{S^2} + \zeta \rho (\nabla \cdot \mathbf{u})^\mathbf{2} \end{aligned}$$

Again we divide by the density and compute the horizontal averages. The temperature change per unit time, which is proportional to the heat change per unit time per unit mass, is shown in figure 5.6. Depicted are the heat conduction terms on the left hand side and the energy losses and gains on the right hand side. The most important process in the corona is the Spitzer heat conduction. Due to its strong temperature dependence it is highly inefficient in the chromosphere. Therefore we included isotropic heat conduction (dotted line), which does neither depend on temperature nor density but only on their gradients. This isotropic heat conduction dominates in the chromosphere but is small when compared to the other heat conduction processes outside the chromosphere. The third heat conduction term, in which the heat flux vector is proportional to the temperature gradient, works only in the transition region. Its purpose is to stabilize the simulation by reducing strong temperature gradients.

The right panel of figure 5.6 illustrates the volumetric heating and cooling functions. In the corona, the Ohmic heating rate is larger than the rate of radiative loss. This implies that, in order to keep the coronal temperature constant, the remaining energy has to be conducted away. Viscous heating is a major contribution and even exceeds the radiative loss at heights above $z \approx 20\,\mathrm{Mm}$. Spitzer (1962) gives a kinematic viscosity for a fully ionized gas

$$\nu \approx 2 \cdot 10^{-17} \frac{(T/[\mathrm{K}])^{\frac{5}{2}}}{\rho/[\frac{\mathrm{kg}}{\mathrm{m}^3}]} \frac{\mathrm{m}^2}{\mathrm{s}} \,. \tag{5.3}$$

The derivation of the viscosity assumes also small temperature gradients and average coronal density. Under these assumptions, we can compute a kinematic viscosity in the solar corona to $\nu \approx 10^{11} \frac{\mathrm{m}^2}{\mathrm{s}}$. The kinematic viscosity used in the numerical simulation is in the same order as the value derived by Spitzer (1962). Thus, the viscous heating is not overestimated in the numerical model. The Newton cooling term has only influences on the photosphere, as it decreases rapidly towards the chromosphere. In our model it has no effect above $z = 3\,\mathrm{Mm}$.

The average coronal temperature profile is a result of the Ohmic heating and cooling by Spitzer heat conduction. The temperature gradient in the transition region is

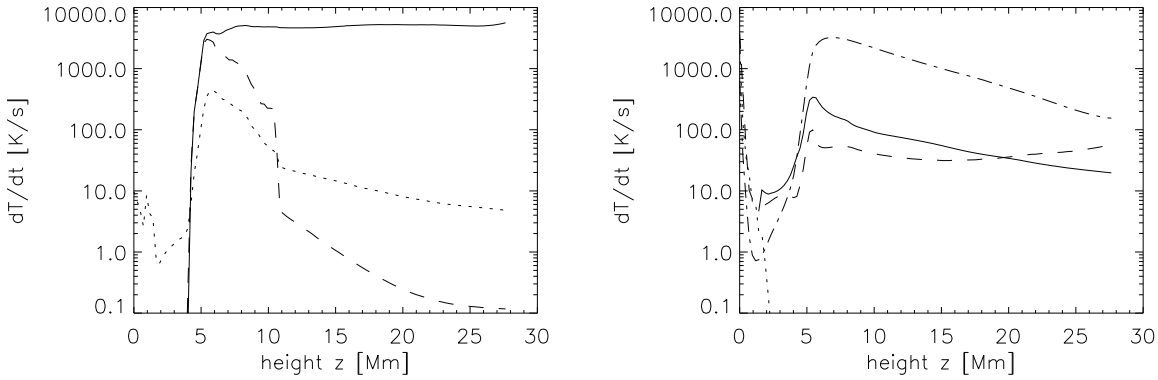

Figure 5.6: Horizontally averaged absolute temperature change per second. *Left*: Spitzer heat flux (solid line), isotropic $K \sim \nabla T$ (dashed line) and isotropic constant χ (dotted line). *Right*: Radiative loss (solid line), Newton cooling (dotted line), viscous heat (dashed line) and Ohmic heat (dash-dotted line).

determined by the Spitzer heat conduction, the additional isotropic heat conduction and the radiative losses. Finally, the Newton cooling defines and only affects the lower chromosphere and the photosphere.

5.3 Spectral synthesis and differential emission measure

To proceed with the forward model approach, we have to calculate the emissivity at each grid point in order to compute the emission line profiles along a line of sight. These profiles can be directly compared to observed spectra. Additionally, they may be analyzed using the conventional techniques like Differential Emission Measure (DEM) or Doppler shift analysis. The results, which are presented in this section, show that our model yields comparable observable quantities as observations.

The line emissivities at each grid point are calculated under the assumption of ionization equilibrium. The lines are dominantly excited by electron collision and de-excited by spontaneous emission. The emissivity is therefore given by:

$$\epsilon = h\nu n_2 A_{21} := G(T, n_e) n_e^2 \tag{5.4}$$

with the electron density n_e and a function $\mathrm{G(T}, n_e)$ defined as

$$G(T, n_e) = h\nu A_{21} \cdot \frac{n_2}{n_e n_{\mathrm{ion}}} \cdot \frac{n_{\mathrm{ion}}}{n_{\mathrm{el}}} \cdot \frac{n_{\mathrm{el}}}{n_{\mathrm{H}}} \cdot \frac{n_{\mathrm{H}}}{n_e} \tag{5.5}$$

The terms on the right hand side of equation (5.5) describe the excitation of the atom, the ionization of the respective ion, the elemental abundances and the degree of ionization of the plasma. The first term is a constant given by atomic physics. The

population of the upper level n_2 is proportional to the density because we assume excitation by electron collision. For the element abundances we use constant values throughout the box according to photospheric values tabulated in CHIANTI (Landi et al., 2006). Also the ionization degree $\frac{n_{\mathrm{ion}}}{n_{\mathrm{el}}}$ and depending thereof the value for $\frac{n_{\mathrm{H}}}{n_e}$ are determined using CHIANTI. From this discussion we see that the contribution function $G(T, n_e)$ as defined in equation 5.4 depends only weakly on density when selecting an appropriate line. Mainly because of the ionization equilibrium the function $G(T, n_e)$ strongly peaks in temperature. For density insensitive lines, i.e. $G{=}G(T)$, the emissivity reflects that the optically thin radiative losses are proportional to the density squared. To evaluate the emissivity at each grid point of the MHD calculation we finally compute the electron density n_e from the mass density ρ of the MHD calculation using the degree of ionization, again as obtained from CHIANTI. If we use an integration along the line of sight we are able to calculate the energy flux density out of our computational box, e.g. in units of $\mathrm{W/m^2}$ for a given line. These quantities can be converted easily into line irradiances as they would be observed e.g. at a certain distance from the Sun.

The intensity at a distance d from the emitting volume V is

$$\begin{aligned} I &= \frac{1}{\pi d^2}\int_V G\left(T\right) n_e^2 \mathrm{d}V \\ &= \frac{1}{\pi d^2}\int_T G\left(T\right) n_e^2 \frac{\mathrm{d}V}{\mathrm{d}T}\mathrm{d}T \\ &= \frac{A}{\pi d^2}\int_T G\left(T\right) n_e^2 \frac{\mathrm{d}h}{\mathrm{d}T}\mathrm{d}T \\ &= \frac{A}{\pi d^2}\int_T G\left(T\right) \mathrm{DEM}\left(T\right) \mathrm{d}T \end{aligned}$$

where DEM is the differential emission measure and A is the observed area. The differential emission measure

$$\mathrm{DEM}\left(T\right) = n_e^2 \frac{\mathrm{d}h}{\mathrm{d}T}$$

characterizes the amount of matter in a certain temperature interval $\mathrm{d}T$. It is a inverse problem and can be solved with a variety of methods. The diagnostics are already in use for several years. The spectral analysis, shown in this section, meaning the emission measures, Doppler shifts and emissivities, is done by Zacharias (PhD thesis, to be finished December 2009). In figure 5.7 we compare the results from our model to the model of Gudiksen and Nordlund (2005) and additionally to observations. The left panel depicts the direct computation of the differential emission measure using $n_e^2 \left(\frac{\mathrm{d}T}{\mathrm{d}h}\right)^{-1}$. This profile shows the same behavior as the observed profiles. It contains a minimum around $\log(T/[\,\mathrm{K}]) = 5.4$, and a maximum at $\log(T/[\,\mathrm{K}]) = 6.0$. Furthermore, Zacharias investigates the DEM based on the line

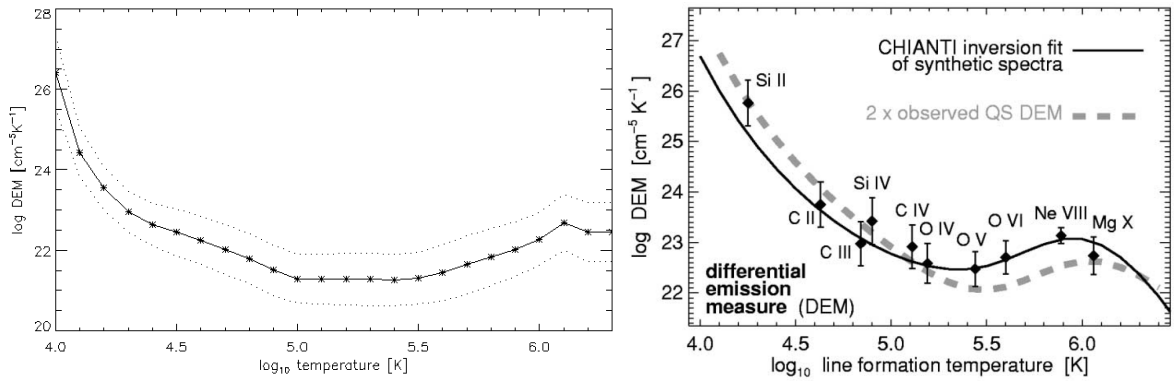

Figure 5.7: *Left*: Differential emission measure (DEM) vs. temperature as computed from simulation data (Zacharias, PhD thesis). The horizontal average is marked by the stars and the dotted lines show the one sigma deviation. *Right*: Observed quiet Sun DEM (dashed line) and synthetic spectra derived from model by Gudiksen and Nordlund (2002) (panel taken from Peter et al. (2004)).

emissivities and the inversion of the problem. Additionally, she computed the emissivities at all grid points for a set of emission lines. We can now observe our model from all sides by integrating the emission along a line of sight. Since the plasma is optically thin, the integration can be replaced by the sum over the grid points along the path. Figure 5.8 and 5.10 show two examples of the synthesized line emissions, where we look from three sides towards the model. The first panels show the view along the y-direction, the middle panel along the x-direction and the last panel shows the domain as seen from above. The first two panels correspond to observations at the solar limb, whereas the right panel corresponds to disk center. The emission of O V originates (cf. figure 5.8) (630 nm) mainly from the transition region, where the line formation temperature of O V ($T \approx 240\,000$ K) is reached. The left and the middle panel show loop like structures of different lengths. In the right panel, the main polarities of the underlying magnetogram are recognizable. Additionally, a Moiré effect interferes with the emission structure. This effects occurs as a result of the barely resolved temperature range in the line formation region. The temperatures in the model rises within a few grid points from some thousand to one million degrees Kelvin. The figure 5.10 shows the emission of Ne VIII, which forms in the lower corona. Besides the loop structures in the left and middle panel, a more diffuse corona stretches towards the upper boundary. Diffuse coronae are observed during the solar minimum and are therefore an indication for a lower magnetic activity. The corona in our model is a result of a scaled down Active Region. Hence, the magnetic structures do not dominate the upper corona and the emission is more diffuse. In the right panel, the main magnetic polarities are distinguishable. Here the Moiré effect is not present, as the temperature stratification of line formation temperature of Ne VIII is better resolved.

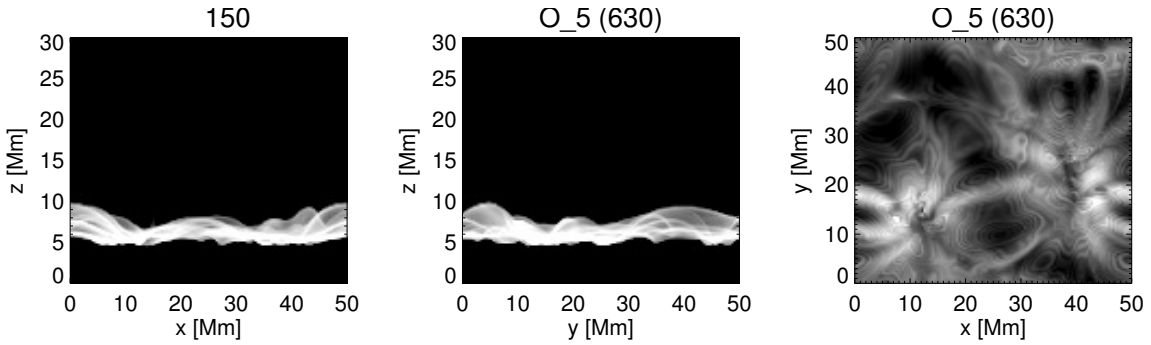

Figure 5.8: Integrated emission of O V (630 nm) along line of sight (Zacharias, PhD thesis). The line formation temperature is $\log(T/[\mathrm{K}]) = 5.38$. *Left*: Side view from y-direction. *Middle*: Side view from x-direction. *Right*: The model as seen from above (z-direction).

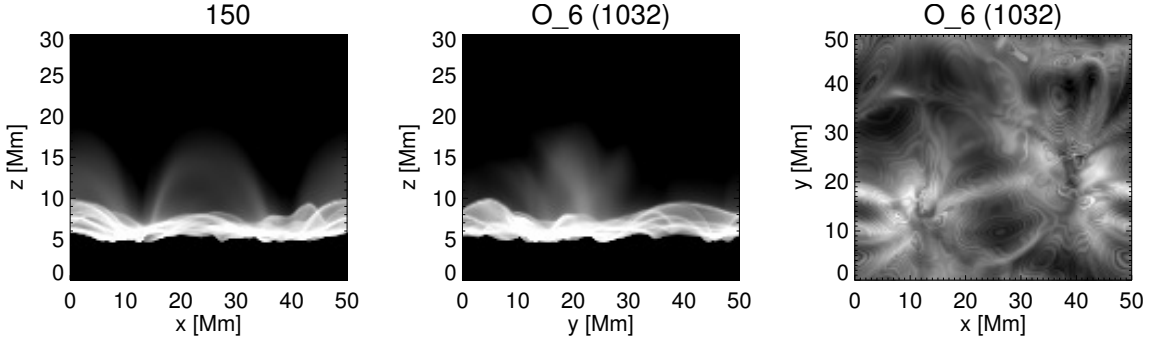

Figure 5.9: Integrated emission of O VI (1032 nm) along line of sight (Zacharias, PhD thesis). The line formation temperature is $\log(T/[\mathrm{K}]) = 5.45$. *Left*: Side view from y-direction. *Middle*: Side view from x-direction. *Right*: The model as seen from above (z-direction).

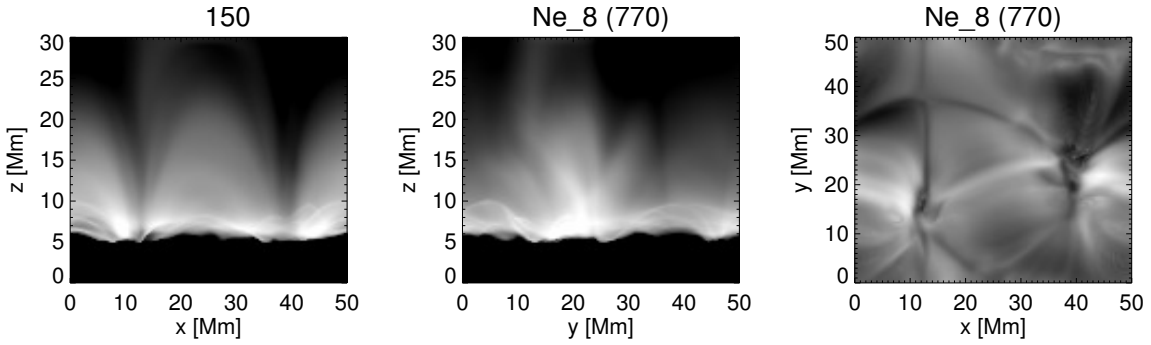

Figure 5.10: Integrated emission of Ne VIII along line of sight (Zacharias, PhD thesis). The line formation temperature is $\log(T/[\mathrm{K}]) = 5.8$. *Left*: Side view from y-direction. *Middle*: Side view from x-direction. *Right*: The model as seen from above (z-direction).

6 Heating of the corona

The heating mechanism of the solar corona is still under debate. Although there are different scenarios suggested, we focus in this model on the heating by Joule dissipation. The heating rate is given by $\eta\mu_0\mathbf{j}^2$, in which the resistivity η is constant in time and space. Under this assumption, the plasma is heated where the currents occur. In the following we discuss the efficiency and occurrence of Ohmic heating and discuss possible consequences of the MHD approximation.

6.1 Heating in the numerical model

The horizontally averaged heating shows an exponential decay with height in the coronal part of our model and increases strongly towards the photosphere, cf. figure 6.1. This mean profile varies in time only by a few percent. Likewise, the time dependence of the minimum and maximum values at each height (dashed lines) do not vary significantly with time. The temporal evolution will be discussed in detail later. Then we will also investigate the change of the heat input at a fixed point in space.

To find the scale height of the heating function, a linear function is fitted to the logarithmic horizontally averaged heating function for all 120 time steps covering one solar hour. During that time, the scale height changes smoothly between $h_{\min} = 7.4\,\mathrm{Mm}$ and $h_{\max} = 10.3\,\mathrm{Mm}$, but does not show a particular pattern. Only the range from $z_1 = 4.7\,\mathrm{Mm}$ to $z_2 = 28.3\,\mathrm{Mm}$ is used. We get $\overline{h} = (8.73 \pm 0.85)$ Mm as the temporal mean scale height for our model. The errors are the standard deviations. This result corresponds nicely to the scale height of 5 Mm found in the simulation of Gudiksen and Nordlund (2005). It is also comparable to the scale heights used for models of 1D-loops including radiative transfer or other simulations which do not solve the complete set of equations and thus have to assume properties of the heating process. For example, Müller et al. (2004) examined in his thesis the behavior of 1D loops when they are heated with different processes and strengths. He found that loops are stable when the heating scale height is higher than 6 Mm. In this sense the loops in our model are stable.

In the right panel of figure 6.1 an energy flux is derived from the heat input. Starting at the photosphere and going upwards, the flux at a given height is equal to the total energy input in the volume above divided by the horizontal plane. It is

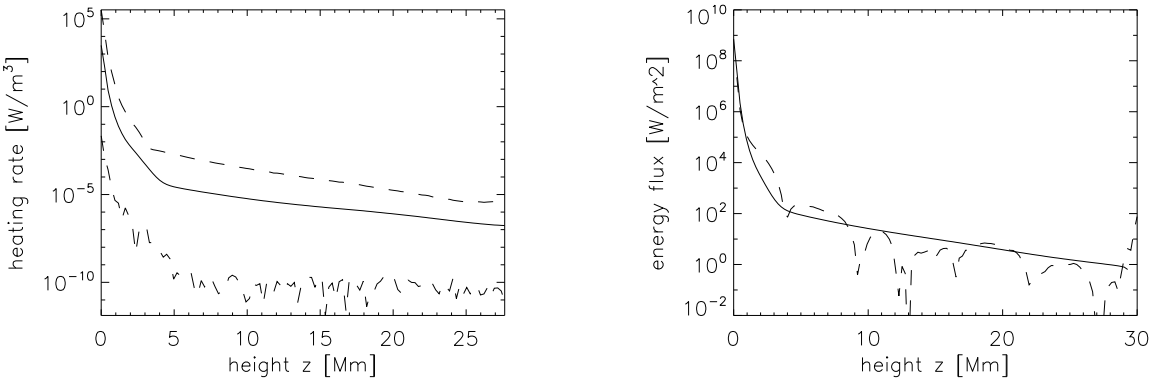

Figure 6.1: *Left*: Horizontally averaged heat input at each height (solid line). Minimum and maximum heat input at each height (dashed line). *Right*: Heat flux (solid line) to sustain average heat input and horizontally averaged vertical Poynting flux (dashed line).

the same as to integrate the average heating rate $h(z)$. The conservation law in one dimension is

$$\frac{\mathrm{d}h(z)}{\mathrm{d}t} + \frac{\mathrm{d}f_h}{\mathrm{d}z} = 0 \tag{6.1}$$

where f_h is the heat flux in the vertical direction. We can compute the heat flux at a coordinate z_0 by integrating the equation 6.1:

$$\int_{z_0}^{\infty} \frac{\mathrm{d}h}{\mathrm{d}t}\mathrm{d}z + (f_h(\infty) - f_h(z_0)) = 0\ . \tag{6.2}$$

We now assume that the heat flux vanishes towards infinity. Then the flux at a height z_0 is given by

$$f_h(z_0) = \int_{z_0}^{\infty} \frac{\mathrm{d}h}{\mathrm{d}t}\mathrm{d}z \tag{6.3}$$

This can be evaluated by numerical integration. The error we make by integrating only up to the upper boundary is small because the heating rate decreases exponentially with height. Tests with extrapolated heating rates show no significant difference.

The energy flux at the base of the corona ($z \approx 5\,\mathrm{Mm}$) is in the order of 100 $\mathrm{W/m^2}$. This is sufficient to maintain a one million degrees hot corona. Observations and theory arrogate a heat flux in this dimension, otherwise the energy loss by radiation and conduction could not be balanced. The required heat flux changes slightly for Active Regions, the quiet Sun or Sun spots. Additionally, the energy amount to sustain chromospheric temperatures also matches the theoretical requirements of $\approx 10^4\,\mathrm{W/m^2}$.

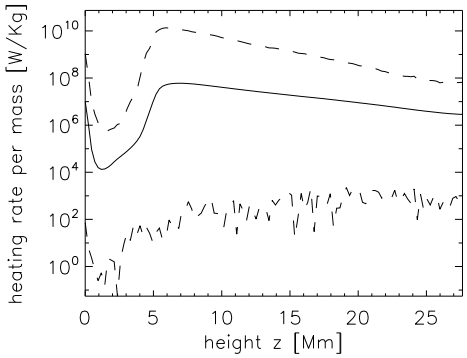

Figure 6.2: Horizontally averaged heating per unit mass (solid line), minimum and maximum values (dashed line) at each height.

The dashed line in the right panel of figure 6.1 shows the absolute vertical Poynting flux. As expected, it is in the same order. It illustrates the flow of energy in a quasi-stationary state corona as shown in figure 3.2.

It is useful to calculate the heat input per unit mass, to see where the heating of the atmosphere is enhanced. It is directly proportional to the temperature increase per unit time. The strongest heating occurs at $z = 6\,\mathrm{Mm}$, cf. figure 6.2. In the corona, the heating rate per unit volume has a scale height of 8.73 Mm and the density is almost constant. Therefore the scale height for the heating rate per unit mass is $h \approx 6.5\,\mathrm{Mm}$. In the chromosphere, the heating is less effective due to the strong increase in density towards the photosphere, therefore the curve decreases towards lower heights.

Poynting flux

Due to the highly structured magnetic field and the fact that the velocities change directions frequently, the averaged Poynting flux is also highly structured. Hence, for a single timestep, the Poynting flux is not directed upwards everywhere. Left panel in figure 6.3 illustrates the horizontally and temporally averaged composition of the Poynting flux (cf. equation 2.15) in the vertical direction. The first term $\mathbf{j} \times \mathbf{B}$ is on average positive up to $z = 11\,\mathrm{Mm}$ and negative above. The term $\mathbf{B} \times (\mathbf{u} \times \mathbf{B})$ is only positive up to $z = 4\,\mathrm{Mm}$ and downwards directed above. Since plasma beta increases towards the upper boundary, the plasma drives the magnetic field and thus injects electromagnetic energy. This energy is transported downwards to the place where the magnetic field dominates. Additionally, the Poynting flux channels energy in the direction of the velocity and perpendicular to the magnetic fieldlines. Since the magnetic fieldlines close in the upper domain, the direction of "open field" in which the energy flows is downwards.

However, the energy input is proportional to the divergence of the Poynting vector. The right panel in figure 6.3 depicts the horizontally averaged energy input for one

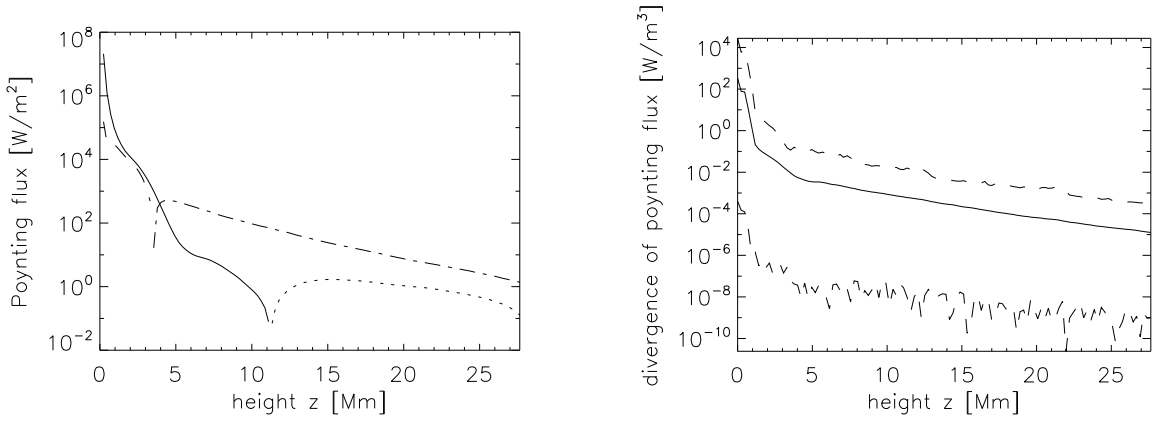

Figure 6.3: *Left*: Composition of the vertical Poynting flux. Upwards (solid line) and downwards (dotted line) directed flux due to $\mathbf{j} \times \mathbf{B}$ term. Upwards (dashed line) and downwards (dashed-dotted line) directed flux due to $\mathbf{u} \times \mathbf{B} \times \mathbf{B}$ term. Profiles are averaged over 1h time. *Right*: Divergence of the Poynting flux horizontally averaged (solid line) and the minimum and maximum values at each height (dashed lines).

snapshot. Also shown are the horizontal minimum and maximum values. The energy input derived from the divergence of the Poynting flux matches the Ohmic heating in figure 6.1. This illustrates that on average the magnetic energy change per unit time is approximately zero: $\partial e_{em}/\partial t = 0$. It shows also that the model is in a quasi-stationary state.

6.1.1 Resistivity and Reynolds number

The Ohmic heating is, besides the heat conduction, the major process in the solar corona. As the heating depends on the magnetic diffusivity, cf. equation (2.37), it needs to be discussed in more detail. Galsgaard and Nordlund (1996) investigate the magnetic energy dissipation for different numerical resolutions in a simplified 3D MHD model. The energy dissipation in their model scales with the Poynting flux for different numerical resolutions. Higher numerical resolutions also implies smaller length scales. So the amount of dissipated energy does not depend on the spatial resolution.

Assuming the Poynting flux at lower boundary is constant with time, the dissipated magnetic energy in the box should not depend on the magnetic diffusivity (resistivity), as long as the dissipative time scale is shorter than the time scale of the dynamical driver. The time scale of the foot point motions is in the order of minutes. As shown later in this section, the diffusive time scale is in the order of seconds.

Another effect is the size of current sheets. For smaller η the current sheets become thinner. But current sheets below the spatial resolution of the numerical model are

not resolved. Thus it is only meaningful to increase the resistivity up to a certain threshold.

We can compare η with solar values: Spitzer (1962) derives the magnetic diffusivity for a fully ionized gas as

$$\eta \approx 5 \cdot 10^8 \, (T/[\,\mathrm{K}])^{-\frac{3}{2}} \; . \tag{6.4}$$

Together with a typical velocity of $u = 100\,\mathrm{km/\,s}$ and a typical length scale of $l = 100\,\mathrm{km}$, the corona exhibits a magnetic Reynolds number of $\mathrm{Rm} = 10^{10}$. This number can also be read as a timescale comparison.

$$\mathrm{Rm} = \frac{\tau_{diff}}{\tau_{advec}}$$

For large Reynolds numbers the advective time scale is much shorter than the diffusive time scale. This implies that the magnetic field is forced to move with the plasma. With the same numbers as used for the Reynolds number we can compute the timescale to

$$\tau_{advec} \;\; = \;\; \frac{l}{u} = 1\,\mathrm{s} \tag{6.5}$$

The diffusive timescale then is $\tau_{diff} = 10^{10}\,\mathrm{s}$ or several thousand years. But we know from observations that processes related to the magnetic field have shorter periods. For example, a typical Active Regions decays within a day. And if Ohmic dissipation heats the corona, it has to be at least as fast as the radiative loss timescale. The idea is that the typical length scale decreases when magnetic fieldlines are braided. The decline stops when the magnetic Reynolds number is in the order of unity. In this case diffusion inhibits a further twist of fieldlines.

Galsgaard and Nordlund (1996) already showed that the length scales of the magnetic field decrease when plasma motions shears the field. The length scales in their model show strong spatial variation and the Poynting flux into the domain is also proportional to the energy loss.

If we would apply such a high solar magnetic Reynolds number in our model, there would be no dissipation of magnetic energy at all. The length scale in our simulation, that enters the magnetic Reynolds number, is limited to the spatial resolution. The grid spacing is the smallest length scale per definition. Therefore, the magnetic diffusivity has to be increased to reach a magnetic Reynolds number in the order of unity.

We set the resistivity η to be constant in time and space for numerical purposes. Hence, additional derivatives are avoided which may lead to instability. In future works we will investigate the influence of a temperature dependent magnetic diffusivity.

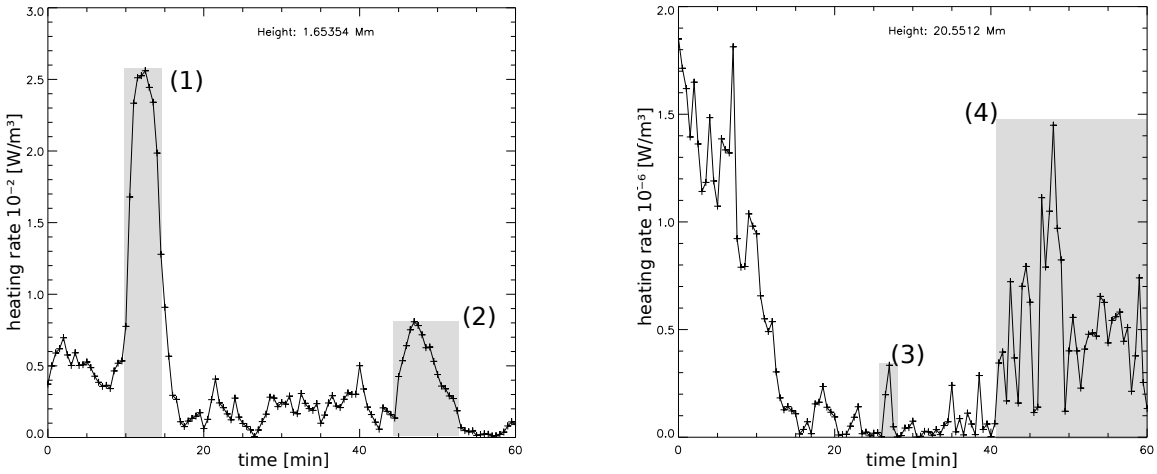

Figure 6.4: Temporal evolution of Ohmic heating at two specific grid points. Left panel at $z \approx 1.6\,\mathrm{Mm}$ and right panel $z \approx 20.5\,\mathrm{Mm}$. Crosses mark the time steps. Several heating events with different amplitudes and durations can be seen. The numbers (1)-(4) indicates events that are discussed in the text.

6.2 Nanoflare heating

Even if the average heat profile is nearly constant in time, the evolution of the heating at a fixed point in space is highly dynamic. Two examples out of 128^3 are shown in figure 6.4. We selected one coordinate in the chromosphere and the other one in the upper corona. The order of magnitude differs by a factor of 10^4 but both profiles show sequences of events. Each individual event is resolved in time, but they differ in duration and amplitude. The cadence shown in the figure is much longer than the typical time step of $10^{-3}\,\mathrm{s}$, i.e. the heating events are even better resolved in the simulation run. We can compute the released energy during an event and categorize the events into flares or nanoflares. For the events we assume a size of one up to a few grid points. Before we compute single events in the next section, average and statistical information is derived first.

The temporal progress in figure 6.4 suggests a periodicity in the event statistics. Therefore, we compute the power spectrum for each grid point to find distinguished frequencies. For each spectrum 120 time steps with a cadence of 30 seconds are used. In the left panel of figure 6.5 the power spectrum for an arbitrary grid point is shown. No dominant frequency is visible but an increase in power towards small frequencies. To reduce the noise we averaged all 128^3 power spectra. To account for the different amplitudes, the profiles are normalized before averaging. The result is shown in the right panel of figure 6.5. The average power spectrum is fitted with a $\frac{1}{f^2}$ function. Figure 6.5 illustrates that the heating events are randomly distributed. It is called red noise because the power increases for low frequencies.

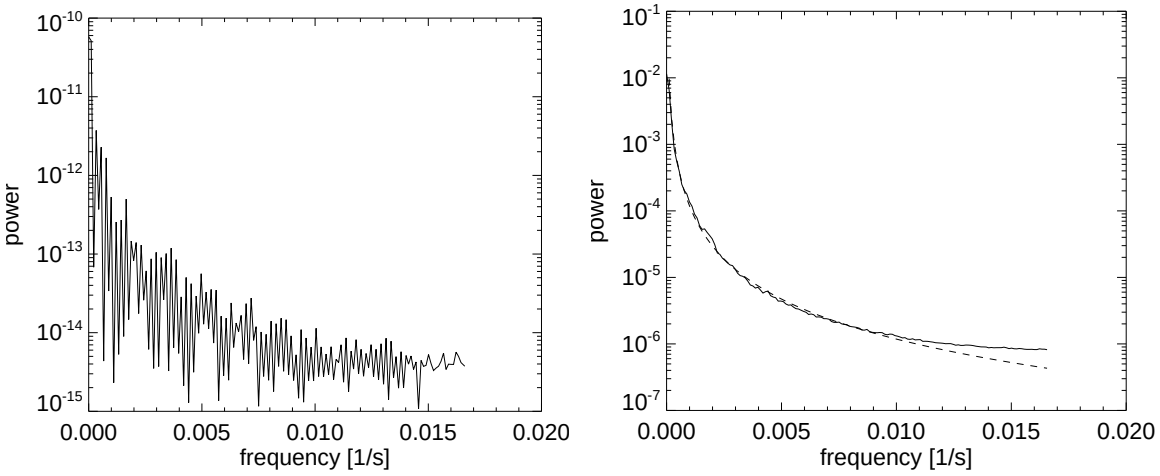

Figure 6.5: *Left*: Power spectrum for the same grid point as in the right panel of figure 6.4. *Right*: Power spectrum (solid line) averaged over all grid points and fitted with a $\frac{1}{f^2}$ function (dashed line).

6.2.1 Individual events and storms

Warren et al. (2003) reproduced the light curve of a loop, observed with TRACE, with a numerical loop model. Instead of one single flare event, different threads of the loop are heated sequentially, in this work. That means that the heat input is spread spatially and temporally. Klimchuk (talk at Hinode 2 Meeting) called that scenario nanoflare storms, where the periods and the intensities of such storms may vary. Nanoflare storms are difficult to observe since single events in a storm have overlapping light curves. Therefore the scenario of Nanoflares is postulated to reproduce light curves which looks like a flare event. Thus, no observational evidence for Nanoflare storms exists yet. While we investigated averaged profiles in the first part of this chapter, single events are examined in the following. We use the events in figure 6.4, labeled (1) to (4) and listed in table 6.1. A typical observed Nanoflare on the Sun has an energy of $10^{17}\,\mathrm{J} - 10^{19}\,\mathrm{J}$, cf. Aschwanden (2006). Hence, event (1) and (2) can be categorized as Nanoflares. Event (3) is very small in duration and amplitude and is not observable. The combination of events however, the storm (4), has an energy which is more than ten times higher. In comparison to the events (1) and (2) the storm occurs higher in the atmosphere. Hence, less plasma has to be heated. Additionally, the storm in figure 6.7 ($x = 41 - 46\,\mathrm{Mm}$, $t = 20 - 40\mathrm{min}$) spans over a bigger area than assumed in the calculations. If the spatial extent of the Storm (4) is in the same size as the storm in 6.7, the total energy of such a Nanoflare storm would be $10^{17}\,\mathrm{J}$, equal to the amount of one regular Nanoflare. Thus, we group events with small energies to build a Nanoflare. This is the first time that those Nanoflare storms are found in a self consistent numerical simulation. The events are properties of the numerical model.

N^o	duration	energy
(1)	300 s	$7.5 \cdot 10^{18}$ J
(2)	540 s	$3.8 \cdot 10^{18}$ J
(3)	180 s	$5.4 \cdot 10^{13}$ J
(4)	1749 s	$8.7 \cdot 10^{14}$ J

Table 6.1: Properties of heating events shown in figure 6.4. For each event a volume of 3x3x3 grid points $\approx 1\,\mathrm{Mm}^3$ is used.

The magnetic configuration in our model is not meant for producing a flare. It represents a stable Active Region shuffled around by the photospheric motions. Therefore, we are not able to find a storm of large events. But showing the existence of small Nanoflare storms suggests, that models with higher magnetic activity, for example using an unscaled magnetogram, may find stronger Nanoflare storms.

6.2.2 Distribution of events

Parker (1988) already proposed that the heating mechanism of the corona is an effect of many small flares. These small flares have energies much less than a typical solar flare with 10^{24}J. Hence these events have to occur quiet frequently to produce enough energy to heat the corona. Energy is produced by Nanoflares and lost through radiation and conduction. Assuming an equilibrium one can estimate the total energy needed to heat the corona with this mechanism. The total energy is then equal to the integral over the nanoflare frequency distribution $N(\mathrm{E})$. As a start, the shape of this distribution is unrestricted.

Observations yield two dimensional maps with the locations and energies of flare events for different times. These maps can be used to derive a frequency distribution of events per unit area ($1/\,\mathrm{J\,m^2\,s}$). On the Sun, small events are more frequent than large events. Thus, the frequency distribution is similar to the one of figure 6.6. The integral over this distribution determines if there is enough energy produced to heat the corona. The distribution decreases exponentially. Therefore a linear fit at the logarithmic values can be performed.

Observations yield values for the slope of $\alpha = 1.54 \pm 0.03$ for the quiet Sun and $\alpha = 1.55 \pm 0.05$ for Active Regions. Not only the slope, but rather the covered energy range is of importance for the total energy production. For the observations the energy range is limited, so up to now it remains unclear if the energy produced by flares is enough.

Theoretical models can also be used to define a required slope. Using the RTV model (Rosner et al., 1978), where the heating is assumed to be uniform, the frequency distribution has a slope of $\alpha = 1.21 \pm 0.08$ (Aschwanden, 2006).

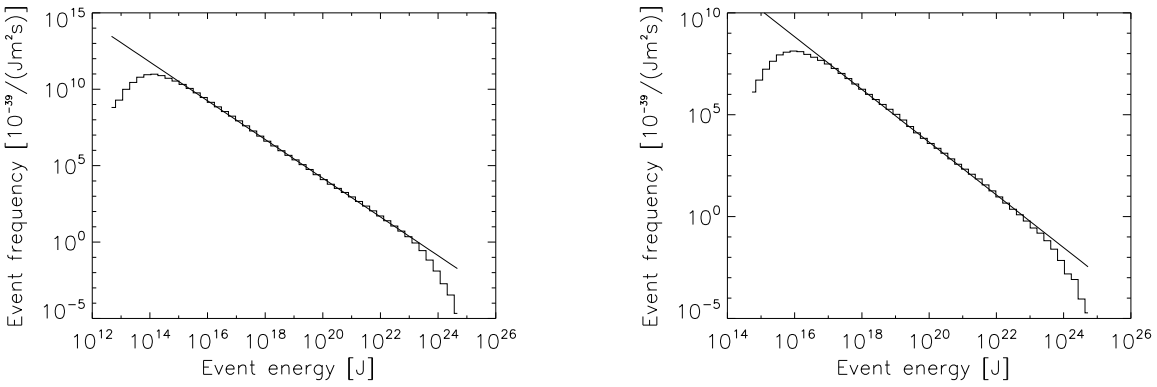

Figure 6.6: Flare frequency for one solar hour and $50 \times 50\,\mathrm{Mm}^2$ area. Each event has a duration of 5 min. *Left*: 8 grid points ($= 0.28\ \mathrm{Mm}^3$) are combined and a linear fit is performed with $N(\mathrm{E}) = (-1.27 \pm 0.003)\mathrm{E} + (9.52 \pm 0.07)$. *Right*: 64 grid points ($= 2.3\ \mathrm{Mm}^3$) are combined. Fit gives $N(\mathrm{E}) = (-1.30 \pm 0.006)\mathrm{E} + (9.6 \pm 0.12)$.

Up to date analysis of observations do not fulfill the requirements and give either too little energy per event or the events are to little frequent. Since we are able to directly compute the energy instead of inverting observations, a flare frequency distribution can be derived directly from our model. Computations of the frequency distribution of the heating events are shown in figure 6.6. We use the $50 \times 50\,\mathrm{Mm}^2$ area of our simulation domain as seen from above. All events are used, even those that are not yet observable. The typical flare duration is assumed to be 5 min for the analysis. A Fourier analysis shows no characteristic spatial scale of the heating events. Two examples are shown: In the left panel we combine 2^3 grid points to one flare, in the right panel 4^3 grid points respectively. Therefore, there are 64^3 or 32^3 events in total. The change in event size alters the energy range but seemingly not the slope of the frequency distribution (left $\alpha = -1.27$, right $\alpha = -1.3$). To combine more grid points to an even bigger volume is not justified when looking at figure 6.7.

6.3 Non MHD effects

When we discuss the heating mechanism in our model, we should remind ourselves of the assumptions we used. The following sections will briefly discuss possible changes to the heating mechanism when we consider effects that go beyond the scope of a pure magneto-hydrodynamical model.

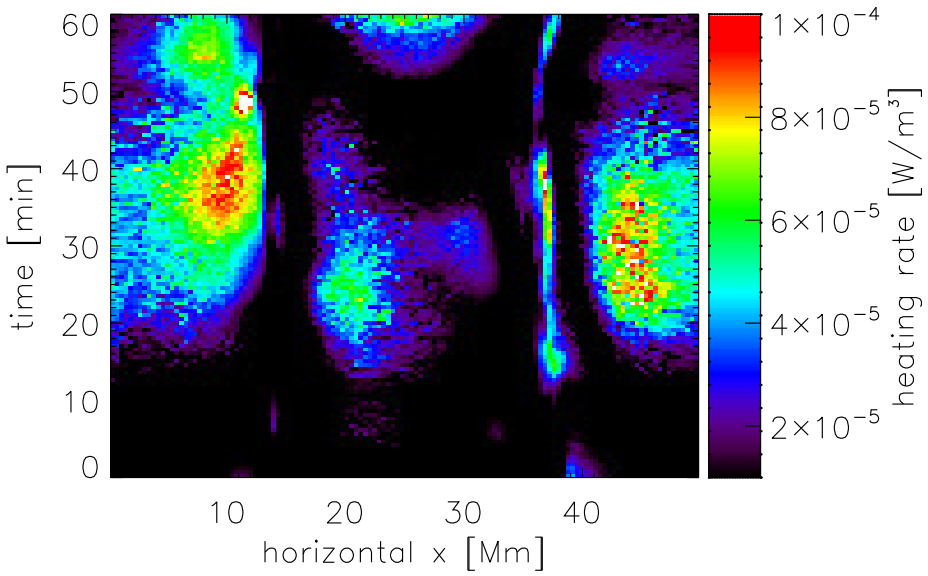

Figure 6.7: Time dependent heating rate along a horizontal line at $z \approx 10\,\mathrm{Mm}$. The line cuts through the loop connecting the main polarities. Color code indicates the strength of the heating. Heating events down to the spatial scale of a grid point are visible.

6.3.1 (Nano)-Flares and electron beams

Do electrons carry energy away? In particular, are electrons heated by a flare still thermal or are they faster and release their energy somewhere else? In our model, where the field is mostly closed, the fast electrons would travel downwards along the fieldlines and release their energy in the chromosphere. They reach the lower atmosphere without losing much of their energy due to their long mean free path (cf. figure 3.7). Electrons traveling upwards would then heat the opposite foot point of a loop. This would result in cooler loops whereas the energy contribution to the chromosphere would be negligible in comparison to the total amount of energy. The thermal energy in the chromosphere is 100 to 10^6 times higher than in the corona. The average coronal thermal energy is $10^{-2}\,\mathrm{J/\,m^3}$.

In our model the electrons are assumed to be thermal since the question how much energy is carried away by these electrons is still under debate. Assuming that all flare energy goes into the acceleration of the electrons, they would reach velocities up to eight times the thermal speed (cf. figure 6.8). This was computed classically, although the thermal speed is already more than one percent of the speed of light. A relativistic calculation would result in smaller numbers. It is unclear however how many electrons are accelerated and thus, how the flare energy is distributed.

This estimate shows that the error introduced by neglecting this effect is in the order of, or less than, the uncertainty of the Spitzer heat flux description. The assumptions made to derive the Spitzer heat flux are gentle temperature gradients,

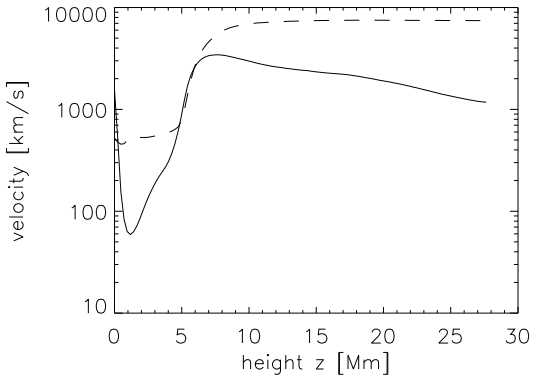

Figure 6.8: Electron velocities due to energy input (solid line) and electron thermal speed (dashed line). Both are mean horizontal values for a single snapshot.

fully ionized gas and constant atomic abundances. The small temperature gradients imply small deviations from the Maxwell velocity distribution. But these deviations are responsible for the heat flux. Furthermore, the complex processes in flares, where fast electrons are produced, are not considered in the Spitzer and Härm (1953) model.

6.3.2 Non-local heating

In order to find a description of the heat flux including the fast electrons, West et al. (2004) suggested the non-local heating mechanism. The fast electrons have a mean free path of several thousands of kilometers and can therefore release their energy far from the point where they are accelerated. The mechanism of non-local heat conduction comprises the long-distant effect and the sensitivity to strong temperature gradients. The latter were neglected in the Spitzer and Härm (1953) derivation. For the non-local heat flux the heat flux vector is modified:

$$q(x) = \int_0^L q_0(x')\omega(x, x')\mathrm{d}x' \tag{6.6}$$

$q_0(x)$ is the Spitzer heat flux. The kernel $\omega(x, x')$ depends on the temperature gradients and densities along the integral. Typically the integration is done along the loop, i.e. the heat flux at a given point depends on the global loop properties. For gentle temperature and density gradients the kernel acts like a delta function and the resulting heat flux is the classical Spitzer and Härm (1953) function. West et al. (2004) showed in their paper that the heat flux is on average reduced by a factor of up to two. Again, this effect is small in comparison to the uncertainty of the Spitzer heat flux.

Although equation 6.6 can easily be added to the MHD equations, it is difficult to implement in our numerical scheme, in which parallelization is used by dividing

into sub domains. Additional communication together with complex loop geometries has to be introduced. This will slow down the performance significantly, whereas the time to conduct a model is already several weeks.

7 Magnetic structures and heating

High resolution measurements of solar magnetic fields are up to now restricted to the solar surface. The structures of coronal magnetic fields are mostly derived from extrapolations of the magnetic fields on the solar surface. These extrapolations were based only on the vertical component of the magnetic field in the beginning. Nowadays, observations provide the full magnetic vector which can be used for more realistic extrapolations. Nevertheless, these models cannot reproduce the dynamics of structures but are snapshots for given photospheric magnetic field configurations. For a few observations loops were successfully aligned with magnetic fieldlines based on extrapolations. Even though there was a good visual agreement, no reliable information about the free magnetic energy could be retrieved. Thus, these models cannot explain the temporal evolution of loops nor why loops can be seen at all. With the advantage to have the full magnetic field vector at each grid point at all times, we are able to discuss the extrapolation of magnetic fields. Furthermore, loop properties, e.g. temperatures or heating rates, can be compared to standard loop models.

7.1 Non force-free state

Extrapolations of magnetic fields on the Sun are still a field of research. The simplest case is the potential field extrapolation where the magnetic field is in the lowest energy state and no currents exist. This case is easy to implement and gives a rough estimate of the magnetic field structure in the corona. More complex models use force-free extrapolations where currents are parallel to magnetic fieldlines. One distinguishes between linear and non-linear force-free extrapolations where the proportionality between the magnetic field and the current is global or only along a fieldline respectively.

When the current is parallel to the magnetic field

$$\mu_0 \mathbf{j} = \alpha \mathbf{B}$$

we can replace the current density in Ampère's law:

$$\nabla \times \mathbf{B} = \alpha \mathbf{B} \, . \tag{7.1}$$

We introduced the proportionality factor α. Thus, force-free extrapolations have to solve equation 7.1 along with the Maxwell equation (2.2):

$$\nabla \cdot \mathbf{B} = 0 \, . \tag{7.2}$$

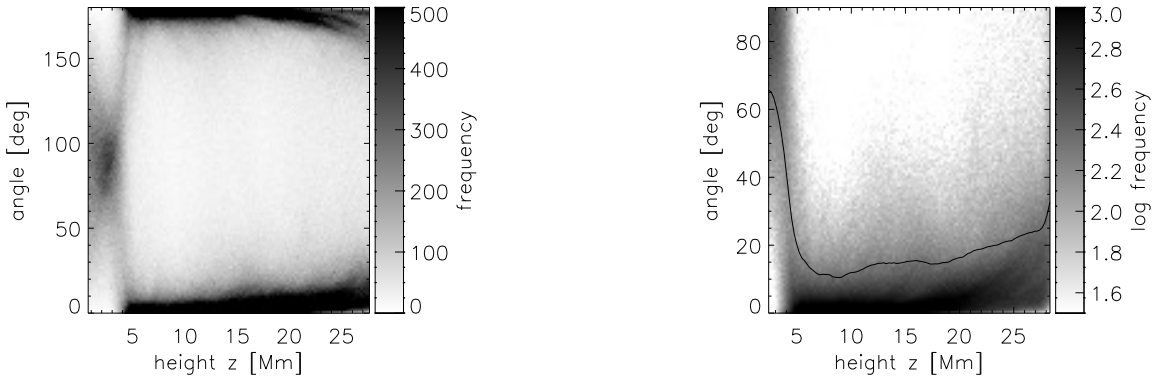

Figure 7.1: *Left*: Histogram of the angular distribution between current **j** and the magnetic field **b**. Zero degrees means parallel and 180 degrees anti parallel. *Right*: Histogram of angular distribution with no differentiation of the parallel and anti-parallel configuration. Cosine values in the second quadrant are copied into the first quadrant. The horizontally averaged mean (solid line) varies between 10 and 60 degrees.

The factor α is equal to zero in equation 7.1 for the potential field, α is constant for the linear force-free case and α depends on the space for non linear force-free extrapolations. For the latter method α is at least constant along a fieldline.

Non force-free extrapolations can be solved with the magneto-hydrostatic equations. These include the momentum equation for a steady state. That means, the Lorentz force, the pressure and the gravitational force counterbalance each other. Therefore, inversions of observations have to be performed to find a pressure distribution in the atmosphere. This among other numerical problems will reduce the accuracy of the extrapolation model.

As a consequence of the dynamic driving, the magnetic field in the corona is in a non force-free state where the currents are inclined with respect to the magnetic fieldlines. This inclination, or rather the angle between the magnetic and the current vector can be computed at each grid point. The angle distribution as a function of height (fig. 7.1) shows a broad spread. The left panel discriminates between parallel and anti parallel currents whereas in the right panel these states are combined. The mean angle (solid line) between the current and the magnetic field vector varies from 10 deg to some 60 deg. It starts with almost perpendicular currents in the photosphere and lower chromosphere and changes into almost parallel currents in the corona. Around 45% of all grid points show an angle below 10 deg, 30% below 5 deg and 0.07% below 1 deg. The potential field extrapolation is often used arguing that the stored energy amount is approximately the same. This may be correct but the spatial distribution of the magnetic energy differs significantly. In figure 7.2 (left panel), the magnetic energy distribution for the simulation and a potential field extrapolation is shown. The extrapolation is done from the photosphere up to the upper layer of the domain. At lower levels the energy density is higher for the time dependent coronal magnetic

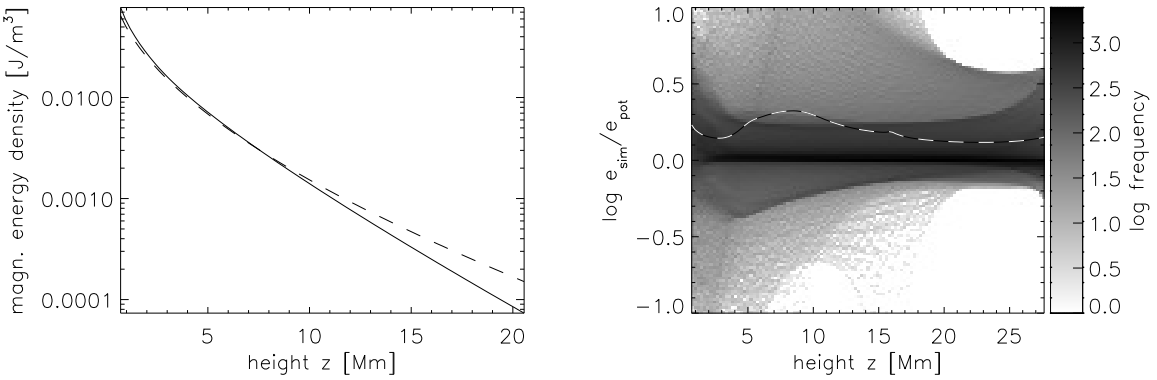

Figure 7.2: *Left*: Horizontally averaged magnetic energy density for a simulation run (solid line) and a potential field extrapolation (dashed line). The extrapolation was started at $z = 0\,\mathrm{Mm}$. *Right*: Comparison between simulation and potential field. For each height a potential field is calculated using the vertical component of the original field. The histogram shows the ratio of the energies of the fields calculated at each grid point. The horizontal average (dashed line) is approximately $\log 1.5$ to $\log 2$.

field. Above $\approx 7\,\mathrm{Mm}$ more energy is stored in the extrapolated field. The total amount of energy differs by less than 10%. Since the potential field is a state with no free energy, the question arises why less energy is stored in the corona in the simulated field. The answer is that it is a result of the assumption that the magnetic field vanishes at infinity for the potential field, whereas in reality the field may close nearby or at the top of the domain.

The right panel in 7.2 illustrates the deviation from a potential field regarding each horizontal plane separately. For the extrapolation only the vertical component of the simulated field is used. The extrapolation is done successively at each height. The resulting full magnetic vector in the respective height can then be used for comparison. The ratio of the potential and the simulated magnetic field energy is shown in the right panel of figure 7.2. Although the horizontally averaged ratio (dashed line) is much less than a factor of ten, it is positive at each height. It has maximum at $\sim 8\,\mathrm{Mm}$ of more than $\log 2$ and in the upper corona a value of $\sim \log 1.3$. This implies that the original field has a higher energy density as a potential field at the respective height. This result is consistent with the angle distribution between currents and magnetic fieldlines. The existence of currents already implies a higher energy state. Investigating sub volumes of our domain, we find areas where the potential field energy is a factor of hundred below the model magnetic field or even less.

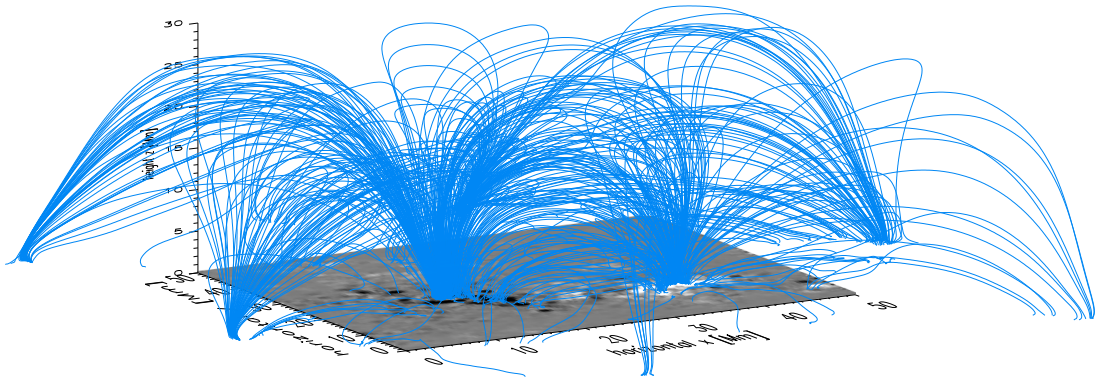

Figure 7.3: Example of fieldlines used for the analysis. Only about 5% of the total number are drawn. The lines connect to the periodically continued magnetogram in the horizontal plane. Most fieldlines arise from the main polarities and a few are low lying loops connecting network or internetwork flux.

7.2 Individual magnetic loops

Observations with TRACE in the EUV show loops with an almost constant brightness. As their length scale is bigger than the pressure scale height these loops have to be dominated by the magnetic field. The plasma is therefore confined to magnetic fieldlines. It is unclear if all solar structures, even the smaller ones, represent fieldlines since no direct measurements of the magnetic field above the photosphere are available yet. Therefore, we compute the magnetic lines of force in our domain.

7.2.1 Tracing of magnetic fieldlines

Fieldlines are traced trough the domain following the magnetic field vector. We start at an arbitrary grid point and make a step with the length of half a grid spacing in the direction of the magnetic field vector. There, the magnetic field has to be interpolated by its surrounding eight neighbors before another step of half a grid spacing can be performed. This procedure is repeated until an end criterion is valid, e.g. penetrating the upper boundary. A smaller interpolation step was tested, but did not change the result. Only for fieldlines with stronger curvature as in our model the step size should be reduced.

Since the box is periodic in x- and y-direction, fieldlines may leave the domain and enter at the opposite side. Or enter the neighboring domain, if we add several boxes together. We selected every second grid point in the horizontal and vertical directions as a starting position for the tracing routine (64^3 start positions). Then the fieldlines are traced in both directions of the magnetic field vector. Only if both foot points enter the photosphere, a fieldline is stored and used for further investigations. Starting at different heights ensures that low lying loops as well as large coronal

structures are found. Figure 7.3 illustrates the result for one single time step. The density of lines corresponds to the magnetic energy density. Fieldlines which are connected to the periodically continued magnetogram are also shown.

7.2.2 Plasma properties along loops

After tracing magnetic fieldlines throughout the domain we are able to investigate the plasma parameters along them. The fieldlines are mostly present in between grid points, thus the parameters have to be interpolated. A simple 3D linear interpolation is used for this. In the figures 7.4, 7.5 and 7.6 we demonstrate three different subsets of field lines. In a later chapter, when we discuss the scaling laws, almost all fieldlines are included in the analysis.

The figures are ordered by the loop temperature profiles and illustrate the loop density, the heating rate along the loop and the emissivities for different emission lines. Additionally, the fieldlines are shown in two projections. One view from the side showing the height and the other from above to illustrate the magnetic structures connected by the fieldlines.

Coronal loops

For figure 7.4 only loops with an average temperature above $\log T/[\,\mathrm{K}] = 5.3$ were selected. They connect the main magnetic polarities and have an apex between 10 and 30 Mm. The temperatures and densities are almost constant in the coronal part of the loop. They would therefore be considered as isothermal and isobaric loops. Indeed, the emission in Mg X is on average (red line in panel (f)) constant as well and an instrument with a dynamic range of at least a factor of 100 would see the entire coronal part of the loops. Even a single fieldline (blue line in panel (d)) shows a variation in emission only by a factor of hundred. These loops are therefore comparable to the loops seen with TRACE.
In the panel (e) we investigate the heating rate along the field lines. Unexpectedly, the heating is not uniform as the rest of the plasma parameters. Each single fieldline (one example marked as blue line) shows a huge scatter but the mean value (red line) is smooth. The peaks in these curves are resolved and are not due to numerical noise. The heating is concentrated at the foot points. The locations where the heating rate changes to almost coronal values are at 10% and 90% of the loop length. These coincide with the start of the transition region (panel (a)) and the points where the density reaches coronal values. But the emission in Mg X begins higher in the atmosphere.

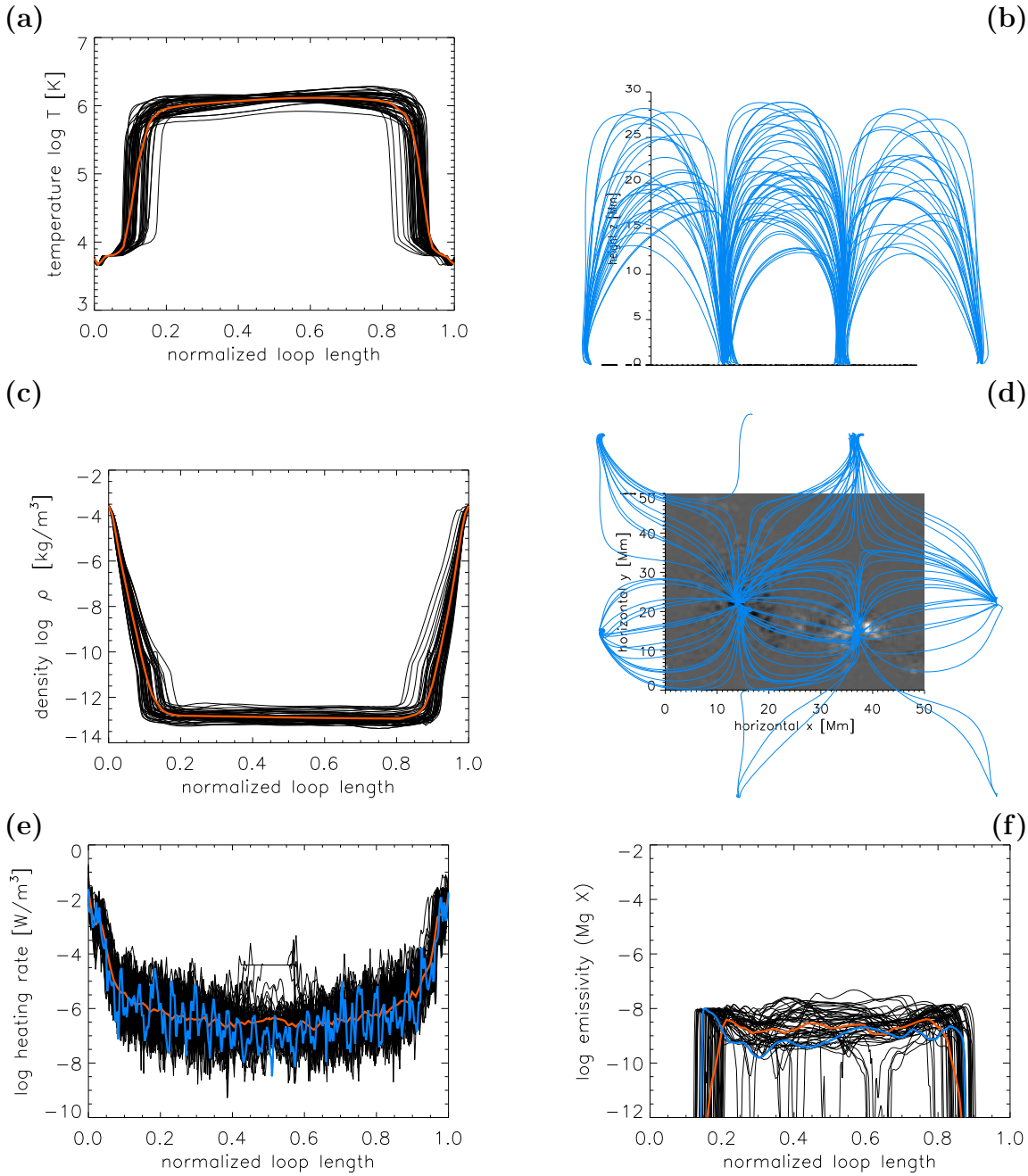

Figure 7.4: Plasma parameters along selected fieldlines. Only fieldlines with an average temperature higher than $\log \hat{T}/[\mathrm{K}] = 5.3$ are chosen. The panels show **(a)** logarithmic temperature, **(c)** logarithmic density, **(e)** logarithmic heating rate and **(f)** logarithmic emissivity in cgs units $[\frac{erg}{\mathrm{s\,cm^3}}]$. The latter illustrates the variation of the intensity for the Mg X spectral line with a formation temperature of $\log T/[\mathrm{K}] = 6.05$. Red lines in panels **(a)**, **(c)**, **(e)** and **(f)** are the mean value for the subset. One selected fieldline is illustrated in both panel **(e)** and **(f)** (thick blue). Panels **(b)** and **(d)** show the fieldlines as seen along the y-direction and from above.

Low lying loops

For figure 7.5 only loops with an average temperature between $\log T/[\,\mathrm{K}] = 3.9$ and $\log T/[\,\mathrm{K}] = 4.8$ were selected. As seen in panels (b) and (d), these fieldlines connect the main polarities with smaller and weaker magnetic patches. The apex are between 4 and 10 Mm. The shapes are far from being half circles and a few lines even have two maxima. The temperature profiles also show more than one maximum. These loops are not isothermal and cover a wide range of temperatures. One fieldline is highlighted in all panels (dark blue line in panel (b) and (d) and blue line in the other panels). The densities show the same behavior as the temperatures. As for the large loops the heating rate shows a huge scatter.
The panels (f), (g) and (h) illustrate the emission for different emission lines with formation temperatures of $\log T/[\,\mathrm{K}] = 6.5$ for Mg X, $\log T/[\,\mathrm{K}] = 4.91$ for C III and $\log T/[\,\mathrm{K}] = 4.44$ for Si II. The hotter loops are still observable in the Mg X line but do not show a constant brightness in the upper part. When observing in the cooler lines, C III or Si II, no loop structures would be seen. Along each fieldline small parts are bright in these spectral lines whereas other parts do not show any emissivity at all.

Chromospheric loops

For figure 7.6 only loops with an average temperature below $\log T/[\,\mathrm{K}] = 3.8$ were selected. As shown in panel (b) these loops do not reach the transition region. Their temperature profile is influenced by the Newton cooling term (see section 2.7.6) which was introduced to stabilize the chromosphere. Thus, the chromosphere was excluded from our analysis and no emission line for that temperature range was computed. The figure emphasizes how structured the lower atmosphere is when we look at the densities along the fieldlines (see panel (c)).

7.2.3 Hydrostatic loops

In this chapter we want to describe coronal loops as a result of the hydrostatic solutions. This approach was already used by Rosner et al. (1978). Using the hydrostatic assumption means that the hydrostatic equation and the energy equation have to be solved:

$$\nabla_s p = -\mathbf{g}_s \rho \tag{7.3}$$

$$E_H(s) - E_R(s) - E_C(s) = 0 \tag{7.4}$$

where s denotes the coordinate along the loop. These equations state that the amount of heat E_H has to be counter balanced either by radiative loss E_R, conduction E_C or both. And the pressure balances the gravitational force, i.e. the loops are in steady state. First attempts to solve the equations, made by Rosner et al. (1978),

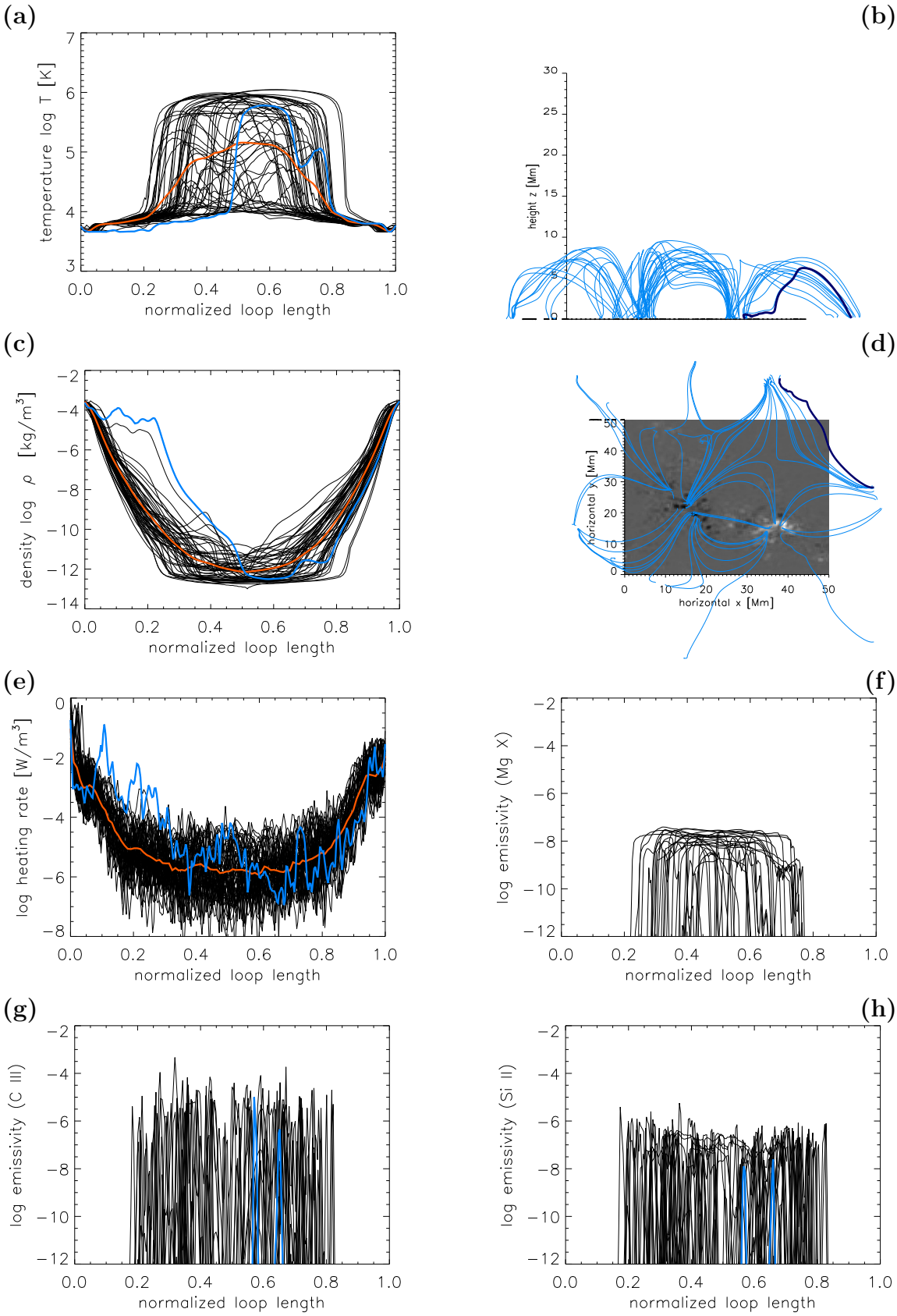

Figure 7.5: The panels show the same plasma parameters as in figure 7.4. Only fieldlines with an average temperature between $\log \hat{T}/[\mathrm{K}] = 3.9$ and $\log \hat{T}/[\mathrm{K}] = 4.8$ are chosen. The panels **(g)** and **(h)** illustrate the line intensity of the spectral lines C III and Si II.

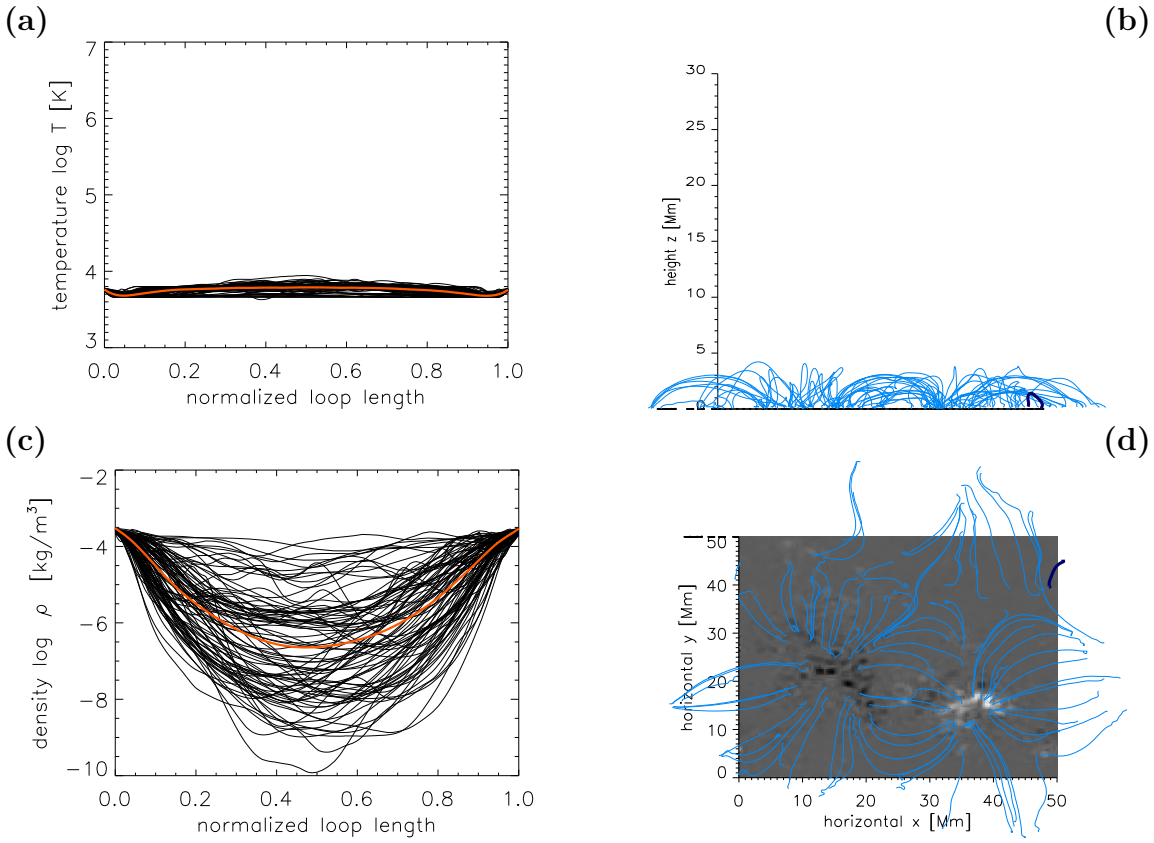

Figure 7.6: The panels show the same plasma parameters as in figure 7.4. Only fieldlines with an average temperature below $\log \hat{T}/[\mathrm{K}] = 3.8$ are chosen.

used a constant heating rate $E_H(s) = constant$ and a constant pressure along the loop. Along with a strongly simplified radiative loss function and some other approximations they were able to solve the energy equation analytically and found the well known RTV (Rosner, Tucker and Vaiana) scaling laws, expressed in SI units:

$$T_{\max} = 1.4 \cdot 10^4 \, (pL)^{\frac{1}{3}} \tag{7.5}$$

More sophisticated models later included non-uniform heating (exponential) and non constant pressure (Serio et al., 1981; Aschwanden, 2006). They found scaling laws similar to RTV with additional dependencies on the heating scale height and pressure scale height. Comparisons with observations show that RTV scaling laws fit only to small hot loops. Other types of loops can be explained by newer models.
Before investigating the properties of the fieldlines, we compute the hydrostatic equilibrium of the entire atmosphere. It is given by

$$\frac{\partial p}{\partial z} = -\rho g$$

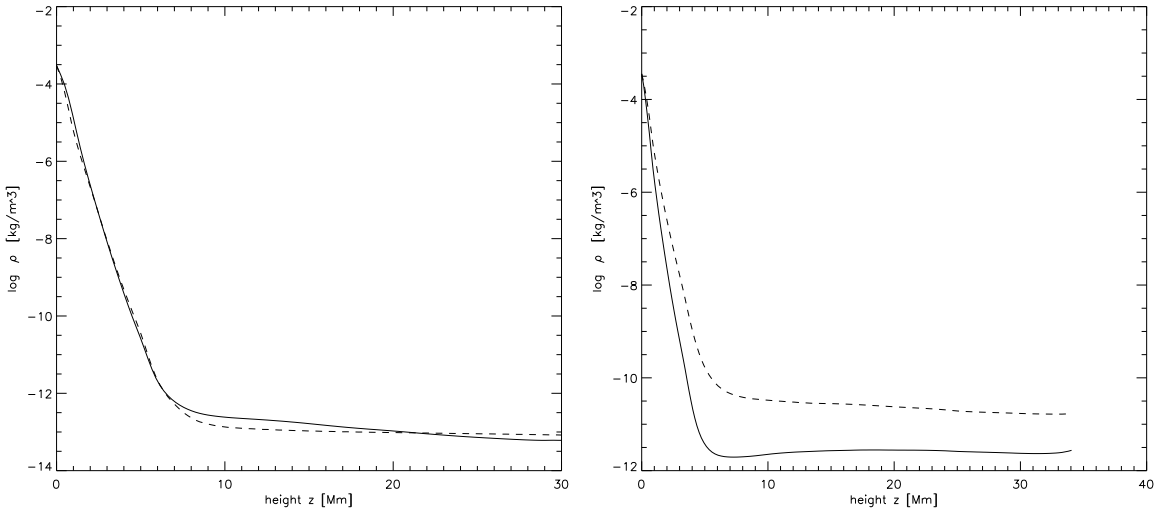

Figure 7.7: Horizontally averaged density (solid line) and density profile of a hydrostatic atmosphere (dashed line) with the same mean temperature profile. *Left*: Simulation described in this work, *Right*: Results from (Gudiksen and Nordlund, 2005)

Along with the equation of state for an ideal gas (eq. (2.31)) it can be written as

$$\ln \rho(z) = \ln \rho_0 - \ln \frac{T(z)}{T_0} - \frac{1}{(c_p - c_v)} \int_{z_0}^{z} \frac{g}{T} dz \tag{7.6}$$

To evaluate this integral numerically we used horizontally averaged temperature profiles and a constant gravity ($g_0 = 274 \frac{m}{s^2}$). Figure 7.7 illustrates the comparison of the hydrostatic density profile (dashed line) to the simulated density profile (solid line) for both the model described in this thesis and the model by Gudiksen and Nordlund (2005). Our atmosphere seems to be close to a hydrostatic atmosphere, but in equation 7.6 the dominant force in the corona, the Lorentz force, was neglected. However, the figure shows a clear difference between the two models. In the model of Gudiksen and Nordlund (2005) the density is lower in comparison to the hydrostatic solution.

Loop scaling laws

Loops with an apex higher than 10 Mm were selected for figure 7.8. It shows the relation between the maximum temperature versus its corresponding pressure at this point times the length of the fieldline. Fieldlines are not shaped like half circles and may have more then one apex. The maximum temperature is not necessarily at the top of the fieldline.

Clusters of fieldlines in this histogram may represent one specific loop as a fieldline does not represent a volume.

The dashed line is a linear fit and has a slope on the order of $\frac{1}{3}$. The slope and intercept of the linear fit depend on the selection criteria for fieldlines, e.g. the

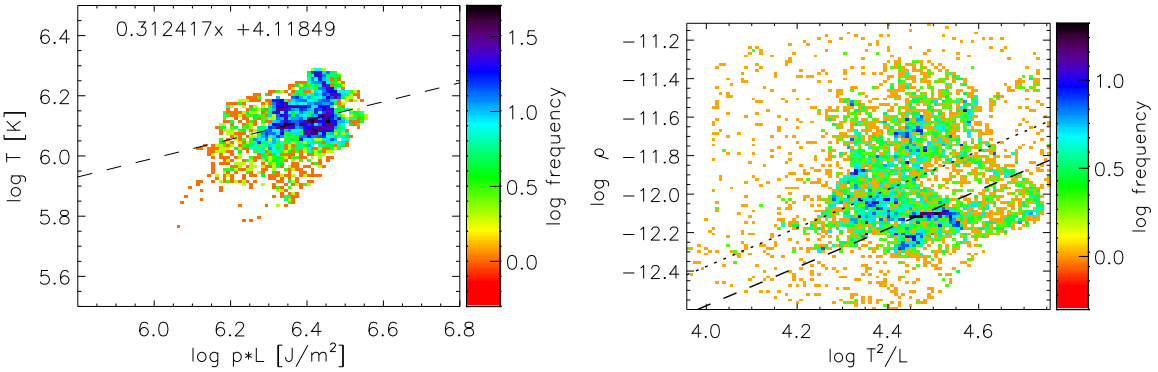

Figure 7.8: *Left*: Histogram of fieldlines, with apex higher than 10 Mm, according to maximum temperature and pressure times fieldline length. The dashed line is a linear fit $T = 1.31 \cdot 10^4 (pL)^{\frac{1}{3.21}}$. The mean absolute deviation of $\log T/[\mathrm{K}]$ is $\sigma = 0.054$. *Right*: The same set of field as in the left panel. Histogram of loop densities versus loop temperatures and lengths. Dashed line represents the equation 7.8 and the dotted line is fitted with a fixed slope of one. The fit results in an intercept of -16.38 ± 0.0036.

maximum loop temperature or different minimum apex heights. It varies for the slope between $\frac{1}{3}$ and $\frac{1}{2}$ and between 3 to 4 for the intercept.

This result corresponds nicely to the scaling laws found for uniform (Rosner et al., 1978) and non-uniform heating (Aschwanden and Schrijver, 2002) along the loops. The RTV scaling law

$$T_{max} = 1.4 \cdot 10^4 \, (pL)^{\frac{1}{3}} \tag{7.7}$$

can be rewritten using the equation of state for an ideal gas (eq. 2.31) to

$$\begin{aligned} \rho &= \frac{3.64 \cdot 10^{-13}}{c_p - c_V} \frac{T^2}{L} \\ \log \rho &= \log \frac{T^2}{L} - 16.58 \end{aligned} \tag{7.8}$$

This correlation is shown on the right side of figure 7.8 for one snapshot. The dashed line shows the function derived from RTV scaling, the dotted line is a fit with a slope of 1 to the data. The intersect is -16.38 ± 0.0036. Again, this result fits nicely to observations and shows that on average the loops are over-dense. Aschwanden (2006) gives the height of the loop base at 1.3 Mm. In contrast, the exponential decay of the heating rate in our model starts at 4.7 Mm. This may be a result of the not perfectly described chromosphere or the missing chromospheric physics. However, other properties match the results by Aschwanden (2006) quite well. E.g. the loop base temperature at $z = 4.7\,\mathrm{Mm}$ is $T_0 = 10^4\,\mathrm{K}$. These results are mean values of quantities which have a large scatter. Individual loops show strong deviations from the scaling laws.

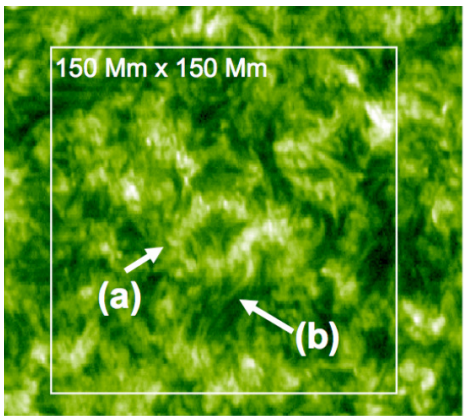

Figure 7.9: Quiet Sun network in the emission line of O VI at 103.2 nm formed around 300.000 K (SOHO/SUMER, http://www.mps.mpg.de/projects/soho/sumer/).

7.3 iLoops

Images of the Sun in X-rays show a corona which is dominated by loop structures formed by plasma at high temperatures of about 10^6 K and number densities of about 10^{15}–10^{16} m^{-3} (cf. 1.4). New measurements with the two STEREO spacecraft allow a stereoscopic view of the corona and thus a reconstruction of the coronal structures in three dimensions. As expected, large isolated coronal loops, with lengths of more than 10% of the solar radius, roughly follow magnetic fieldlines determined from extrapolations of the measured surface magnetic field (Feng et al., 2007). Based on this paradigm, namely that bright loops seen in solar X-ray and extreme ultraviolet (EUV) emission follow magnetic fieldlines, numerous corona models have been built in the framework of loop models. This solar paradigm is also applied to other stars, not only to those which are solar-like, but also to stars being much more active than our Sun. Even though this concept is very attractive and certainly valid for the large loop systems seen in Active Regions on the Sun, one should carefully evaluate to what extent it can be generalized. On the solar surface the super-granular flow forms a complex magnetic network with a typical cell size of about 20 Mm. These spatially complex concentrations of magnetic fields harbor small loop-like structures seen in EUV emission lines formed at temperatures at and above 10^5 K. Mostly these cool loops are very short, barely resolvable with lengths of below 5 Mm, which is less than 1% of the solar radius (labeled a in 7.9). Some of these structures seem to be low-lying long loops crossing the network cells (labeled b). It is unclear whether these small structures are of the same nature as the larger structures seen at hotter temperatures on the Sun, i.e. if the network loop-like structures follow magnetic fieldlines, too. This seems unlikely, though, as the surface magnetic field below these structures is often unipolar, and so no magnetic loops should emerge to heights of several Mm. This poses the question as to the nature of these loops. It will be answered later

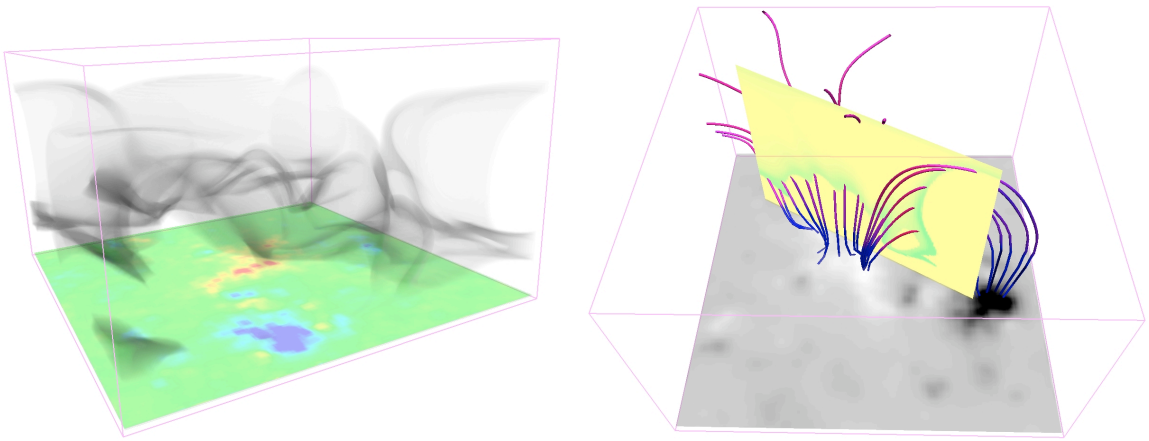

Figure 7.10: *Left*: 3D Visualization of the emission in Ne VIII (inverse gray scale) in the model. At the bottom of the box the (vertical) magnetic field is shown with the opposite main polarities and the surrounding network magnetic patches. The loop-like structures seen in intensity, the iLoops, show no direct connection to the underlying magnetic field. *Right*: Vertical cut through the box showing the Ne VIII emission (green on yellow plane). At the bottom the (vertical) magnetic field is shown (gray is zero field). Selected field lines are drawn, which intersect the region of high Ne VIII emission in the vertical cut. The temperature along the fieldline is color coded from blue (10^4 K) to pink ($2{\cdot}10^6$ K). Both panels are compiled with VAPOR.

in terms of "iLoops", i.e. loops that appear only as intensity enhancements, not necessarily following the magnetic field. Current observations simply do not have the spatial and temporal resolution to decide on this. Another question is even more tempting: What is the nature of structures to be expected in the coronae of stars being more active (and presumably magnetically more complex) than our Sun? Are they closer in nature to the large hot loops in the solar corona or to the small loop-like structures in the magnetically complex solar network? In order to investigate the formation of structures in the hot corona we compare the result from the model presented in this thesis and former simulations with different boundary conditions. In previous models we used the same boundary condition for the magnetic field as in Gudiksen and Nordlund (2005). Both models used the scaled down Active Region but without the additional network flux as described in chapter 3. As in the the study in (Gudiksen and Nordlund, 2002, 2005; Peter et al., 2004) the model without network flux shows a large coronal loop tracing the magnetic field lines. The model presented in this work also show loop like structures (cf. figure 5.10). To understand the connection between structures seen in intensity and the underlying magnetic field we looked at the 3D box from different angles. The loops change their form or even disappear with other loops appearing at other places (cf. 7.10 for a 3D visualization of the coronal emission). In the 3D box the emission of Ne VIII is originating from a relatively thin surface which is highly corrugated. Depending on the viewing angle

the contribution along the line-of-sight can change significantly across the complex surface of the coronal emission.

To further illustrate this we plotted in the right panel of figure 7.10 a vertical cut through the box showing the emission in Ne VIII. Over-plotted are fieldlines which cross this vertical cut where the Ne VIII emission is high. The color along the fieldlines indicates the temperature at the respective location. A closer inspection shows that the temperature is non-constant along the fieldline. Consequently, the emission seen in a specific emission line, e.g. the Ne VIII, is formed over a small fraction of the fieldline — for some fieldlines the formation temperature of Ne VIII is reached at the top (right of 7.10), for some at intermediate heights (left). As the formation temperature of a given emission line is reached at a different height along each fieldline, this results in the complex corrugated source region as mentioned above. The consequence of the complex magnetic field structure is that the distribution of the energy dissipated in the coronal volume also becomes more complex. That naturally produces a more complex temperature structure both along and across the magnetic field, thus the structures that can be identified are in general structures which, in projection are overlapping.

8 Discussion

We presented in this work a self-consistent model of the solar corona above an Active Region. Photospheric motions braid the magnetic fields lines, which leads to currents in the upper atmosphere. Dissipation of these currents heats the corona and sustains coronal temperatures of roughly one million degrees. The processes of heat conduction, heating and radiative cooling are in equilibrium and the model is in a quasi-stationary state. We synthesized emission lines and derived thereof quantities comparable with solar observations. The comparison with observations shows already a good agreement but is discussed in more detail in the PhD thesis of P. Zacharias.

In this work we focus on the heating process and investigate its temporal and spatial evolution. The Ohmic heating is strong enough to heat the corona. The energy flux at the base of the corona, derived from the volumetric heating rate, is in the order of the value required by theoretical models as well as in the order of the heat flux derived from observations. The heating rate decays exponentially with height starting at the transition region and increases strongly towards the photosphere. Magnetic loops in the model are heated at their foot points. The heating rate shows spatially and temporally resolved events. These events can be categorized into Nanoflares or in groups of Nanoflares, the so-called Nanoflare storms. In the chromosphere and the transition region events have a typical energy of $10^{16} - 10^{-19}$ J, but the average energy density for an event decreases with height. The decrease is also explained with the exponential decrease of the average Ohmic heat.

We derived a Nanoflare distribution similar to observations. To obtain this we assumed that every event is visible and is 'observed' in our model from above. The resulting energy distribution per unit time and unit area has a slope as predicted from theoretical models. This is the first time that the Nanoflare distribution was found self-consistently in a numerical model. This result can be used as an input for models which focus on other physical effects. For example models based on the Boltzmann equation or models describing the radiative transfer in detail.

A result of line emission studies is that one can see loop-like structures, also above mono-polar magnetic patches: these iLoops do not follow the magnetic field but are a projection effect. This provides a novel explanation for the loop-like structures seen above network patches in the quiet Sun. The iLoops are seemingly not connected to the surface magnetic structures, if considering only the EUV emission patterns. Nonetheless each location where one sees this emission, e.g. in O VI, is magnetically

connected to the solar surface. However, the ends of the iLoops do not point to a location on the surface that is connected to the loop, because the iLoop is a projection effect. Thus the failure of previous studies trying to connect the 'foot points' of the iLoops to photospheric and chromospheric patches is understandable (Feldman et al., 2001).

Stars more active than our Sun can be expected to have quite a different structure of the surface magnetic fields. Observations using Doppler-(Zeeman)-imaging techniques show large polar spots, active longitudes, or a generally higher level of surface filling of magnetic fields. As an example, based on surface magnetic fields derived by Doppler-Zeeman-imaging a reconstruction of the appearance of the corona of AB Dor was done (Jardine et al., 2002). Also in general, many models for stellar coronae assume (sometimes implicitly) that the emission from a corona is originating from numerous loops (Schrijver and Title, 2005) following the magnetic field lines, i.e. bLoops.

However, on other (perhaps more active) stars a higher complexity of the surface magnetic field might well lead to effects as found in this study with the iLoops for complex solar network patches, but then on a larger scale. Thus it might be possible that the emission from more active coronae is not dominated by loops following magnetic fieldlines, but by structures more closely related to the iLoops. This would be of pivotal importance for our understanding of stellar coronae in general and deserves further investigations in the future.

Nevertheless, we should remember the limitations of our numerical model. The magnetic diffusivity used in our box is larger by several orders of magnitude in comparison to solar values and is in addition spatially constant. We argue that a larger number is meaningful due to the time scale comparison. Using solar values would result in an almost non-resistive simulation. But, future numerical experiments should consider the spatial variation due to the temperature dependency. Also, the dynamic viscosity has to be used with its dependency on temperature.

A Appendix

A.1 Conduction of the numerical experiment

The numerical simulations discussed in this thesis were done at the Kiepenheuer Institut für Sonnenphysik in Freiburg. The institute provides a computer cluster with 92 cores with unlimited access. The cluster is composed of 23 nodes, DELL Poweredge 1950 Server, with two 3 GHz Intel CoreDuo (TM) Xeon processors each. A node has 4 GB main memory and communicates via InfiniBand with other nodes. This fast inter-node communication channel is vital for parallelized schemes such as the Pencil Code.

A.1.1 Timings and volume of data

The model described in chapter 3 has 128^3 grid points and used 16 nodes of the computer cluster. It takes about one week to simulate one solar hour. Increased resolution, for example using 256^3 grid points, needs roughly 40 times more. This results from 8 times more grid points and a time step for heat conduction decreased by factor of 4.

A snapshot of all physical parameters has a size of 127 MB. We recorded two solar hours with a cadence of 30 seconds. Therefore, we have in total 240 snapshots, which corresponds to 29.7 GB.

A.1.2 Boundary conditions

The labels given in the table A.1.2 are directly usable in control files of the code. Their meaning is

- 'a' antisymmetric: $f = 0$ at the boundary
- 's' symmetric: $f' = 0$ at the boundary
- 'a2' antisymmetric: $f'' = 0$ and $f \neq 0$ at the boundary
- 'g' : first set u_x and u_x at boundary then apply 'a2'
- 'rho' : extend the data below the photosphere (ghost cells) with solar values

	u_x	u_y	u_z	$\ln \rho$	$\ln T$	A_x	A_y	A_z
lower boundary	g	a2	a	rho	set	fBs	fBs	a2
upper boundary	s	s	a	s	s	pwd	nil	a2

Table A.1: Boundary conditions used for the simulation presented in this work.

- 'set' : set f to given value then apply 'a2'
- 'fBs' : set diffusion η to zero at the boundary and apply 's'
- 'pwd' : calculate potential field extrapolation
- 'nil' : do nothing

where f stands for the variables u_i, $\ln \rho$, $\ln T$ and A_i.

A.1.3 Units in the code

All physical parameters are unified using a conversion system. A variable Π_p used in the code can be expressed in SI units or vice versa using the unit value $[\Pi]$ like:

$$\Pi_P \cdot [\Pi] = \Pi_{SI}$$

The following units are given as initial parameters

$$[\rho]\ [l]\ [v]\ \ .$$

This defines the units of the energy E and the time t:

$$[t] = \frac{[l]}{[v]}$$
$$[E] = [\rho][v]^2[l]^3$$

Furthermore, the unit of the magnetic field B is defined by setting $\mu_{0_{Pencil}} = 1$ using the magnetic energy density e_B

$$e_B = \frac{B^2}{2\mu_0}$$
$$[B] = \sqrt{\frac{\mu_{0_{SI}}}{\mu_{0_{Pencil}}} \frac{J}{m^3}}$$
$$[B] = \sqrt{\mu_0[\rho][v^2]} = [v]\sqrt{\mu_0[\rho]}$$

where $\mu_0 = 4\pi \cdot 10^{-7}$. The unit of the temperature is defined via the internal energy

$$e = c_V T \tag{A.1}$$

with $(c_p - c_V) = R/\mu$ and $c_p/c_V = \gamma$ we can write

$$[T] = \frac{\mu(\gamma - 1)[v^2]}{R} \tag{A.2}$$

where $\gamma = \frac{5}{2}$ and $c_p = 1$ in the code.

A.2 The k-ω-diagram

For a time dependent quantity $F = F(x, y, t)$ given at a plane one can compute a k-ω-diagram. It represents the power spectrum in the temporal and spatial domain. We compute the three dimensional Fourier spectrum:

$$\hat{F}(k_x, k_y, \omega) = fft(F(x, y, t)) \tag{A.3}$$

The power spectrum is then given by the absolute value:

$$P(k_x, k_y, \omega) = \sqrt{\hat{F}(k_x, k_y, \omega)^2}$$

Introducing polar coordinates $k = \sqrt{k_x^2 + k_y^2}$ in the spatial domain and integrating azimuthal gives the two dimensional k-ω-diagram

$$\hat{P}(k, \omega) = \int_k P(k, \phi, \omega) k \mathbf{d}\phi \tag{A.4}$$

A.3 Diffusion along fieldlines

The Spitzer heat conduction used in model conforms a diffusion along field lines with spatial dependent coefficient. In order to implement the heat conduction term in the energy equation into the code, we have to derive a useful form. All product rules have to be evaluated and only first and second order derivatives of code variables, such as temperature or density, are allowed. The diffusion along a fieldline for an arbitrary coefficient K reads:

$$\mathcal{D}e = \partial_i \left(K_{ij} \partial_j e \right) \tag{A.5}$$

$$\mathcal{D}e = \left(\partial_i K_{ij} \right) \partial_j e + K_{ij} \left(\partial_i \partial_j e \right) \tag{A.6}$$

The coefficient K is composed of a parallel and a perpendicular part

$$K_{ij} = K_\perp \delta_{ij} + \left(K_\parallel - K_\perp \right) b_i b_j \tag{A.7}$$

The derivative hereof is:

$$\partial_i K_{ij} = \partial_j K_\perp + \left(\partial_i K_\parallel - \partial_i K_\perp\right) b_i b_j + \left(K_\parallel - K_\perp\right) \partial_i \left(b_i b_j\right)$$

We define H to make the result more readable as:

$$\begin{aligned}
H_j &= \partial_i \left(b_i b_j\right) \\
&= \partial_i \frac{B_i B_j}{B_k B_k} = \frac{\partial_i \left(B_i B_j\right)}{B_k B_k} - \frac{b_i b_j}{B_k B_k} 2 B_l \partial_i B_l \\
&= \Big[\underbrace{\left(\partial_i B_i\right)}_{\nabla B = 0} B_j + B_i \partial_i B_j - 2 b_i b_j B_l \partial_i B_l\Big] \frac{1}{|\mathbf{B}|^2} \\
&= \left[b_i \partial_i B_j - 2 b_i b_j b_l \partial_i B_l\right] \frac{1}{|\mathbf{B}|} \\
&= \left(b_i \delta_{jl} - 2 b_i b_j b_l\right) \frac{\partial_i B_l}{|\mathbf{B}|} \\
&= \left(\delta_{jl} - 2 b_j b_l\right) b_i \frac{\partial_i B_l}{|\mathbf{B}|}
\end{aligned} \tag{A.8}$$

All together the diffusion along fieldlines reads then

$$\begin{aligned}
\mathcal{D}e = \quad & \nabla K_\perp \cdot \nabla e + \left(\mathbf{b} \cdot \nabla K_\parallel - \mathbf{b} \cdot \nabla K_\perp\right) \left(\mathbf{b} \cdot \nabla e\right) \\
& + \left(K_\parallel - K_\perp\right) \mathbf{H} \cdot \nabla e + K_\perp \Delta e + \left(K_\parallel - K_\perp\right) \left[\left(e_{ij} \cdot \mathbf{b}\right) \cdot \mathbf{b}\right]
\end{aligned}$$

where e_{ij} is the Hesse-Matrix of e.
For constant $K_\parallel K_\perp$ the equation reduces to

$$\mathcal{D}e = + \left(K_\parallel - K_\perp\right) \mathbf{H} \cdot \nabla e + K_\perp \Delta e + \left(K_\parallel - K_\perp\right) \left[\left(e_{ij} \cdot \mathbf{b}\right) \cdot \mathbf{b}\right]$$

In the case of Spitzer heat conduction, we have

$$\begin{aligned}
K_\perp &= 0 \\
K_\parallel &= K_0 T^{2.5} \\
\nabla K_\parallel &= \frac{5}{2} K_0 T^{2.5} \nabla \ln T
\end{aligned}$$

Therefore

$$\begin{aligned}
c_v \rho T \frac{\partial \ln T}{\partial t} &= \left(\mathbf{b} \cdot \nabla K_\parallel\right) \left(\mathbf{b} \cdot \nabla T\right) + K_\parallel \mathbf{H} \cdot \nabla T + K_\parallel \left(T_{ij} \circ \mathbf{b}\right) \cdot \mathbf{b} \\
&= K_0 T^{3.5} \left(\frac{5}{2} \left(\mathbf{b} \cdot \nabla \ln T\right)^2 + \mathbf{H} \cdot \nabla \ln T + \left(\ln T_{ij} \circ \mathbf{b}\right) \cdot \mathbf{b}\right) \\
\frac{\partial \ln T}{\partial t} &= \frac{K_0 T^{2.5}}{c_v \rho} \left(\frac{5}{2} \left(\mathbf{b} \cdot \nabla \ln T\right)^2 + \mathbf{H} \cdot \nabla \ln T + \left(\ln T_{ij} \circ \mathbf{b}\right) \cdot \mathbf{b}\right)
\end{aligned} \tag{A.9}$$

where the last line represents the form implemented in the code.

A.4 Calculation of number densities

The radiative losses, cf. equation (2.41), depend on the electron and proton number densities. Therefore we need to find the correlation between the number densities n and the density ρ used in the code. For a fully ionized gas of hydrogen and helium with an abundance of $\log\frac{n_{He}}{n_H} + 12 = 10.93$, from Stix (1989) the electron number density is

$$n_e = n_p + 2\,n_\alpha = n_p\,(1 + 0.17) = 1.17 n_p$$

The mean atomic mass is

$$\mu \;=\; \frac{n_e m_e + n_p m_p + n_\alpha m_\alpha}{n_e + n_p + n_\alpha} = 0.595\,m_p$$

The total and electron number densities are given by

$$\begin{aligned} n &= \frac{\rho}{\mu} = 1.68\,\frac{\rho}{m_p} \\ n_e &= 0.519 \cdot n = 0.872\,\frac{\rho}{m_p} \end{aligned}$$

$$n_e n_p = \frac{0.872^2}{1.17}\left(\frac{\rho}{m_p}\right)^2$$

We used the given abundance for the entire domain and assumed a fully ionized gas.

A.5 Potential field extrapolation

The simplified Maxwell equation 2.10 reduces for a force free field to $\nabla \times \mathbf{B} = \alpha\mathbf{B}$, and for a potential field to $\nabla \times \mathbf{B} = 0$. Thus one has to solve

$$\begin{aligned} \nabla \times \mathbf{B} &= 0 \\ \nabla \cdot \mathbf{B} &= 0 \end{aligned} \tag{A.10}$$

This implies that the magnetic field can be derived from a potential

$$\mathbf{B} = \nabla\Phi \tag{A.11}$$

Following Bracewell (1965), we take the Fourier transform of A.10

$$\begin{aligned} k_x\hat{B}_x + k_y\hat{B}_y + \partial_z\hat{B}_z &= 0 \\ ik_y\hat{B}_z - \partial_z\hat{B}_y &= 0 \\ \partial_z\hat{B}_x - ik_x\hat{B}_z &= 0 \\ ik_x\hat{B}_y - ik_y\hat{B}_x &= 0 \end{aligned} \tag{A.12}$$

and assume an exponentially decaying Fourier transform of the vertical magnetic field:

$$\hat{B}_z(k_x, k_y, z) = e^{-kz}\hat{B}_z(k_x, k_y, z = 0) \tag{A.13}$$

where k_x and k_y are the coordinates in Fourier space and z is the height. The observed vertical component of the magnetic field in the photosphere is used as boundary condition $\hat{B}_z(k_x, k_y, z = 0)$. Combining everything we get

$$\begin{aligned} \hat{B}_x &= -i\frac{k_x}{k}\hat{B}_z \\ \hat{B}_y &= -i\frac{k_y}{k}\hat{B}_z \end{aligned}$$

with $k^2 = k_x^2 + k_y^2$. Since we are interested in the vector potential we have to solve:

$$\begin{aligned} \hat{B}_x &= ik_y\hat{A}_z - \partial_z\hat{A}_y \\ \hat{B}_y &= \partial_z\hat{A}_x - ik_x\hat{A}_z \\ \hat{B}_z &= ik_x\hat{A}_y - ik_y\hat{A}_x \end{aligned} \tag{A.14}$$

This leads to:

$$\begin{aligned} \hat{A}_x &= -i\frac{k_y}{k^2}\hat{B}_z \\ \hat{A}_y &= i\frac{k_x}{k^2}\hat{B}_z \\ \hat{A}_z &= 0. \end{aligned} \tag{A.15}$$

A.6 Power law of a 2D velocity map

In chapter 3 we used a power spectrum to compare the velocity boundary condition with the photospheric motions on the Sun. We start with a velocity map $v(x, y)$ in units of $[v] = u_v$. This unit may be $\frac{\mathrm{m}}{\mathrm{s}}$. The Fourier transformed field $F_v = fft(v)$ then has the units of $[F_v] = u_v u_l^2$, since we apply the transformation in two dimensions. Here we used u_l as the unit length. The new field is in the coordinates of the wave number vector, $F_v = F_v(k_x, k_y)$. We can derive the 2D power spectrum by taking the absolute value of the Fourier transformed field,

$$\begin{aligned} p(k_x, k_y) &= \sqrt{|F_v|^2} \\ [p] &= u_v u_l^2 \end{aligned}$$

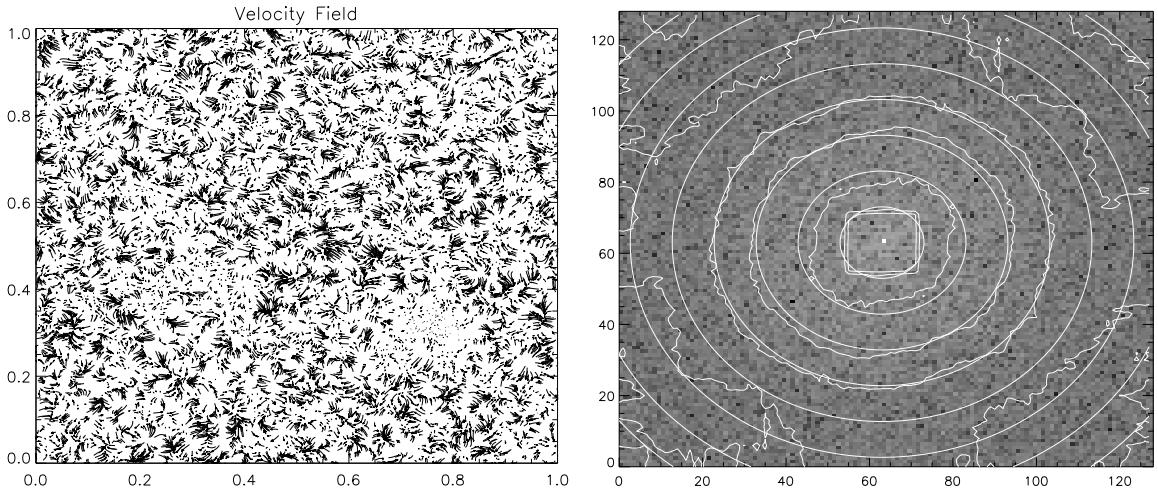

Figure A.1: *Left*: Velocity field. Vector lengths indicate the absolute value. *Right*: 2D power spectrum. Solid lines illustrate contours and lines of constant **k**.

Assuming that the velocity field has no preferred direction, the 2D power spectrum is symmetric. We can apply cylindrical coordinates with

$$\begin{aligned} k &= \sqrt{k_x^2 + k_y^2} \\ k_x &= k\cos\phi \\ k_y &= k\sin\phi \\ p &= p(k,\phi) \end{aligned}$$

We now conduct an azimuthal integration

$$\hat{p} = \int pk\mathbf{d}\phi$$

Integrating over rings, indicated by the circles om the right hand side of figure A.6, gives the representative power spectrum depending on k. Therefore $p(\hat{k})$ has the units of $[p] = u_v u_l$. It is common to plot $\hat{p}\cdot k$, cf. panel on the left hand side of figure 3.4, which has the units of u_l, over the spherical harmonic wave number $l(l+1) = k^2r^2$. Here r is the solar radius and should be in the same units as the wave vector k. Then the spherical harmonic wave number is dimensionless.

List of Figures

Index

Bibliography

H. Alfvén. On Sunspots and the Solar Cycle. *Arkiv for Astronomi*, 29:1–17, 1943.

A. Aschwanden. *Physics of the solar corona*. Springer-Verlag Berlin Heidelberg New York, 2006.

M. J. Aschwanden and C. J. Schrijver. Analytical Approximations to Hydrostatic Solutions and Scaling Laws of Coronal Loops. *APJ*, 142:269–283, October 2002. doi: 10.1086/341945.

T. E. Berger, M. G. Löfdahl, R. A. Shine, and A. M. Title. Measurements of Solar Magnetic Element Dispersal. *APJ*, 506:439–449, October 1998. doi: 10.1086/306228.

T. J. M. Boyd and J. J. Sanderson. *The Physics of Plasmas*. Physics of Plasmas, February 2003.

R. Bracewell. *The Fourier transform and its applications*. McGraw-Hill, New York, 1965.

A. Brandenburg. *Computational aspects of astrophysical MHD and turbulence*, pages 269–+. Advances in Nonlinear Dynamics, 2003.

A. Brandenburg and W. Dobler. Hydromagnetic turbulence in computer simulations. *Comp. Phys. Comm.*, 147:471–475, 2002.

J. Clyne and M. Rast. A prototype discovery environment for analyzing and visualizing terascale turbulent fluid flow simulations. *Proceedings of Visualization and Data Analysis*, pages 284–294, 2005.

J. W. Cook, C.-C. Cheng, V. L. Jacobs, and S. K. Antiochos. Effect of coronal elemental abundances on the radiative loss function. *APJ*, 338:1176–1183, March 1989. doi: 10.1086/167268.

R. Courant, K. Friedrichs, and H. Lewy. Über die partiellen Differenzengleichungen der mathematischen Physik. *Mathematische Annalen*, 100:32–74, 1928.

I. de Moortel, P. Browning, S. J. Bradshaw, B. Pintér, and E. P. Kontar. The way forward for coronal heating. *Astronomy and Geophysics*, 49(3):030000–3, June 2008. doi: 10.1111/j.1468-4004.2008.49321.x.

V. Domingo, B. Fleck, and A. I. Poland. The SOHO Mission: an Overview. *Solar Physics*, 162:1–2, December 1995. doi: 10.1007/BF00733425.

B. Edlén. Die Deutung der Emissionslinien im Spektrum der Sonnenkorona. Mit 6 Abbildungen. *Zeitschrift fur Astrophysik*, 22:30–+, 1943.

U. Feldman, I. E. Dammasch, and K. Wilhelm. On the unresolved fine structures of the solar upper atmosphere. iv. the interface with the chromosphere. *APJ*, 558: 423–427, 2001.

L. Feng, B. Inhester, S. K. Solanki, T. Wiegelmann, B. Podlipnik, R. A. Howard, and J.-P. Wuelser. First Stereoscopic Coronal Loop Reconstructions from STEREO SECCHI Images. *Astrophysical Journal, Letters to the Editor*, 671:L205–L208, December 2007. doi: 10.1086/525525.

K. Galsgaard and Å. Nordlund. Coronal Heating by Flux Braiding. *Astrophysical Letters Communications*, 34:175–+, 1996.

G. A. Gary. Plasma Beta above a Solar Active Region: Rethinking the Paradigm. *Solar Physics*, 203:71–86, October 2001.

W. Grotrian. Ergebnisse der Potsdamer Expedition zur Beobachtung der Sonnenfinsternis am 9. Mai 1929 in Takengon (Nordsumatra). 6. Mitteilung. Über die Intensitätsverteilung des kontinuierlichen Spektrums der inneren Korona. Mit 8 Abbildungen. (Eingegangen am 27. Juni 1931). *Zeitschrift fur Astrophysik*, 3:199–+, 1931.

B. V. Gudiksen and Å. Nordlund. An Ab Initio Approach to the Solar Coronal Heating Problem. *APJ*, 618:1020–1030, January 2005. doi: 10.1086/426063.

B. V. Gudiksen and Å. Nordlund. Bulk Heating and Slender Magnetic Loops in the Solar Corona. *APJ*, 572:L113–L116, June 2002. doi: 10.1086/341600.

B. N. Handy, L. W. Acton, C. C. Kankelborg, C. J. Wolfson, D. J. Akin, M. E. Bruner, R. Caravalho, R. C. Catura, R. Chevalier, D. W. Duncan, C. G. Edwards, C. N. Feinstein, S. L. Freeland, F. M. Friedlaender, C. H. Hoffmann, N. E. Hurlburt, B. K. Jurcevich, N. L. Katz, G. A. Kelly, J. R. Lemen, M. Levay, R. W. Lindgren, D. P. Mathur, S. B. Meyer, S. J. Morrison, M. D. Morrison, R. W. Nightingale, T. P. Pope, R. A. Rehse, C. J. Schrijver, R. A. Shine, L. Shing, K. T. Strong, T. D. Tarbell, A. M. Title, D. D. Torgerson, L. Golub, J. A. Bookbinder, D. Caldwell, P. N. Cheimets, W. N. Davis, E. E. Deluca, R. A. McMullen, H. P. Warren, D. Amato, R. Fisher, H. Maldonado, and C. Parkinson. The transition region and coronal explorer. *Solar Physics*, 187:229–260, July 1999. doi: 10.1023/A:1005166902804.

M. Jardine, K. Wood, A. Collier Cameron, J.-F. Donati, and D. H. Mackay. Inferring X-ray coronal structures from Zeeman-Doppler images. *Monthly Notices of the RAS*, 336:1364–1370, November 2002. doi: 10.1046/j.1365-8711.2002.05877.x.

T. J. Kentischer, C. Bethge, D. F. Elmore, R. Friedlein, C. Halbgewachs, M. Knölker, H. Peter, W. Schmidt, M. Sigwarth, and K. Streander. ChroTel: a robotic telescope to observe the chromosphere of the Sun. In *Society of Photo-Optical Instrumentation Engineers (SPIE) Conference Series*, volume 7014 of *Presented at the Society of Photo-Optical Instrumentation Engineers (SPIE) Conference*, August 2008. doi: 10.1117/12.789044.

E. Landi, G. Del Zanna, P.R. Young, K.P. Dere, H.E. Mason, and M. Landini. CHIANTI - An atomic database for emission lines - Paper VII: New data for x-rays and other improvements. 162:261, 2006.

J. C. Maxwell. A dynamical theory of the electromagnetic field. *Royal Society Transactions*, 155:459512, 1865.

J.-P. Meyer. Solar-stellar outer atmospheres and energetic particles, and galactic cosmic rays. *APJS*, 57:173–204, January 1985. doi: 10.1086/191001.

D. A. N. Müller, H. Peter, and V. H. Hansteen. Dynamics of solar coronal loops. II. Catastrophic cooling and high-speed downflows. *Astronomy and Astrophysics*, 424:289–300, September 2004. doi: 10.1051/0004-6361:20040403.

E. N. Parker. Magnetic Neutral Sheets in Evolving Fields - Part Two - Formation of the Solar Corona. *Astrophysical Journal*, 264:642–+, January 1983. doi: 10.1086/160637.

E. N. Parker. Nanoflares and the solar X-ray corona. *Astrophysical Journal*, 330: 474–479, July 1988. doi: 10.1086/166485.

E.N. Parker. Topological dissipation and the small-scale fields in turbulent gases. 174:499–510, 1972.

H. Peter, B. V. Gudiksen, and Å. Nordlund. Coronal Heating through Braiding of Magnetic Field Lines. *APJ*, 617:L85–L88, December 2004. doi: 10.1086/427168.

H. Peter, B. V. Gudiksen, and Å. Nordlund. Forward Modeling of the Corona of the Sun and Solar-like Stars: From a Three-dimensional Magnetohydrodynamic Model to Synthetic Extreme-Ultraviolet Spectra. *Astrophysical Journal*, 638:1086–1100, February 2006.

R. Rosner, W. H. Tucker, and G. S. Vaiana. Dynamics of the quiescent solar corona. *APJ*, 220:643–645, March 1978. doi: 10.1086/155949.

J. Schou, J. Christensen-Dalsgaard, and M. J. Thompson. On comparing helioseismic two-dimensional inversion methods. *APJ*, 433:389–416, September 1994. doi: 10.1086/174653.

C. J. Schrijver and A. M. Title. The Heating of Cool-Star Coronae: From Individual Loops to Global Flux-Flux Scalings. *Astrophysical Journal*, 619:1077–1083, February 2005. doi: 10.1086/426709.

S. Serio, G. Peres, G. S. Vaiana, L. Golub, and R. Rosner. Closed coronal structures. II - Generalized hydrostatic model. *Astrophysical Journal*, 243:288–300, January 1981. doi: 10.1086/158597.

Jr. Spitzer, L. and R. Härm. *Phys. Rev.*, 89:977, 1953.

L. Spitzer. *Physics of fully Ionized Gases*, volume 3. Interscience Tracts on Physics and Astronomy, 1962.

R. F. Stein and A. Nordlund. Simulations of Solar Granulation. I. General Properties. *APJ*, 499:914–+, May 1998. doi: 10.1086/305678.

M. Stix. *The Sun. An Introduction.* The Sun. An Introduction, XIII, 390 pp. 192 figs.. Springer-Verlag Berlin Heidelberg New York. Also Astronomy and Astrophysics Library, 1989.

H. P. Warren, A. R. Winebarger, and J. T. Mariska. Evolving Active Region Loops Observed with the Transition Region and Coronal explorer. II. Time-dependent Hydrodynamic Simulations. *APJ*, 593:1174–1186, August 2003. doi: 10.1086/376678.

M. J. West, P. J. Cargill, and S. J. Bradshaw. Non-Local Heat Conduction and Ite Effect on Coronal Cooling Times. In R. W. Walsh, J. Ireland, D. Danesy, and B. Fleck, editors, *SOHO 15 Coronal Heating*, volume 575 of *ESA Special Publication*, pages 573–+, December 2004.

Danksagung

Zuerst möchte ich mich bei Hardi Peter bedanken. Ich habe viel von seiner Begeisterung zur Physik und seiner wissenschafltichen Arbeit gelernt. Er hat, nicht nur mich, stets motiviert und unterstütz, aber gleichzeitig mir auch den Freiraum gelassen meine eigene Ideen umzusetzten.

Ausserdem möchte ich mich bei Oskar von der Lühe bedanken, der es mir ermöglicht hat meine Arbeit am Kiepenheuer-Institut anzufertigen. Ohne den am Institut installierten Rechen-Cluster wäre eine Durchführung meiner Arbeit nur schwer möglich gewesen.

Natürlich geht mein Dank auch an Christian Bethge als Freund und Wegbegleiter. Er hat meine Arbeit immer kritisch beurteilt und dadurch viel zur Verbesserung beigetragen.

Hans-Peter Doerr danke ich für die Administration des Rechen-Clusters, meines Laptops sowie den vielen kleine Tipps und Tricks welche die Arbeit mit dem Computer erleichtern.

Bei Pia Zacharias bedanke ich mich für die gute Zusammenarbeit, ohne die es ein Teil dieser Arbeit gar nicht gäbe.

Dann gibt es natürlich noch: Tayeb Aiouaz, Christian Beck, Andreas Bitzer, Philippe Bourdin, Morten Franz, Frank Heidecke, Stefan Jendersie, Petri Käpylä, Tassos Nesis,
Christian Nutto, Reza Rezaei, Markus Roth, Rolf Schlichenmeier, Dirk Schmidt, Markus Seiler, Oskar Steiner, Jörn Warnecke, Adrian Zimmer ...

Ich bedanke mich auch bei den anderen Institutsmitgliedern der Elektronik-, Mechanik- und Administrations-Abteilungen die zusammen erst dieses Institut ausmachen. Ich konnte viel von dem weiten Spektrum an Wissen der Mitarbeiter profitieren und wurde immer hilfreich unterstützt. Andreas Bernert möchte ich danken für die lehrreichen Stunden der Metallverarbeitung und bei der Unterstützung bei Bastelarbeiten.

Meinen Eltern, Karin und Schorsch, möchte ich danken für die Unterstützung. Meinen Schwiegereltern, Irene und Günter, danke ich dafür, das sie sich, wie natürlich auch meine Eltern, so liebevoll um meine Söhne kümmern.

Meiner Frau Christine möchte zu tiefst danken für das Verständnis und die Rückenstärkung während meiner Zeit als Doktorand. Besonders möchte ich mich auch bei meinen Söhnen Jonathan und Elias bedanken, die mich gerade während dem Ende dieser Arbeit entbehren mussten.